

Energy-Momentum Tensors and Energy Conditions with Worldline Numerics

Dissertation

zur Erlangung des akademischen Grades
doctor rerum naturalium (Dr. rer. nat.)

vorgelegt dem Rat der Physikalisch-Astronomischen Fakultät
der Friedrich-Schiller-Universität Jena

von Dipl.-Phys. Marco Schäfer,
geboren am 16.03.1984 in Räckelwitz

Gutachter

1. *Prof. Dr. Holger Gies,*
Friedrich-Schiller-Universität Jena

2. *Prof. Dr. Noah Graham,*
Middlebury College, Middlebury

3. *Prof. Dr. Christian Schubert,*
Universidad Michoacana de San Nicolás de Hidalgo, Morelia

Tag der Disputation: 30. April 2013

Abstract

We apply the worldline formalism and its numerical realization to composite operators. Specifically, we compute the energy-momentum tensor induced by a quantum scalar field which is subject to Dirichlet boundary conditions. The worldline formalism is a mapping of quantum field theory amplitudes onto quantum mechanical path integrals. These path integrals can be evaluated numerically very efficiently. Previous calculations were performed for effective interaction energies. In this thesis we show that composite operators like the energy-momentum tensor can be treated in the same way. We check our worldline algorithms by comparing numerical and analytical results for the configurations of a single plate and two parallel plates and provide a detailed analysis of numerical errors. We also investigate the averaged null energy condition in boundary configurations that allow for complete geodesics. This energy condition is fulfilled in all our calculations.

Zusammenfassung

Wir verwenden den Weltlinienformalismus und die Weltliniennumerik zur Berechnung von lokalen Operatoren. Insbesondere berechnen wir den Energieimpulstensor eines quantisierten Skalarfeldes, welches Dirichlet Randbedingungen unterliegt. Der Weltlinienformalismus bildet Amplituden einer Quantenfeldtheorie auf quantenmechanische Pfadintegrale ab. Diese Pfadintegrale können sehr effizient numerisch ausgewertet werden. In bisherigen Rechnungen wurden effektive Wechselwirkungsenergien berechnet. In dieser Dissertation zeigen wir, dass lokale Operatoren wie der Energieimpulstensor genauso behandelt werden können. Wir überprüfen unsere Weltlinienalgorithmen durch den Vergleich von numerischen und analytischen Ergebnissen für den Fall einer einfachen Platte und zweier parallelen Platten und zeigen eine detaillierte Fehlerbetrachtung. Außerdem untersuchen wir die gemittelte Nullenergiebedingung für Randkonfigurationen, die vollständige Geodäten erlauben. Diese Energiebedingung ist in allen unseren Rechnungen erfüllt.

Contents

1	Introduction	11
2	Worldline Formalism for composite operators	17
2.1	The energy-momentum tensor as a composite operator	17
2.2	The worldline representation of $G(\vec{x}, \vec{x}', k)$	22
2.3	Summary	34
3	The energy-momentum tensor for a single plate	35
3.1	Analytic calculation for a single plate	35
3.2	Worldline calculation for one Dirichlet plate	37
3.3	Numerical results for $T_{00}(\vec{x}_{cp}, t)$ and $T_{zz}(\vec{x}_{cp}, t)$	40
3.4	Conclusions	50
4	The energy-momentum tensor for Casimir's parallel plates	51
4.1	Analytical calculation for two parallel plates	51
4.2	Worldline calculation for two parallel Dirichlet plates	56
4.3	Numerical results for $T_{00}(\vec{x}_{cp}, t)$ and $T_{zz}(\vec{x}_{cp}, t)$	60
4.4	Conclusions	65
5	Averaged Null Energy Condition for configurations with complete geodesics	67
5.1	Averaged Null Energy Condition for a plate with a hole in $d = 2$	68
5.2	Averaged Null Energy Condition for a plate with a hole in $d = 3$	79
5.3	Averaged Null Energy Condition for a plate with a slit in $d = 3$	85
5.4	Conclusions	89
6	Summary and outlook	91

Contents

Bibliography	93
A Systematic errors for two parallel plates	99

List of Figures

2.1	Rescaling the worldlines to unit loops	26
3.1	Single plate setup	38
3.2	Systematic errors of cumulants of $(-y_-)$	43
3.3	Systematic errors of $\langle(-y_-)^n\rangle$ for 2^{10} points per loops	45
3.4	Systematic errors of $\langle(-y_-)^n\rangle$ for 2^{14} points per loops	46
3.5	Systematic errors of $\langle(-y_-)^n\rangle$ for 2^{17} points per loops	46
3.6	Systematic errors of $\langle(-y_-)^n\rangle$ for 2^{20} points per loops	47
3.7	Complete systematic errors for derivative terms	48
4.1	Setup of Casimir's parallel plates	57
4.2	Preliminary numerical data in comparison to analytical results	61
4.3	Error estimate of the linearization of ∂sgn	63
4.4	$T_{zz}(\vec{x}_{cp}, t)$ for the original Casimir configuration in $d = 2$ and $d = 3$	64
4.5	NEC along the z axis for two parallel plates in 2 and 3 spatial dimensions	65
5.1	Punctured plate configuration in $d = 2$	68
5.2	Sketch of the angular binning of a worldline	70
5.3	$T_{zz}(\vec{x}_{cp}, t)$ for the punctured plate in $d = 2$ with a simplified intersection condition	73
5.4	NEC along the z axis for the punctured plate in $d = 2$ with a simplified intersection condition	74
5.5	Comparison of $T_{00}(\vec{x}_{cp}, t) _I$ for the plate with a hole in $d = 2$ using different intersection conditions	76
5.6	NEC along the z axis for the punctured plate in $d = 2$ using the precise intersection condition	77

List of Figures

5.7	Punctured plate configuration in $d = 3$	80
5.8	$T_{zz}(\vec{x}_{cp}, t)$ for the punctured plate in $d = 3$ with a simplified intersection condition	81
5.9	NEC along the z axis for the punctured plate in $d = 3$ with a simplified condition of intersection	82
5.10	Comparison of $T_{00}(\vec{x}_{cp}, t) _I$ for the punctured plate in $d = 3$ using different intersection conditions	84
5.11	NEC along the z axis for the punctured plate in $d = 3$	85
5.12	Plate with a slit configuration in $d = 3$	86
5.13	Comparison of $T_{00}(\vec{x}_{cp}, t) _I$ for the plate with a slit using different intersection conditions	87
5.14	NEC along the z axis for plate with a slit in $d = 3$	88
A.1	Systematic errors of EMT components in the parallel plates configuration in $d = 2$ dimensions	100
A.2	Systematic errors of EMT components in the parallel plates configuration in $d = 3$ dimensions	101

List of Tables

3.1	Preliminary results for the single plate in $d = 2$	41
3.2	Preliminary results for the single plate in $d = 3$	41
3.3	Optimal values for f and ε	48
3.4	Optimized numerical results for the single plate	49
4.1	Systematic errors for the original Casimir setup	64

Abbreviations

EMT	energy-momentum tensor, $T_{\mu\nu}(\vec{x}, t)$
BC	boundary condition
DBC	Dirichlet boundary condition
NEC	null energy condition - This term is used for both the projection of the EMT on a null geodesic with tangent vector V^μ , that is, $T_{\mu\nu}(\vec{x}, t)V^\mu V^\nu$, and the inequality $T_{\mu\nu}(\vec{x}, t)V^\mu V^\nu \geq 0$.
ANEC	averaged null energy condition - This term is used for both the integral $\int_\gamma d\lambda T_{\mu\nu}(\vec{x}, t)V^\mu V^\nu$ over a null geodesic γ with tangent vector V^μ and affine parameter λ and for the inequality $\int_\gamma d\lambda T_{\mu\nu}(\vec{x}, t)V^\mu V^\nu \geq 0$.

1 Introduction

Almost 65 years have passed since H.B.G. Casimir published his paper on the effect of boundary conditions in quantum field theory [1]. He showed that fluctuations of the quantized electromagnetic field result in a negative energy between infinite, perfectly conducting plates in the vacuum, and that this energy gives rise to an attractive force between the plates. This Casimir effect has since been studied for several kinds of quantized fields with different boundary conditions and many geometric configurations of boundaries. It has been measured, not only between two parallel plates, but also between a plate and cylinder or sphere.

The theoretical understanding of the Casimir effect has become well developed too. While there are several results known analytically, predicting the sign or the magnitude of the Casimir energy from them has remained difficult. The calculation of the Casimir energy for a sphere in [2] is an example for a positive energy and thus a repulsive force. These results have, however, been questioned for some time, e.g., in [3, 4]. More recently, in [5], instead of idealized boundary conditions, the authors use the interactions with an external potential and perturbatively renormalize divergences by calculating Feynman diagrams. They find that the Casimir energy is finite for smooth potentials but diverges in the perfect boundary limit. In general, Casimir energies are influenced by factors like the parameters of the quantum field and its boundary conditions or temperature. Beyond these, geometric factors like the dimension of spacetime and the shape of the boundaries play an important role [6–9].

Despite all that is known, the Casimir effect is still a paradigmatic test case for the exploration of a diversity of phenomena within quantum field theory. The interaction energies, pressures, and forces caused by imposing boundary conditions on quantum fields are of particular interest. They represent phenomenological observables that can be directly related to experiments. Furthermore, the understanding of quantum effects gained

1 Introduction

from such experiments has already found its way into technological applications. The structures of microchips and integrated circuits, for example, have become so small that quantum effects can no longer be neglected. In addition, micro-electro-mechanical systems (MEMS) promise to open the door to many new applications because they are capable of employing quantum effects directly [10–12].

From a theoretical perspective, the energy-momentum tensor is the quantity in which crucial information about the quantum field is encoded. The energy-momentum tensor (EMT) is also of interest because it is the source term for the gravitational field if the quantum field is coupled to gravity. A study of the gravitational properties of the Casimir energy can be found in [13–15]. Negative energy densities do not pose a problem for the calculation of Casimir forces; they are very similar to negative binding energies in systems with bound states. However, there may arise difficulties with negative energy densities in conjunction with gravity. Since the energy-momentum tensor serves as the source term for gravity, it determines the geometry of spacetime. Consequently, one finds that negative energy densities allow for spacetime metrics in which it is possible to travel with superluminal velocities or to construct time machines or wormholes [16–21]. In turn, it was found that spacetime metrics that allow the construction of time machines, wormholes, and superluminal travel require “exotic matter”, that is, matter with a negative energy density.

One tries to avoid such “exotic” phenomena because they all violate causality, which is one of the most essential principles of physics. Avoiding spacetime metrics that allow causality violations translates, via the Einstein equations of General Relativity, into constraining the energy-momentum tensor. There exist several ways to constrain the energy-momentum tensor in order to prevent causality violations, which usually have the form of energy conditions. Such an energy condition is that the projection of the EMT on a geodesic γ whose tangent vector is denoted by V^μ be larger or equal to zero

$$T_{\mu\nu}V^\mu V^\nu \geq 0.$$

If V^μ is a null vector this condition is called the null energy condition (NEC) and if V^μ is timelike the condition is called the weak energy condition. Such an inequality states that the sum of energy density and pressures that an observer measures while moving along the geodesic γ is always non-negative at any point along the geodesic.

The Casimir effect violates both conditions, in contrast to classical physics, where both conditions are obeyed. Therefore, neither the weak nor the null energy condition may be used to rule out the violation of causality by the Casimir effect. There is, however, a somewhat weaker condition which still suffices to avoid the aforementioned exotic phenomena: the averaged null energy condition (ANEC). It requires that the null energy condition hold only when integrated along the complete geodesic γ . Therefore, ANEC allows for $T_{\mu\nu}V^\mu V^\nu$ to be negative for some region along the geodesic as long as there are regions with positive contributions to the integral which exceed the negative contributions. The ANEC was found to be satisfied by all Casimir examples studied so far on flat Minkowski space [22, 23], but it can be violated on compact flat or curved spacetimes [24–27].

It was shown in [28] that ANEC cannot be violated by a minimally coupled scalar field in flat Minkowski spacetime for geodesics that do neither intersect nor asymptotically approach the boundary. The reason for this is that the boundary cannot affect the causal structure near the geodesic. Such a distant boundary can then only be observed, if one sends a signal from the null geodesic to the boundary and receive it again later. This is, however, not possible for a null geodesic in flat space. As a result, the measurement only on the geodesic corresponds to the measurement in Minkowski spacetime, where the ANEC is obeyed.

In [23] a new version of the ANEC, the achronal ANEC, was proposed. It requires that the ANEC hold only for achronal geodesics. These are geodesics do not contain any points connected by a time-like path. This condition, while weaker than the traditional ANEC, seems to be still sufficient to rule out closed timelike curves and wormholes. The investigation of ANEC remains nevertheless interesting and understanding ANEC in flat space will help with the understanding of ANEC and its possible violations in realistic situations, that is, curved and non-idealized spacetimes with non-idealized physical systems, matter, and interactions.

Since the calculation of the averaged null energy condition requires knowledge of several components of the energy-momentum tensor along a complete geodesic, it may become complicated to calculate particular Casimir configurations. However, the physically interesting geodesics, which are those that collect negative energy densities, are typically directed towards the bounding surfaces and thus ultimately hit the boundary. On the boundary $T_{\mu\nu}V^\mu V^\nu$ acquires a generically large positive contribution from the surface

1 Introduction

itself, which might exceed the negative Casimir contributions. In order to avoid the discussion of such large non-universal contributions, relevant configurations should have holes that a geodesic can pass through. Indeed, the case of a single plate with a hole has been found to respect the averaged null energy condition [22].

It is apparent from these considerations that a general study of energy conditions in Casimir configurations demands a theoretical framework that is able to deal with the energy-momentum tensor in arbitrary geometries of boundary surfaces. Current standard computations of Casimir energy-momentum tensors are usually based on mode summation or expansion, image charge methods, or similar techniques [29–32]. All of these have their own merits and advantages, but they are generally not suited for arbitrary boundary geometries.

In this thesis, we apply the worldline formalism to the energy-momentum tensor of a scalar field that is subject to Dirichlet boundary conditions. The worldline formalism is a mapping of expectation values in quantum field theory on quantum-mechanical path integrals, whose paths can be understood as the paths, or worldlines, of quantum fluctuations [33, 34]. It is by construction independent of the geometry of the boundaries and the background potential and breaks no spacetime symmetries as a consequence. It thus circumvents the difficult computation of the spectrum of the quantum fluctuations. We use worldline numerics [35, 36] for our calculations, which has been used to discuss a variety of nontrivial Casimir configurations and compute effective actions, interaction energies, pressures and forces [37–44].

This thesis is intended to be a manual for the numerical computation of composite operators using the worldline formalism. It is organized as follows: in Chapter 2 we apply the worldline formalism to composite operators, specifically the energy-momentum tensor of a Dirichlet scalar. We emphasize the similarities and differences between the formalism for composite and non-composite operators or functionals like the effective action. In Chapter 3 we test our numerical worldline algorithm by calculating components of the energy-momentum tensor for a single plate with Dirichlet boundary conditions (DBC) analytically and numerically. In Chapter 4, the numerical calculation of the EMT and of the NEC is presented for the parallel plate configuration. We compare our numerical results with known analytical results and discuss the arising systematic and statistical errors. Chapter 5 is devoted to the study of the averaged null energy condition for

configurations that allow for complete geodesics. We present three different setups of boundaries, two of which are known analytically. We conclude with a summary of our results and an outlook on future worldline calculations in Chapter 6.

2 Worldline Formalism for composite operators

In this chapter we apply the worldline formalism to composite operators. In quantum field theory, composite, or local, operators are the local product of field operators and their derivatives. These operators are distribution-valued and thus their product at the same point in spacetime may not be well-defined and can give rise to divergences. Despite that, such local operators can be used for calculations after these divergences have been regulated. This is achieved, for example, by point-splitting, ζ function, or dimensional regularization. In this thesis we investigate the energy-momentum tensor (EMT) of a quantum scalar field. More precisely, we compute the vacuum expectation value of the energy-momentum tensor operator, a composite operator constructed from the scalar field operator and its derivatives. We will focus our calculations on two components of the EMT and evaluate them using worldline numerics. A generalization to the remaining components is then straightforward.

2.1 The energy-momentum tensor as a composite operator

In our calculations, we follow the computations in [32]. There are only a few minor differences. We study a quantum scalar field $\hat{\Phi}(\vec{x}, t)$ that is a \mathcal{C}^∞ map from a domain \mathcal{D} of $d+1$ -dimensional Minkowski spacetime $\mathcal{M}^{(d,1)}$ to the linear space of self-adjoint operators on the Fock space \mathcal{F}

$$\hat{\Phi}(\vec{x}, t) : \mathcal{M}^{(d,1)} \ni \mathcal{D} \rightarrow \mathcal{F}.$$

2 Worldline Formalism for composite operators

$\hat{\Phi}(\vec{x}, t)$ has mass m and is minimally coupled to a static classical background potential $\sigma(\vec{x})$. The background potential will be used later to impose boundary conditions on the fluctuations of $\hat{\Phi}(\vec{x}, t)$. We use the $d + 1$ -dimensional Minkowski metric $g_{\mu\nu}$ with the "mostly minus" signature $(+, -, \dots, -)$. From the Lagrangian density operator

$$\hat{\mathcal{L}} = \frac{1}{2} \partial_\mu \hat{\Phi}(\vec{x}, t) \partial^\mu \hat{\Phi}(\vec{x}, t) - \frac{1}{2} (m^2 + \sigma(\vec{x})) \hat{\Phi}(\vec{x}, t) \hat{\Phi}(\vec{x}, t), \quad (2.1)$$

we derive the equation of motion for $\hat{\Phi}(\vec{x}, t)$,

$$(\partial_\lambda \partial^\lambda + m^2 + \sigma(\vec{x})) \hat{\Phi}(\vec{x}, t) = 0, \quad (2.2)$$

as well as its canonical energy-momentum tensor operator

$$\begin{aligned} \hat{T}_{\mu\nu}(\vec{x}, t) &= \frac{\partial \hat{\mathcal{L}}}{\partial(\partial^\mu \hat{\Phi}(\vec{x}, t))} \partial_\nu \hat{\Phi}(\vec{x}, t) - g_{\mu\nu} \hat{\mathcal{L}} \\ &= \partial_\mu \hat{\Phi}(\vec{x}, t) \partial_\nu \hat{\Phi}(\vec{x}, t) - \frac{1}{2} g_{\mu\nu} \left(\partial^\lambda \hat{\Phi}(\vec{x}, t) \partial_\lambda \hat{\Phi}(\vec{x}, t) - (m^2 + \sigma(\vec{x})) \hat{\Phi}(\vec{x}, t) \hat{\Phi}(\vec{x}, t) \right). \end{aligned} \quad (2.3)$$

The EMT operator in Eq. (2.3) contains products of field operators at the same spacetime point that lead to divergences. We regulate them by a point-splitting procedure in the spatial components \vec{x} , that is, we apply the following replacement rules:

$$\hat{\Phi}(\vec{x}, t) \hat{\Phi}(\vec{x}, t) \longrightarrow \hat{\Phi}(\vec{x}, t) \hat{\Phi}(\vec{x}', t) \quad \partial_\alpha \hat{\Phi}(\vec{x}, t) \partial_\beta \hat{\Phi}(\vec{x}, t) \longrightarrow \partial_\alpha \hat{\Phi}(\vec{x}, t) \partial'_\beta \hat{\Phi}(\vec{x}', t).$$

The point-split EMT operator is then

$$\hat{T}_{\mu\nu}(\vec{x}, t) = \lim_{\vec{x}' \rightarrow \vec{x}} \left[\partial_\mu \hat{\Phi}(\vec{x}, t) \partial'_\nu \hat{\Phi}(\vec{x}', t) - \frac{1}{2} g_{\mu\nu} (\partial^\lambda \partial'_\lambda - m^2 - \sigma(\vec{x})) \hat{\Phi}(\vec{x}, t) \hat{\Phi}(\vec{x}', t) \right]. \quad (2.4)$$

As we mentioned before, the goal of this thesis is to compute the effects of boundary conditions on the energy-momentum tensor. The energy conditions that the EMT fulfills in such situations are of particular interest. Therefore, while all components of the energy-momentum tensor are of physical interest, for specific boundary geometries, only some may be required to compute energy conditions. We restrict ourselves to computing the null energy condition (NEC) in the following chapters. For the sake of convenience, we compute the NEC only in the z direction, where the z coordinate is always the d th coordinate of our spatial vectors $\vec{x} = (x^1, \dots, x^d) = (x^1, \dots, z)$. This null energy condition

2.1 The energy-momentum tensor as a composite operator

is then given by the vacuum expectation value of the projection of the EMT on a null curve with the null tangent vector $V^\mu = (1, 0, \dots, 0, 1)$,

$$0 \leq \left\langle \hat{T}_{\mu\nu}(\vec{x}, t) V^\mu V^\nu \right\rangle = \left\langle \hat{T}_{00}(\vec{x}, t) + \hat{T}_{zz}(\vec{x}, t) \right\rangle = T_{00}(\vec{x}, t) + T_{zz}(\vec{x}, t), \quad (2.5)$$

where $\langle \dots \rangle$ denotes the vacuum expectation value. Since only $T_{00}(\vec{x}, t)$ and $T_{zz}(\vec{x}, t)$ are needed for the NEC in Eq. (2.5), all calculations will be performed with these two components. However, all of these computations can be generalized straightforwardly to other components.

In order to compute the vacuum expectation values of Eq. (2.4), we expand the field operator $\hat{\Phi}(\vec{x}, t)$ in momentum modes $\psi_p(\vec{x})$ and bosonic creation and annihilation operators \hat{a}_p^\dagger and \hat{a}_p ,

$$\hat{\Phi}(\vec{x}, t) = \int \frac{d^d p}{(2\pi)^d} \frac{1}{\sqrt{2E_p}} (\psi_p(\vec{x}) e^{iE_p t} \hat{a}_p + \psi_p^*(\vec{x}) e^{-iE_p t} \hat{a}_p^\dagger),$$

with $E_p^2 = p^2 + m^2$ and $[\hat{a}_p, \hat{a}_q^\dagger] = (2\pi)^d \delta^d(p - q)$. The $\psi_p(\vec{x})$ are defined as eigenmodes of the Laplacian in the presence of the potential $\sigma(\vec{x})$, i.e., they obey the Helmholtz equation

$$\left(-\vec{\nabla}^2 - p^2 + \sigma(\vec{x}) \right) \psi_p(\vec{x}) = 0. \quad (2.6)$$

The vacuum expectation values in Eq. (2.5) are now written as

$$\begin{aligned} T_{00}(\vec{x}, t)|_\sigma &= \left\langle \hat{T}_{00}(\vec{x}, t) \right\rangle_\sigma = \lim_{\vec{x}' \rightarrow \vec{x}} \int \frac{d^d p}{(2\pi)^d} \left(\frac{E_p}{2} + \frac{1}{4E_p} \vec{\nabla} \cdot (\vec{\nabla} + \vec{\nabla}') \right) \psi_p(\vec{x}) \psi_p^*(\vec{x}'), \\ T_{zz}(\vec{x}, t)|_\sigma &= \left\langle \hat{T}_{zz}(\vec{x}, t) \right\rangle_\sigma = \lim_{\vec{x}' \rightarrow \vec{x}} \int \frac{d^d p}{(2\pi)^d} \left(\frac{1}{2E_p} \partial_z \partial_{z'} - \frac{1}{4E_p} \vec{\nabla} \cdot (\vec{\nabla} + \vec{\nabla}') \right) \psi_p(\vec{x}) \psi_p^*(\vec{x}'). \end{aligned} \quad (2.7)$$

The term $\psi_p(\vec{x}) \psi_p^*(\vec{x}')$ in Eq. (2.7) is already very suggestive of the spectral representation of a Green's function. Indeed,

$$G_\sigma(\vec{x}, \vec{x}', k) = \int \frac{d^d p}{(2\pi)^d} \frac{\psi_p(\vec{x}) \psi_p^*(\vec{x}')}{p^2 - k^2 - i\varepsilon} \quad (2.8)$$

is the spectral representation of the Green's function or the fundamental solution of Eq. (2.6),

$$\left(-\vec{\nabla}^2 - k^2 + \sigma(\vec{x}) \right) G_\sigma(\vec{x}, \vec{x}', k) = \delta(\vec{x} - \vec{x}'). \quad (2.9)$$

2 Worldline Formalism for composite operators

Before we can express Eq. (2.7) in terms of $G_\sigma(\vec{x}, \vec{x}', k)$, we insert unity in the form

$$1 = \int_0^\infty dk 2k \delta(p^2 - k^2) = \int_0^\infty dk 2k \lim_{\varepsilon \rightarrow 0^+} \frac{1}{\pi} \text{Im} \left(\frac{1}{p^2 - k^2 - i\varepsilon} \right).$$

A subsequent exchange of the k and p integrations casts Eq. (2.7) in the following form:

$$\begin{aligned} T_{00}(\vec{x}, t)|_\sigma &= \lim_{\vec{x}' \rightarrow \vec{x}} \int_0^\infty dk \frac{k}{\pi} \left(E_k + \frac{1}{2E_k} \vec{\nabla} \cdot (\vec{\nabla} + \vec{\nabla}') \right) \text{Im} \int \frac{d^d p}{(2\pi)^d} \frac{\psi_p(\vec{x}) \psi_p^*(\vec{x}')}{p^2 - k^2 - i\varepsilon} \\ T_{zz}(\vec{x}, t)|_\sigma &= \lim_{\vec{x}' \rightarrow \vec{x}} \int_0^\infty dk \frac{k}{\pi} \left(\frac{1}{E_k} \partial_z \partial_{z'} - \frac{1}{2E_k} \vec{\nabla} \cdot (\vec{\nabla} + \vec{\nabla}') \right) \text{Im} \int \frac{d^d p}{(2\pi)^d} \frac{\psi_p(\vec{x}) \psi_p^*(\vec{x}')}{p^2 - k^2 - i\varepsilon}. \end{aligned} \tag{2.10}$$

The integral inside the imaginary part is immediately recognized as the Green's function $G_\sigma(\vec{x}, \vec{x}', k)$. In general, a decaying exponential $e^{-k/\Lambda}$ must be inserted instead of unity in order to construct local counterterms for renormalization (cf. [32]). Λ then serves as a cutoff for large momenta k . This is, however, not necessary in our calculations because we are going to evaluate the EMT only at points for which $\sigma(\vec{x}) = 0$, so that all local counterterms, that is, all counterterms that depend on $\sigma(\vec{x})$, are automatically zero. Furthermore, since the term $\psi_p(\vec{x}) \psi_p^*(\vec{x}')$ is in general complex, pulling it into the argument of the imaginary part generates an additional term that is proportional to $\text{Im} \psi_p(\vec{x}) \psi_p^*(\vec{x}')$. We have not displayed this term and need not consider it because it vanishes in the limit $\vec{x} \rightarrow \vec{x}'$.

The effects of boundary conditions imposed on the field fluctuations by the potential $\sigma(\vec{x})$ are described by the difference between the EMT with non-vanishing potential and the EMT with $\sigma(\vec{x}) = 0$. So far, we have left the potential $\sigma(\vec{x})$ arbitrary to emphasize that our calculations are independent of its specific properties. We can therefore repeat all the above steps with a vanishing potential. The only changes that occur are the mode functions $\psi_p(\vec{x})$ in Eq. (2.6). The corresponding Green's function is not $G_\sigma(\vec{x}, \vec{x}', k)$ but $G_0(\vec{x}, \vec{x}', k)$, defined by Eq. (2.9) for vanishing potential. The vacuum expectation values

2.1 The energy-momentum tensor as a composite operator

of the EMT components for vanishing potential are

$$\begin{aligned}
 T_{00}(\vec{x}, t) &= \lim_{\vec{x}' \rightarrow \vec{x}} \int_0^\infty dk \frac{k}{\pi} \left(E_k + \frac{1}{2E_k} \vec{\nabla} \cdot (\vec{\nabla} + \vec{\nabla}') \right) \text{Im} G(\vec{x}, \vec{x}', k), \\
 T_{zz}(\vec{x}, t) &= \lim_{\vec{x}' \rightarrow \vec{x}} \int_0^\infty dk \frac{k}{\pi} \left(\frac{1}{E_k} \partial_z \partial_{z'} - \frac{1}{2E_k} \vec{\nabla} \cdot (\vec{\nabla} + \vec{\nabla}') \right) \text{Im} G(\vec{x}, \vec{x}', k),
 \end{aligned} \tag{2.11}$$

where we have used $G(\vec{x}, \vec{x}', k) = G_\sigma(\vec{x}, \vec{x}', k) - G_0(\vec{x}, \vec{x}', k)$. The great advantage of Eq. (2.11) is that these expressions are independent of any specific mode expansion of $\hat{\Phi}(\vec{x}, t)$. They only depend on the Green's function $G(\vec{x}, \vec{x}', k)$, which is representation-independent by definition. Therefore, any method for the computation of $G(\vec{x}, \vec{x}', k)$ can be used at this stage, e.g., an optical approach in [32]. The subtraction of the vacuum Green's function $G_0(\vec{x}, \vec{x}', k)$ also removes the divergent terms that are independent of the potential $\sigma(\vec{x})$.

Before we apply the worldline formalism to compute $T_{00}(\vec{x}, t)$ and $T_{zz}(\vec{x}, t)$, we will make a change of variables in Eq. (2.11). This variable transformation allows us, at least in part, to exchange the evaluation of the point-splitting limit and the derivatives. We define *common point* variables by

$$\vec{x}_{cp} := \frac{\vec{x} + \vec{x}'}{2}, \quad \vec{\Delta} := \frac{\vec{x} - \vec{x}'}{2}$$

and replace the point-splitting limit $\vec{x} \rightarrow \vec{x}'$ by $\vec{\Delta} \rightarrow 0$. The term *common point* stems from the kind of closed worldlines or loops that we are going to use in our numerical evaluations, which all have one point in common. The derivatives in Eq. (2.11) can then be computed with the help of the mode functions $\psi_p(\vec{x})\psi_p^*(\vec{x}')$. We find for the first term

$$\begin{aligned}
 \lim_{\vec{x}' \rightarrow \vec{x}} \vec{\nabla} \cdot (\vec{\nabla} + \vec{\nabla}') \psi_p(\vec{x})\psi_p^*(\vec{x}') &= \lim_{\vec{x}' \rightarrow \vec{x}} \left[\left(\vec{\nabla}^2 \psi_p(\vec{x}) \right) \psi_p^*(\vec{x}') + \left(\vec{\nabla} \psi_p(\vec{x}) \right) \left(\vec{\nabla}' \psi_p^*(\vec{x}') \right) \right] \\
 &= \frac{1}{2} \vec{\nabla}_{cp}^2 \psi_p(\vec{x}_{cp})\psi_p^*(\vec{x}_{cp}),
 \end{aligned}$$

where $\vec{\nabla}_{cp}^2$ is the second derivative with respect to the coordinate \vec{x}_{cp} . In the second term we are not able to evaluate the limit $\vec{\Delta} \rightarrow 0$ completely, but find

$$\begin{aligned}
 \lim_{\vec{x}' \rightarrow \vec{x}} \partial_z \partial_{z'} \psi_p(\vec{x})\psi_p^*(\vec{x}') &= \lim_{\vec{x}' \rightarrow \vec{x}} \left[\partial_z \psi_p(\vec{x}) \right] \left[\partial_{z'} \psi_p^*(\vec{x}') \right] \\
 &= \frac{1}{4} \lim_{\vec{\Delta} \rightarrow 0} \left(\partial_{z_{cp}}^2 - \partial_{\Delta_z}^2 \right) \psi_p(\vec{x}_{cp} + \vec{\Delta})\psi_p^*(\vec{x}_{cp} - \vec{\Delta}).
 \end{aligned}$$

2 Worldline Formalism for composite operators

Here we have to act with the derivatives ∂_{Δ_z} before we evaluate the point-splitting limit. Nevertheless, the transformation to *common point* variables allows for a little more compact notation of our previous result

$$\begin{aligned} T_{00}(\vec{x}, t) &= \lim_{\vec{\Delta} \rightarrow 0} \int_0^\infty dk \frac{k}{\pi} \left(E_k + \frac{1}{4E_k} \vec{\nabla}_{cp}^2 \right) \text{Im} G(\vec{x}, \vec{x}', k), \\ T_{zz}(\vec{x}, t) &= \lim_{\vec{\Delta} \rightarrow 0} \int_0^\infty dk \frac{k}{\pi} \left(\frac{1}{4E_k} \left(\partial_{z_{cp}}^2 - \partial_{\Delta_z}^2 \right) - \frac{1}{4E_k} \vec{\nabla}_{cp}^2 \right) \text{Im} G(\vec{x}, \vec{x}', k), \end{aligned} \quad (2.12)$$

where $G(\vec{x}, \vec{x}', k)$ needs to be evaluated at $\vec{x} = \vec{x}_{cp} + \vec{\Delta}$ and $\vec{x}' = \vec{x}_{cp} - \vec{\Delta}$.

2.2 The worldline representation of $G(\vec{x}, \vec{x}', k)$

We use the proper-time or worldline representation for the Green's function $G(\vec{x}, \vec{x}', k)$ in this thesis. Toward this end, we interpret $G(\vec{x}, \vec{x}', k)$ as the matrix element of an operator $\hat{\mathcal{G}}(k)$ and Eq. (2.6) as a quantum mechanical Schrödinger problem whose Hamiltonian is $H = -\vec{\nabla}^2 + \sigma(\vec{x})$. The function $G(\vec{x}, \vec{x}', k)$ then corresponds to a quantum mechanical propagator, Fourier transformed to energy space, from which the free motion has been subtracted. Hence, it can be written as a Feynman path integral in position space:

$$\begin{aligned} \text{Im} G(\vec{x}, \vec{x}', k) &= \text{Im} \langle \vec{x}' | \hat{\mathcal{G}}(k) | \vec{x} \rangle \\ &= \text{Im} i \int_0^\infty ds e^{isk^2} \langle \vec{x}' | e^{-is(-\vec{\nabla}^2 + \sigma(\vec{x}))} - e^{is\vec{\nabla}^2} | \vec{x} \rangle \end{aligned} \quad (2.13)$$

$$= \text{Im} i \int_0^\infty ds e^{isk^2} \int_{\vec{x}=\vec{x}(0)}^{\vec{x}'=\vec{x}(s)} \mathcal{D}\vec{x}(\tau) e^{i \int_0^s d\tau \frac{\dot{\vec{x}}^2}{4}} \left(e^{-i \int_0^s d\tau \sigma(\vec{x}(\tau))} - 1 \right) \quad (2.14)$$

$$= \text{Im} \int_0^\infty dT e^{-Tk_E^2} \int_{\vec{x}=\vec{x}(0)}^{\vec{x}'=\vec{x}(T)} \mathcal{D}\vec{x}(\tau) e^{-\int_0^T d\tau \frac{\dot{\vec{x}}^2}{4}} \left(e^{-\int_0^T d\tau \sigma(\vec{x}(\tau))} - 1 \right). \quad (2.15)$$

The matrix element in Eq. (2.13) is easily identified as quantum mechanical transition amplitude of a fictitious particle moving from \vec{x} at the fictitious time $\tau = 0$ to \vec{x}' at $\tau = s$ with a Hamiltonian $H = -\vec{\nabla}^2 + \sigma(\vec{x})$. The corresponding Feynman path integral

2.2 The worldline representation of $G(\vec{x}, \vec{x}', k)$

in position space is then straightforward to find. In the last step, we performed formal Euclidean rotations in both the s and k planes, such that $s = -iT$ and $k_E = ik$, which are consistent with causality. This casts $G(\vec{x}, \vec{x}', k)$ in its Euclidean form Eq. (2.15).

The variables s and T are called Minkowskian and Euclidean proptime, respectively. Both describe the time evolution of the fictitious Schrödinger problem, but neither is a physical, measurable time.

An analogous proptime representation for the effective action has been used in previous calculations of effective interaction energies for the Casimir effect and similar boundary configurations [35, 39, 40]. The worldline representation of the effective action contains, however, a path integral over closed loops, whereas for $G(\vec{x}, \vec{x}', k)$, open worldlines running from \vec{x} to \vec{x}' must be computed.

The path integral in Eq. (2.15) is implicitly normalized in such a way that the free path integral gives the standard free propagator,

$$\int_{\vec{x}=\vec{x}(0)}^{\vec{x}'=\vec{x}(T)} \mathcal{D}\vec{x}(\tau) e^{-\int_0^T d\tau \frac{\dot{\vec{x}}^2}{4}} = \frac{e^{-\frac{\vec{\Delta}^2}{T}}}{(4\pi T)^{\frac{d}{2}}}, \quad (2.16)$$

where again $\vec{\Delta} = (\vec{x} - \vec{x}')/2$. From this normalization one derives the shorthand notation for the path integral expectation value of an arbitrary operator $\mathcal{O}[\vec{x}(\tau)]$:

$$\langle \mathcal{O}[\vec{x}(\tau)] \rangle_{\vec{x}, \vec{x}'} \cdot \frac{e^{-\frac{\vec{\Delta}^2}{T}}}{(4\pi T)^{\frac{d}{2}}} := \int_{\vec{x}=\vec{x}(0)}^{\vec{x}'=\vec{x}(T)} \mathcal{D}\vec{x}(\tau) e^{-\int_0^T d\tau \frac{\dot{\vec{x}}^2}{4}} \mathcal{O}[\vec{x}(\tau)]. \quad (2.17)$$

We use this notation to write the propagator $G(\vec{x}, \vec{x}', k)$ as

$$\text{Im } G(\vec{x}, \vec{x}', k) \Big|_{k=-ik_E} = \text{Im} \int_0^\infty \frac{dT}{(4\pi T)^{\frac{d}{2}}} e^{-Tk_E^2} e^{-\frac{\vec{\Delta}^2}{T}} \left\langle e^{-\int_0^T d\tau \sigma(\vec{x}(\tau))} - 1 \right\rangle_{\vec{x}, \vec{x}'}. \quad (2.18)$$

However, the EMT in Eq. (2.12) has the functional structure

$$T_{--}(\vec{x}_{cp}, t) \propto \int_0^\infty dk f(k) \text{Im} \left[\int_0^\infty ds e^{isk^2} g(s) \right]. \quad (2.19)$$

Due to the factor e^{isk^2} , the Euclidean rotations of s and k should not be performed independently but simultaneously. To do so, we pull the k integral inside the argument

2 Worldline Formalism for composite operators

of the imaginary part. We use the Minkowskian versions of Eq. (2.16) and Eq. (2.17) as well as $E_k^2 = m^2 + k^2$ and thus find that only two different integrals (\mathcal{I}_1 and \mathcal{I}_2) occur in Eq. (2.12):

$$\begin{aligned}
\mathcal{I}_1 &= \text{Im} \left[i \int_0^\infty ds \frac{e^{i\tilde{\Delta}^2/s}}{(4\pi is)^{d/2}} \left\langle e^{-i \int_0^s d\tau \sigma(\vec{x}(\tau))} - 1 \right\rangle \int_0^\infty dk k \sqrt{k^2 + m^2} e^{isk^2} \right] \\
&= \text{Im} \left[- \int_0^\infty dT \frac{e^{-\tilde{\Delta}^2/T}}{(4\pi T)^{d/2}} \left\langle e^{-\int_0^T d\tau \sigma(\vec{x}(\tau))} - 1 \right\rangle \int_0^\infty dk_E k_E \sqrt{m^2 - k_E^2} e^{-Tk_E^2} \right] \\
&= - \int_0^\infty dT \frac{e^{-\tilde{\Delta}^2/T}}{(4\pi T)^{d/2}} \left\langle e^{-\int_0^T d\tau \sigma(\vec{x}(\tau))} - 1 \right\rangle \text{Im} \left[\frac{i}{4T^{3/2}} e^{-m^2 T} \left(\sqrt{\pi} - \Gamma \left[\frac{3}{2}, -m^2 T \right] \right) \right] \\
&\stackrel{m \rightarrow 0}{=} - \int_0^\infty dT \frac{e^{-\tilde{\Delta}^2/T}}{(4\pi T)^{d/2}} \left\langle e^{-\int_0^T d\tau \sigma(\vec{x}(\tau))} - 1 \right\rangle \frac{1}{4T^{3/2}} \sqrt{\pi}, \tag{2.20}
\end{aligned}$$

$$\begin{aligned}
\mathcal{I}_2 &= \text{Im} \left[i \int_0^\infty ds \frac{e^{i\tilde{\Delta}^2/s}}{(4\pi is)^{d/2}} \left\langle e^{-i \int_0^s d\tau \sigma(\vec{x}(\tau))} - 1 \right\rangle \int_0^\infty dk \frac{k}{\sqrt{k^2 + m^2}} e^{isk^2} \right] \\
&= \text{Im} \left[- \int_0^\infty dT \frac{e^{-\tilde{\Delta}^2/T}}{(4\pi T)^{d/2}} \left\langle e^{-\int_0^T d\tau \sigma(\vec{x}(\tau))} - 1 \right\rangle \int_0^\infty dk_E \frac{k_E}{\sqrt{m^2 - k_E^2}} e^{-Tk_E^2} \right] \\
&= - \int_0^\infty dT \frac{e^{-\tilde{\Delta}^2/T}}{(4\pi T)^{d/2}} \left\langle e^{-\int_0^T d\tau \sigma(\vec{x}(\tau))} - 1 \right\rangle \text{Im} \left[e^{-m^2 T} \sqrt{\frac{\pi}{4T}} \left(\text{Erfi} \left[m\sqrt{T} \right] - i \right) \right] \\
&\stackrel{m \rightarrow 0}{=} \int_0^\infty dT \frac{e^{-\tilde{\Delta}^2/T}}{(4\pi T)^{d/2}} \left\langle e^{-\int_0^T d\tau \sigma(\vec{x}(\tau))} - 1 \right\rangle \sqrt{\frac{\pi}{4T}}. \tag{2.21}
\end{aligned}$$

For both calculations we performed the substitution $s = -iT$ and $k = -ik_E$ in the integration variables and the rotation of the integral contours in the second line. We assume $m > 0$ and $T > 0$ and take the massless limit only in the last line because the results are greatly simplified as $m \rightarrow 0$. We will hence consider the field $\hat{\Phi}(\vec{x}, t)$ to be massless from now on. The massless limit is, however, not a necessity and the following calculations are easily generalized to the case of finite m .

With all these considerations, we are finally able to write down compact expressions for the vacuum-subtracted vacuum expectation values of $\hat{T}_{00}(\vec{x}, t)$ and $\hat{T}_{zz}(\vec{x}, t)$ in the

worldline representation,

$$\begin{aligned}
 T_{00}(\vec{x}_{cp}, t) &= \frac{1}{(4\pi)^{\frac{d+1}{2}}} \lim_{\vec{\Delta} \rightarrow 0} \int_0^\infty \frac{dT}{4T^{\frac{d+1}{2}}} \left(-\frac{2}{T} + \vec{\nabla}_{cp}^2 \right) e^{-\frac{\vec{\Delta}^2}{T}} \left\langle e^{-\int_0^T d\tau \sigma(\vec{x}(\tau))} - 1 \right\rangle_{\vec{x}_{cp}, \vec{\Delta}} \\
 T_{zz}(\vec{x}_{cp}, t) &= \frac{1}{(4\pi)^{\frac{d+1}{2}}} \lim_{\vec{\Delta} \rightarrow 0} \int_0^\infty \frac{dT}{4T^{\frac{d+1}{2}}} \left(\partial_{z_{cp}}^2 - \partial_{\Delta_z}^2 - \vec{\nabla}_{cp}^2 \right) e^{-\frac{\vec{\Delta}^2}{T}} \left\langle e^{-\int_0^T d\tau \sigma(\vec{x}(\tau))} - 1 \right\rangle_{\vec{x}_{cp}, \vec{\Delta}}.
 \end{aligned} \tag{2.22}$$

2.2.1 Worldline Numerics for worldline expectation values

The expectation value of the path integral in Eq. (2.22) is defined as

$$\left\langle e^{-\int_0^T d\tau \sigma(\vec{x}(\tau))} - 1 \right\rangle_{\vec{x}_{cp}, \vec{\Delta}} := \frac{\int_{\vec{x}=\vec{x}(0)}^{\vec{x}'=\vec{x}(T)} \mathcal{D}\vec{x}(\tau) e^{-\int_0^T d\tau \frac{\dot{\vec{x}}^2}{4}} \left(e^{-\int_0^T d\tau \sigma(\vec{x}(\tau))} - 1 \right)}{\int_{\vec{x}=\vec{x}(0)}^{\vec{x}'=\vec{x}(T)} \mathcal{D}\vec{x}(\tau) e^{-\int_0^T d\tau \frac{\dot{\vec{x}}^2}{4}}}. \tag{2.23}$$

This is an expectation value for worldlines $\vec{x}(\tau)$ that start at $\vec{x} = \vec{x}(0)$ and end at $\vec{x}' = \vec{x}(T)$. They are weighted with a Gaussian velocity distribution. For the numerical calculations, it is convenient to rescale the worldlines $\vec{x}(\tau)$ such that, in the limit $\vec{x} \rightarrow \vec{x}'$, all paths have one common start and endpoint $\vec{x}_{cp} = (\vec{x} + \vec{x}')/2$ (Fig. 2.1). These worldlines are then referred to as *common point* loops or lines. The remaining path is written in terms of a dimensionless unit loop $\vec{y}(t)$ with $t \in [0, 1]$ and $\tau = Tt$. The unit loop $\vec{y}(t)$ can itself be written as a straight path from $\vec{y}(0) = \vec{u}$ to $\vec{y}(1) = \vec{v}$ and some deviation $\vec{Z}(t)$ that obeys $\vec{Z}(0) = 0 = \vec{Z}(1)$. The origin of the \vec{y} coordinate system is chosen to lie at the point \vec{x}_{cp} . The points \vec{u} and \vec{v} then lie symmetrically around this origin ($\vec{u} = -\vec{v}$), which suggests the substitution $\vec{\delta} = (\vec{u} - \vec{v})/2$,

$$\vec{x}(\tau) = \vec{x}(Tt) = \vec{x}_{cp} + \sqrt{T} \vec{y}(t) \tag{2.24}$$

$$= \vec{x}_{cp} + \sqrt{T} \left(t\vec{v} + (1-t)\vec{u} + \vec{Z}(t) \right) \tag{2.25}$$

$$= \vec{x}_{cp} + \sqrt{T} \left((1-2t)\vec{\delta} + \vec{Z}(t) \right). \tag{2.26}$$

In the limit $\vec{\delta} \rightarrow 0$ the path $\vec{y}(t)$ becomes closed, thus justifying the name unit loop.

2 Worldline Formalism for composite operators

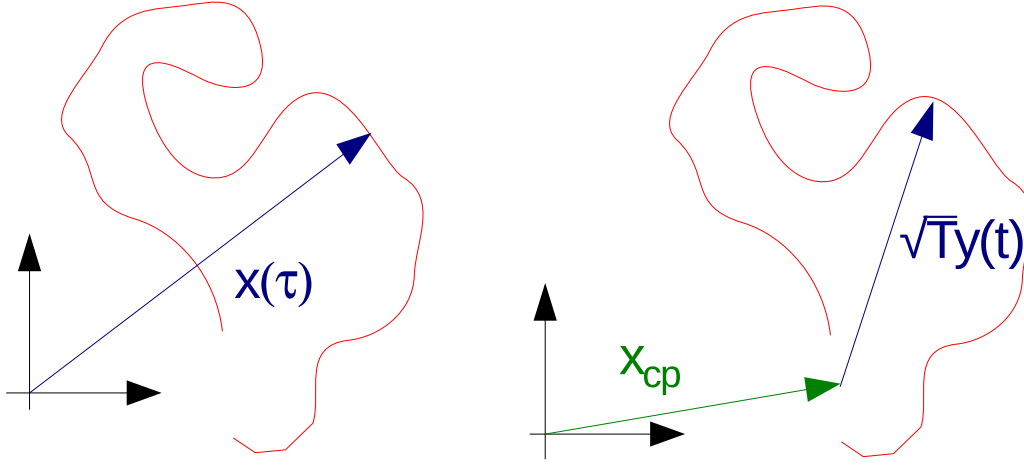


Figure 2.1 Schematic depiction of the rescaling from the worldlines $\vec{x}(\tau)$ to the unit loops $\vec{y}(t)$.

The main advantage of the rescaling to unit loops is that it makes the weight factor in the path integral independent of T ,

$$\int_{\vec{x}=\vec{x}(0)}^{\vec{x}'=\vec{x}(T)} \mathcal{D}\vec{x}(\tau) e^{-\int_0^T d\tau \frac{\dot{\vec{x}}^2}{4}} e^{-\int_0^T d\tau \sigma(\vec{x}(\tau))} \implies \int_{\vec{y}(0)=\vec{x}/\sqrt{T}}^{\vec{y}(1)=\vec{x}'/\sqrt{T}} \mathcal{D}\vec{y}(t) e^{-\int_0^1 dt \frac{\dot{\vec{y}}^2}{4}} e^{-\int_0^1 dt \sigma(\vec{x}_{cp} + \sqrt{T}\vec{y}(t))}. \quad (2.27)$$

This allows us to compute the expectation value in Eq. (2.23) by generating only one ensemble of unit loops $\vec{y}(t)$, which are defined with respect to the same coordinate system. We also immediately see the connection between the variables $\vec{\Delta}$ and $\vec{\delta}$,

$$\frac{\vec{\Delta}}{\sqrt{T}} = \frac{\vec{x} - \vec{x}'}{2\sqrt{T}} = \vec{\delta}. \quad (2.28)$$

This connection is crucial for the computation of the derivatives of the expectation value with respect to Δ_z .

We now compute the expectation values of these rescaled path integrals by replacing the path integral with a sum over a finite number N of unit loops. These loops are themselves approximated by a finite number n_{ppl} of points per loop \vec{y}_i with $i \in \{0, \dots, n_{ppl}\}$. The points \vec{y}_i are random numbers which are distributed according to the Gaussian weight

2.2 The worldline representation of $G(\vec{x}, \vec{x}', k)$

factor in Eq. (2.27). As a result, the expectation value of an operator \mathcal{O} is written as an average,

$$\langle \mathcal{O} \rangle_{\vec{x}_{cp}, \vec{\Delta}} = \frac{1}{N} \sum_{l=1}^N \mathcal{O}_l(\vec{y}_l), \quad i \in \{1, \dots, n_{ppl}\}. \quad (2.29)$$

The common point lines \vec{y}_i can be conveniently generated with the d loop algorithm [35], which also works for open worldlines.

2.2.2 Dirichlet constraints on $\partial\mathcal{D}$

The entire formalism that we have outlined so far works, of course, for arbitrary static background field configurations $\sigma(\vec{x})$. In our calculations, we use

$$\sigma(\vec{x}) = \lambda \int_{\partial\mathcal{D}} d\Sigma \delta(\vec{x} - \vec{x}_{\partial\mathcal{D}}), \quad \vec{x}_{\partial\mathcal{D}} \in \partial\mathcal{D}, \quad (2.30)$$

where $d\Sigma$ is a surface element on $\partial\mathcal{D}$. We then arrive at Dirichlet BCs in the limit $\lambda \rightarrow \infty$.

The subtraction of the vacuum Green's function in Eq. (2.11) already removed all divergences independent of $\sigma(\vec{x})$. Therefore, $G(\vec{x}, \vec{x}', k)$ can only diverge at points for which the background potential is not zero. This means that Eq. (2.30) renders the energy-momentum tensor in Eq. (2.22) finite on \mathcal{D} , where the potential σ vanishes. The remaining divergences are then located on the boundary $\partial\mathcal{D}$. They can be related to the infinite amount of energy which is necessary to constrain $\hat{\Phi}(\vec{x}, t)$ on all momentum scales in order to fulfill the Dirichlet boundary condition on $\partial\mathcal{D}$.

The parametrization Eq. (2.30) and the subsequent Dirichlet limit greatly simplify the expectation value of the path integral because now we have

$$\begin{aligned} \left\langle e^{-\int_0^1 dt \sigma(\vec{x}_{cp} + \sqrt{T}\vec{y}(t))} - 1 \right\rangle_{\vec{x}_{cp}, \vec{\Delta}} &= \left\{ \begin{array}{l} -1 \text{ if } \vec{x}_{cp} + \sqrt{T}\vec{y}(t) \text{ intersects } \partial\mathcal{D} \\ 0 \text{ otherwise} \end{array} \right\} \\ &= - \left\langle \Theta \left[\mathcal{F}(\vec{x}_{cp} + \sqrt{T}\vec{y}(t)) \right] \right\rangle_{\vec{x}_{cp}, \vec{\Delta}}. \end{aligned} \quad (2.31)$$

Equation Eq. (2.31) states that only paths $\vec{x}_{cp} + \sqrt{T}\vec{y}(t)$ which violate the boundary conditions lead to deviations from the trivial vacuum and thus contribute to the expectation value. We call the function \mathcal{F} the intersection condition. It gives a geometric description of how the worldlines intersect the boundary and for which values of T this happens.

2 Worldline Formalism for composite operators

As long as the start and end point of the worldline are not on the boundary, that is, as long as $\vec{x}_{cp} \pm \vec{\Delta} \notin \partial\mathcal{D}$, the intersection condition will always determine a minimal non-zero value for the proptime $T_{min} > 0$ for which the loop first intersects $\partial\mathcal{D}$. T_{min} denotes the minimum proptime that is necessary for a worldline to propagate from the start to the end point and intersect a boundary in between. For any $T < T_{min}$ deviations from the straight line between \vec{x} and \vec{x}' are typically strongly suppressed. Only for sufficiently large proptimes $T \geq T_{min}$ does the diffusive Brownian motion process, described by the path integral, create sufficiently large random detours that can intersect $\partial\mathcal{D}$. In the proptime integral, T_{min} serves as a lower bound and removes the divergence which would occur for $T \rightarrow 0$. From a physics point of view, T_{min} acts as an ultraviolet cutoff as small proptimes correspond to large momenta. \mathcal{F} may also provide an upper bound T_{max} in general. T_{max} is then the proptime for which the worldlines no longer intersect the boundary. This needs to be considered especially for configurations where the boundary consists of objects of finite size. In many cases, however, T_{max} is very large compared to T_{min} and we can use $T_{max} \approx \infty$ in the evaluation of the T integral.

2.2.3 Compact expressions of $T_{00}(\vec{x}_{cp}, t)$ and $T_{zz}(\vec{x}_{cp}, t)$ for Worldline Numerics

As we have seen the components of the energy-momentum tensor are completely finite on $\mathcal{D} \setminus \partial\mathcal{D}$ by virtue of Eq. (2.31). We may therefore decompose $T_{00}(\vec{x}_{cp}, t)$ and $T_{zz}(\vec{x}_{cp}, t)$ further and study the resulting, more compact, terms one by one.

We write $T_{00}(\vec{x}_{cp}, t) = T_{00}(\vec{x}_{cp}, t)|_I + T_{00}(\vec{x}_{cp}, t)|_{II}$ with

$$T_{00}(\vec{x}_{cp}, t)|_I := \frac{1}{2} \frac{1}{(4\pi)^{\frac{d+1}{2}}} \lim_{\vec{\Delta} \rightarrow 0} \int_0^\infty \frac{dT}{T^{\frac{d+3}{2}}} e^{-\frac{\vec{\Delta}^2}{T}} \left\langle \Theta \left[\mathcal{F}(\vec{x}_{cp} + \sqrt{T}\vec{y}(t)) \right] \right\rangle_{\vec{x}_{cp}, \vec{\Delta}}, \quad (2.32a)$$

$$T_{00}(\vec{x}_{cp}, t)|_{II} := -\frac{1}{4} \frac{1}{(4\pi)^{\frac{d+1}{2}}} \lim_{\vec{\Delta} \rightarrow 0} \int_0^\infty \frac{dT}{T^{\frac{d+1}{2}}} e^{-\frac{\vec{\Delta}^2}{T}} \vec{\nabla}_{cp}^2 \left\langle \Theta \left[\mathcal{F}(\vec{x}_{cp} + \sqrt{T}\vec{y}(t)) \right] \right\rangle_{\vec{x}_{cp}, \vec{\Delta}}. \quad (2.32b)$$

With $T_{zz}(\vec{x}_{cp}, t)$ we proceed accordingly and find two terms with partial derivatives and one term with $\vec{\nabla}_{cp}^2$. All derivatives with respect to \vec{x}_{cp} or one of its components act only on the Θ function. The Δ_z derivatives, however, act on $\exp(-\vec{\Delta}^2/T)$ too. As a result,

2.2 The worldline representation of $G(\vec{x}, \vec{x}', k)$

we define four parts for $T_{zz}(\vec{x}_{cp}, t)$:

$$T_{zz}(\vec{x}_{cp}, t)|_{Ia} := -\frac{1}{4} \frac{1}{(4\pi)^{\frac{d+1}{2}}} \lim_{\vec{\Delta} \rightarrow 0} \int_0^\infty \frac{dT}{T^{\frac{d+1}{2}}} e^{-\frac{\vec{\Delta}^2}{T}} \partial_{z_{cp}}^2 \left\langle \Theta \left[\mathcal{F}(\vec{x}_{cp} + \sqrt{T}\vec{y}(t)) \right] \right\rangle_{\vec{x}_{cp}, \vec{\Delta}}, \quad (2.33a)$$

$$T_{zz}(\vec{x}_{cp}, t)|_{Ib} := \frac{1}{4} \frac{1}{(4\pi)^{\frac{d+1}{2}}} \lim_{\vec{\Delta} \rightarrow 0} \int_0^\infty \frac{dT}{T^{\frac{d+1}{2}}} e^{-\frac{\vec{\Delta}^2}{T}} \partial_{\Delta_z}^2 \left\langle \Theta \left[\mathcal{F}(\vec{x}_{cp} + \sqrt{T}\vec{y}(t)) \right] \right\rangle_{\vec{x}_{cp}, \vec{\Delta}}, \quad (2.33b)$$

$$T_{zz}(\vec{x}_{cp}, t)|_{Ic} := \frac{1}{4} \frac{1}{(4\pi)^{\frac{d+1}{2}}} \lim_{\vec{\Delta} \rightarrow 0} \int_0^\infty \frac{dT}{T^{\frac{d+1}{2}}} \left(\partial_{\Delta_z}^2 e^{-\frac{\vec{\Delta}^2}{T}} \right) \left\langle \Theta \left[\mathcal{F}(\vec{x}_{cp} + \sqrt{T}\vec{y}(t)) \right] \right\rangle_{\vec{x}_{cp}, \vec{\Delta}}, \quad (2.33c)$$

$$T_{zz}(\vec{x}_{cp}, t)|_{II} := \frac{1}{4} \frac{1}{(4\pi)^{\frac{d+1}{2}}} \lim_{\vec{\Delta} \rightarrow 0} \int_0^\infty \frac{dT}{T^{\frac{d+1}{2}}} e^{-\frac{\vec{\Delta}^2}{T}} \vec{\nabla}_{cp}^2 \left\langle \Theta \left[\mathcal{F}(\vec{x}_{cp} + \sqrt{T}\vec{y}(t)) \right] \right\rangle_{\vec{x}_{cp}, \vec{\Delta}}. \quad (2.33d)$$

We immediately see that Eq. (2.32b) and (2.33d) are identical, except for the sign. The evaluation of $\partial_{\Delta_z}^2 \exp\left(-\vec{\Delta}^2/T\right)$ for $\vec{\Delta} \rightarrow 0$, shows that Eq. (2.32a) and (2.33c) are identical except for the sign as well. These terms will cancel in the computation of the null energy condition. Hence, only four independent quantities remain.

In Eq. (2.32a) we take $\vec{\Delta} \rightarrow 0$, compute the proper-time integral and the worldline average. We do the same in Eq. (2.32b) and (2.33a), because the point-splitting limit and the \vec{x}_{cp} derivatives commute since $\vec{\Delta}$ and \vec{x}_{cp} are independent variables. The order of the T integration and the differentiation for these terms is arbitrary for the examples that we study, but the loop average is most conveniently performed last. This freedom of choice can be used to minimize numerical errors in some cases.

In Eq. (2.33b) we compute the limit of the exponential for $\vec{\Delta} \rightarrow 0$, but we cannot exchange the limit with $\partial_{\Delta_z}^2$. Furthermore, the intersection condition \mathcal{F} depends on T because the loops $\vec{y}(t)$ depend on $\vec{\delta} = \vec{\Delta}/\sqrt{T}$. This means that we can perform the proper-time integration only in the limit of closed loops. For this reason, the order of computation in $T_{zz}(\vec{x}_{cp}, t)|_{Ib}$ is completely fixed. We must act with $\partial_{\Delta_z}^2$ on the step function first. After that we can let $\vec{\Delta} \rightarrow 0$ and integrate with respect to T . The worldline average is again done in the last step.

2 Worldline Formalism for composite operators

The decomposition outlined in this paragraph shows that only four different terms need to be computed for $T_{00}(\vec{x}_{cp}, t)$ and $T_{zz}(\vec{x}_{cp}, t)$. In order to actually perform the proptime integration and differentiations in a very general way, we write the intersection condition \mathcal{F} as

$$\Theta \left[\mathcal{F}(\vec{x}_{cp} + \sqrt{T}\vec{y}(t)) \right] = \Theta \left(\sqrt{T}\mathcal{M} - 1 \right).$$

The function \mathcal{M} now describes the geometrical conditions for a worldline to intersect the boundary $\partial\mathcal{D}$. It depends on \vec{x}_{cp} and on $\vec{\delta}$. Through the latter, it also depends on T , a dependence that vanishes in the limit $\vec{\Delta} \rightarrow 0$. We note that \mathcal{M} is in general not a smooth function of these parameters. In fact, it can be non-differentiable in either variable. Since \mathcal{M} depends on the shape of the boundary $\partial\mathcal{D}$ for the specific setup that is to be studied, its functional properties must be investigated each time anew. In addition, there can be several ways in which the intersection condition \mathcal{F} may be written. These different parameterizations can exhibit very different properties during numerical evaluation. Thus, the following calculations should be understood as primarily formal.

In these formal computations, we take the function \mathcal{M} to be twice differentiable in both \vec{x}_{cp} and $\vec{\delta}$. We additionally assume that all limits exist, that they can be evaluated and that \mathcal{M} only determines a lower bound T_{min} on the proptime integral. In this case, we have $T_{min} = \mathcal{M}^{-2}$.

We start with $T_{00}(\vec{x}_{cp}, t)|_I$ in Eq. (2.32a) by exchanging the point-splitting limit with the T integration and the worldline average. The function \mathcal{M} thus no longer depends on T and we substitute the integration variable using $\mu = \sqrt{T}\mathcal{M} - 1$. Interchanging the loop average with the integration results in an integral over the Θ function which is trivial to evaluate,

$$\begin{aligned} T_{00}(\vec{x}_{cp}, t)|_I &= \frac{1}{2} \frac{1}{(4\pi)^{\frac{d+1}{2}}} \int_0^\infty \frac{dT}{T^{\frac{d+3}{2}}} \left\langle \Theta \left(\sqrt{T}\mathcal{M} - 1 \right) \right\rangle_{\vec{x}_{cp}, \vec{\Delta}=0} \\ &= \frac{1}{(4\pi)^{\frac{d+1}{2}}} \left\langle \int_{-1}^\infty \frac{d\mu}{(\mu+1)^{d+2}} \mathcal{M}^{d+1} \Theta(\mu) \right\rangle_{\vec{x}_{cp}, \vec{\Delta}=0} \\ &= \frac{1}{(4\pi)^{\frac{d+1}{2}}} \frac{1}{d+1} \langle \mathcal{M}^{d+1} \rangle_{\vec{x}_{cp}, \vec{\Delta}=0}. \end{aligned} \tag{2.34}$$

2.2 The worldline representation of $G(\vec{x}, \vec{x}', k)$

The terms $T_{00}(\vec{x}_{cp}, t)|_{II}$ and $T_{zz}(\vec{x}_{cp}, t)|_{Ia}$ in Eq. (2.32b) and (2.33a) have the same structure. This is why we will present only the calculation of $T_{zz}(\vec{x}_{cp}, t)|_{Ia}$. The calculation for $T_{00}(\vec{x}_{cp}, t)|_{II}$ can be derived by replacing the partial derivatives $\partial_{z_{cp}}$ with $\vec{\nabla}_{cp}$. As before, we evaluate the point-splitting limit first in order to remove the implicit T dependence of the unit loops. The differentiation, the proptime integration and the worldline average are interchanged so that we can act with the derivatives on the Θ function:

$$\begin{aligned}
T_{zz}(\vec{x}_{cp}, t)|_{Ia} &= -\frac{1}{4} \frac{1}{(4\pi)^{\frac{d+1}{2}}} \partial_{z_{cp}}^2 \int_0^\infty \frac{dT}{T^{\frac{d+1}{2}}} \left\langle \Theta(\sqrt{T}\mathcal{M} - 1) \right\rangle_{\vec{x}_{cp}, \vec{\Delta}=0} \\
&= -\frac{1}{4} \frac{1}{(4\pi)^{\frac{d+1}{2}}} \left\langle \int_0^\infty \frac{dT}{T^{\frac{d+1}{2}}} \partial_{z_{cp}} \left[\partial_{z_{cp}} (\sqrt{T}\mathcal{M} - 1) \partial_\mu \Theta(\mu) \right] \right\rangle_{\vec{x}_{cp}, \vec{\Delta}=0} \\
&= -\frac{1}{2} \frac{1}{(4\pi)^{\frac{d+1}{2}}} \left\langle \int_{-1}^\infty \frac{d\mu}{(\mu+1)^{d-1}} \left[\partial_{z_{cp}}^2 \mathcal{M} + \frac{\mu+1}{\mathcal{M}} (\partial_{z_{cp}} \mathcal{M})^2 \partial_\mu \right] \partial_\mu \Theta(\mu) \right\rangle_{\vec{x}_{cp}, \vec{\Delta}=0} \\
&= -\frac{1}{2} \frac{1}{(4\pi)^{\frac{d+1}{2}}} \left\langle \int_{-1}^\infty \frac{d\mu}{(\mu+1)^{d-1}} \left[\partial_{z_{cp}}^2 \mathcal{M} + \frac{d-2}{\mathcal{M}} (\partial_{z_{cp}} \mathcal{M})^2 \right] \partial_\mu \Theta(\mu) \right\rangle_{\vec{x}_{cp}, \vec{\Delta}=0} \\
&= -\frac{1}{2} \frac{1}{(4\pi)^{\frac{d+1}{2}}} \left\langle \mathcal{M}^{d-2} \partial_{z_{cp}}^2 \mathcal{M} + (d-2) \mathcal{M}^{d-3} (\partial_{z_{cp}} \mathcal{M})^2 \right\rangle_{\vec{x}_{cp}, \vec{\Delta}=0}. \tag{2.35}
\end{aligned}$$

There are two integrals, arising from integrating by parts, that we needed to discuss:

$$\begin{aligned}
\int_{-1}^\infty \frac{d\mu}{(\mu+1)^{d-2}} \partial_\mu^2 \Theta(\mu) &= \lim_{r \rightarrow -1} \frac{\partial_\mu \Theta(\mu)}{(\mu+1)^{d-2}} \Big|_r^\infty + \int_{-1}^\infty \frac{d\mu}{(\mu+1)^{d-1}} (d-2) \partial_\mu \Theta(\mu), \\
\int_{-1}^\infty \frac{d\mu}{(\mu+1)^{d-1}} \partial_\mu \Theta(\mu) &= \int_{-1}^\infty \frac{d\mu}{(\mu+1)^{d-1}} \delta(\mu) = 1
\end{aligned}$$

The boundary term for the first integration vanishes because $\partial_\mu \Theta(\mu)$ is zero everywhere except at $\mu = 0$. In the second integral we identify $\partial_\mu \Theta(\mu) = \delta(\mu)$ because the domain of integration includes $\mu = 0$. The evaluation of the integral is then trivial.

The calculation of $T_{zz}(\vec{x}_{cp}, t)|_{Ib}$ is very similar. Unlike before, we cannot exchange the differentiation and the point-splitting limit. However, we interchange the derivatives, the proptime integration, and the worldline average. The derivatives now act on the Θ function first. Since $\vec{\delta} = \vec{\Delta}/\sqrt{T}$, we cannot integrate with respect to T until we have taken

2 Worldline Formalism for composite operators

the limit $\vec{\Delta} \rightarrow 0$. The T dependence of $\mathcal{M} = \mathcal{M}(\vec{y}(\vec{\delta}))$ is not explicitly known. It thereby unambiguously defines the order of our calculations. We must evaluate the point-splitting limit before the proptime integration. Additionally, when substituting μ as integration variable we must account for the T dependence of \mathcal{M} unless we let $\vec{\delta} \rightarrow 0$ before. After evaluating this limit, the μ integration proceeds as in the previous calculation. Using a prime $'$ to denote the differentiation with respect to δ_z , one finds

$$\begin{aligned}
T_{zz}(\vec{x}_{cp}, t)|_{Ib} &= \frac{1}{4} \frac{1}{(4\pi)^{\frac{d+1}{2}}} \lim_{\vec{\Delta} \rightarrow 0} \partial_{\Delta_z}^2 \int_0^\infty \frac{dT}{T^{\frac{d+1}{2}}} \left\langle \Theta(\sqrt{T}\mathcal{M} - 1) \right\rangle_{\vec{x}_{cp}, \vec{\Delta}} \\
&= \frac{1}{4} \frac{1}{(4\pi)^{\frac{d+1}{2}}} \lim_{\vec{\Delta} \rightarrow 0} \left\langle \int_0^\infty \frac{dT}{T^{\frac{d+1}{2}}} \partial_{\Delta_z} \left[\frac{1}{\sqrt{T}} \partial_{\delta_z} (\sqrt{T}\mathcal{M} - 1) \partial_\mu \Theta(\mu) \right] \right\rangle_{\vec{x}_{cp}, \vec{\Delta}} \\
&= \frac{1}{4} \frac{1}{(4\pi)^{\frac{d+1}{2}}} \lim_{\vec{\Delta} \rightarrow 0} \left\langle \int_0^\infty \frac{dT}{T^{\frac{d+1}{2}}} \left[\frac{1}{\sqrt{T}} \mathcal{M}'' \partial_\mu \Theta(\mu) + \mathcal{M}' \mathcal{M}' \partial_\mu^2 \Theta(\mu) \right] \right\rangle_{\vec{x}_{cp}, \vec{\Delta}} \\
&\stackrel{\vec{\Delta} \rightarrow 0}{=} \frac{1}{2} \frac{1}{(4\pi)^{\frac{d+1}{2}}} \left\langle \int_{-1}^\infty \frac{d\mu}{(\mu+1)^d} \mathcal{M}^{d-1} \left[\frac{\mathcal{M}}{\mu+1} \mathcal{M}'' \partial_\mu \Theta(\mu) + \mathcal{M}' \mathcal{M}' \partial_\mu^2 \Theta(\mu) \right] \right\rangle_{\vec{x}_{cp}, \vec{\Delta}=0} \\
&= \frac{1}{2} \frac{1}{(4\pi)^{\frac{d+1}{2}}} \left\langle \mathcal{M}^d \mathcal{M}'' + d \mathcal{M}' \mathcal{M}' \mathcal{M}^{d-1} \right\rangle_{\vec{x}_{cp}, \vec{\Delta}=0}. \tag{2.37}
\end{aligned}$$

Upon integrating by parts we again encountered two integrals. They only differ from the integrals we had to compute before in the power of the denominator,

$$\begin{aligned}
\int_{-1}^\infty \frac{d\mu}{(\mu+1)^d} \partial_\mu^2 \Theta(\mu) &= \lim_{r \rightarrow -1} \left. \frac{\partial_\mu \Theta(\mu)}{(\mu+1)^d} \right|_r^\infty + \int_{-1}^\infty \frac{d\mu}{(\mu+1)^{d+1}} d \partial_\mu \Theta(\mu), \\
\int_{-1}^\infty \frac{d\mu}{(\mu+1)^{d+1}} \partial_\mu \Theta(\mu) &= \int_{-1}^\infty \frac{d\mu}{(\mu+1)^{d+1}} \delta(\mu) = 1.
\end{aligned}$$

The boundary term in the first line again vanishes because $\partial_\mu \Theta(\mu)$ is only non-vanishing at $\mu = 0$ and the evaluation of the second integral is as straightforward as before.

In this derivation we interchanged several limits, which we now justify. First, we note that all expressions we deal with are finite by construction due to the Dirichlet constraint Eq. (2.31). Since this is valid for all $\vec{\Delta}$, the limit $\vec{\Delta} \rightarrow 0$ may be interchanged with all other limits except ∂_{Δ_z} . Furthermore, since we approximate the worldline average by a finite

2.2 The worldline representation of $G(\vec{x}, \vec{x}', k)$

sum, this average can be exchanged with other limits and be conveniently computed in the end. We can also formally interchange proptime integration and differentiations because T , \vec{x}_{cp} and $\vec{\Delta}$ are independent variables. There is, however, the intersection condition \mathcal{F} , which depends on all three variables. Picturing the worldlines as paths in space helps examine the connection between these three parameters: we need not only compute the intersection condition itself but also its derivatives, that is, we need to determine how the intersection is altered if \vec{x}_{cp} or $\vec{\Delta}$ are changed.

A derivative with respect to \vec{x}_{cp} can be viewed geometrically as moving the complete worldline through space without changing its shape. On the other hand, a derivative with respect to $\vec{\Delta}$ corresponds to opening and closing the worldline at a fixed point \vec{x}_{cp} in space, changing its shape in the process. As a consequence, the derivatives of $\mathcal{F}(\vec{x}_{cp} + \sqrt{T}\vec{y}(t))$, or more specifically of \mathcal{M} , must be computed before the proptime integration. The required order in which these manipulations of the worldline expressions should be performed is then:

1. compute the derivatives of $\Theta \left[\mathcal{F}(\vec{x}_{cp} + \sqrt{T}\vec{y}(t)) \right]$ with respect to z_{cp} and δ_z ,
2. let $\vec{\Delta} \rightarrow 0$, that is, $\vec{\delta} \rightarrow 0$,
3. perform the proptime integration, and
4. average the expression over all worldlines in the ensemble.

We now summarize the four terms that we will deal with in the remainder of this thesis in their most compact form:

$$T_{00}(\vec{x}_{cp}, t)|_I = \frac{1}{(4\pi)^{\frac{d+1}{2}}} \frac{1}{d+1} \langle \mathcal{M}^{d+1} \rangle, \quad (2.39a)$$

$$T_{00}(\vec{x}_{cp}, t)|_{II} = -\frac{1}{2} \frac{1}{(4\pi)^{\frac{d+1}{2}}} \left\langle \mathcal{M}^{d-2} \left(\vec{\nabla}_{cp}^2 \mathcal{M} \right) + (d-2) \mathcal{M}^{d-3} \left(\vec{\nabla}_{cp} \mathcal{M} \right)^2 \right\rangle, \quad (2.39b)$$

$$T_{zz}(\vec{x}_{cp}, t)|_{Ia} = -\frac{1}{2} \frac{1}{(4\pi)^{\frac{d+1}{2}}} \left\langle \mathcal{M}^{d-2} \left(\partial_{z_{cp}}^2 \mathcal{M} \right) + (d-2) \mathcal{M}^{d-3} \left(\partial_{z_{cp}} \mathcal{M} \right)^2 \right\rangle, \quad (2.39c)$$

$$T_{zz}(\vec{x}_{cp}, t)|_{Ib} = \frac{1}{2} \frac{1}{(4\pi)^{\frac{d+1}{2}}} \langle \mathcal{M}^d \mathcal{M}'' + d \mathcal{M}' \mathcal{M}' \mathcal{M}^{d-1} \rangle. \quad (2.39d)$$

The worldline average is here understood to be evaluated at \vec{x}_{cp} and $\vec{\Delta} = 0$. We state once more that the above equations are still formal expressions. The issues of differentiability

2 Worldline Formalism for composite operators

of \mathcal{M} will be addressed separately for each case that we study. From the four compact and general expressions in Eq. (2.39a)-(2.39d), the complete $T_{00}(\vec{x}_{cp}, t)$ and $T_{zz}(\vec{x}_{cp}, t)$ can be constructed

$$T_{00}(\vec{x}_{cp}, t) = T_{00}(\vec{x}_{cp}, t)|_I + T_{00}(\vec{x}_{cp}, t)|_{II}, \quad (2.40)$$

$$\begin{aligned} T_{zz}(\vec{x}_{cp}, t) &= T_{zz}(\vec{x}_{cp}, t)|_{Ia} + T_{zz}(\vec{x}_{cp}, t)|_{Ib} + T_{zz}(\vec{x}_{cp}, t)|_{Ic} + T_{zz}(\vec{x}_{cp}, t)|_{II} \\ &= T_{zz}(\vec{x}_{cp}, t)|_{Ia} + T_{zz}(\vec{x}_{cp}, t)|_{Ib} - T_{00}(\vec{x}_{cp}, t)|_I - T_{00}(\vec{x}_{cp}, t)|_{II}. \end{aligned} \quad (2.41)$$

The null energy condition along the z axis now reduces to computing the sum

$$T_{00}(\vec{x}_{cp}, t) + T_{zz}(\vec{x}_{cp}, t) = T_{zz}(\vec{x}_{cp}, t)|_{Ia} + T_{zz}(\vec{x}_{cp}, t)|_{Ib}. \quad (2.42)$$

2.3 Summary

In this chapter we showed how the worldline formalism can be applied to local operators like the energy-momentum tensor of a scalar field $\hat{\Phi}(\vec{x}, t)$ coupled to a static background potential $\sigma(\vec{x})$. We were able to separate the time and spatial dependence of the field and construct a Green's function $G(\vec{x}, \vec{x}', k)$ that depends only on spatial coordinates. It was then straightforward to find a worldline description of this Green's function because it is the fundamental solution of a Schrödinger-like differential operator. The potential $\sigma(\vec{x})$ can be parameterized to impose Dirichlet boundary conditions on the field fluctuations. This renders the vacuum-subtracted Green's function $G(\vec{x}, \vec{x}', k)$ finite everywhere inside \mathcal{D} , but not on $\partial\mathcal{D}$. The numerical approach to the worldline formalism can then be used to calculate components of the EMT. The actual evaluation of these components for various configurations of boundaries is the subject of the following chapters.

3 The energy-momentum tensor for a single plate

The numerical computation of $T_{00}(\vec{x}, t)$ and $T_{zz}(\vec{x}, t)$ in $d = 2$ and $d = 3$ space dimensions in the case that $\partial\mathcal{D}$ is a single $d - 1$ -dimensional surface, i.e., a plate, is our first proof-of-principle example. The plate imposes DBCs on the fluctuations of $\hat{\Phi}(\vec{x}, t)$. It is placed at $z = 0$ such that its normal is the z axis. The single Dirichlet plate configuration is also sometimes referred to as the perfect mirror.

3.1 Analytic calculation for a single plate

Before we use worldline numerics, we compute the EMT for the single Dirichlet plate analytically. For that, we use Eq. (2.12) and compute $G(\vec{x}, \vec{x}', k)$ by solving the equation of motion Eq. (2.6) for different boundary conditions. Denoting the BCs by a superscript σ , we must solve

$$\left(-\vec{\nabla}^2 - p^2\right) \psi_p^\sigma(\vec{x}) = 0. \tag{3.1}$$

Toward that end, we decompose any $\vec{x} \in \mathcal{D}$ in the $d - 1$ -dimensional vector \vec{x}_\parallel parallel to the boundary $\partial\mathcal{D}$ and the z component of \vec{x} . The solution of Eq. (3.1) in the half space $z > 0$ with Dirichlet boundary conditions at $z = 0$ is then

$$\begin{aligned} \psi_p^\sigma(\vec{x}) &= \sqrt{2} \sin(p_z z) \exp(i\vec{p}_\parallel \cdot \vec{x}_\parallel) \\ &= \frac{\sqrt{2}}{2i} \left(e^{ip_z z} - e^{-ip_z z} \right) \exp(i\vec{p}_\parallel \cdot \vec{x}_\parallel) \\ &= \frac{\sqrt{2}}{2i} \left(\exp(i\vec{p} \cdot \vec{x}) - \exp\left(i\vec{p} \cdot \tilde{\vec{x}}\right) \right) \end{aligned} \tag{3.2a}$$

3 The energy-momentum tensor for a single plate

with $\vec{x} = (\vec{x}_{||}, z)$ and $\tilde{\vec{x}} = (\vec{x}_{||}, -z)$. In the derivation of this solution we assumed the Sommerfeld radiation condition to hold true, that is, we assumed that there are only outgoing waves at spatial infinity. In the same manner, the free solution without boundary conditions is found to be

$$\psi_p^0(\vec{x}) = \exp(i\vec{p} \cdot \vec{x}). \quad (3.3)$$

Both solutions are normalized for $z > 0$ and $z' > 0$,

$$\int \frac{d^d p}{(2\pi)^d} \psi_p^\sigma(\vec{x}) \psi_p^{\sigma*}(\vec{x}') = \delta^d(\vec{x} - \vec{x}') = \int \frac{d^d p}{(2\pi)^d} \psi_p^0(\vec{x}) \psi_p^{0*}(\vec{x}').$$

The Green's functions $G_\sigma(\vec{x}, \vec{x}', k)$ and $G_0(\vec{x}, \vec{x}', k)$ are now computed according to the spectral representation Eq. (2.8). We perform the momentum integration in polar coordinates and find (see also [45–47])

$$\begin{aligned} G_\sigma(\vec{x}, \vec{x}', k)|^{d=2} &= \frac{1}{2\pi} \left(\mathcal{K}_0(-ik|\vec{x} - \vec{x}'|) - \mathcal{K}_0(-ik|\vec{x} - \tilde{\vec{x}}'|) \right), \\ G_0(\vec{x}, \vec{x}', k)|^{d=2} &= \frac{1}{2\pi} \mathcal{K}_0(-ik|\vec{x} - \vec{x}'|), \\ G_\sigma(\vec{x}, \vec{x}', k)|^{d=3} &= \frac{1}{4\pi} \left(\frac{e^{ik|\vec{x} - \vec{x}'|}}{|\vec{x} - \vec{x}'|} - \frac{e^{ik|\vec{x} - \tilde{\vec{x}}'|}}{|\vec{x} - \tilde{\vec{x}}'|} \right), \\ G_0(\vec{x}, \vec{x}', k)|^{d=3} &= \frac{1}{4\pi} \frac{e^{ik|\vec{x} - \vec{x}'|}}{|\vec{x} - \vec{x}'|}. \end{aligned}$$

The functions \mathcal{K}_0 are modified Bessel functions of the second kind, sometimes called MacDonald functions.

Eq. (2.12) can now be solved analytically and we can even use the decomposition of $T_{00}(\vec{x}_{cp}, t)$ and $T_{zz}(\vec{x}_{cp}, t)$ that we developed in Sec. 2.2.3. When we denote the distance from the plate with z_{cp} , we find for the EMT in $d = 2$

$$\begin{aligned} T_{00}(\vec{x}_{cp}, t)|_I^{d=2} &= \frac{1}{32\pi} \frac{1}{z_{cp}^3}, & T_{00}(\vec{x}_{cp}, t)|_{II}^{d=2} &= -\frac{1}{16\pi} \frac{1}{z_{cp}^3}, \\ T_{zz}(\vec{x}_{cp}, t)|_{Ia}^{d=2} &= -\frac{1}{16\pi} \frac{1}{z_{cp}^3}, & T_{zz}(\vec{x}_{cp}, t)|_{Ib+Ic}^{d=2} &= 0. \end{aligned}$$

3.2 Worldline calculation for one Dirichlet plate

And in the case of 3 spatial dimensions the values for $T_{00}(\vec{x}_{cp}, t)$ and $T_{zz}(\vec{x}_{cp}, t)$ are

$$\begin{aligned} T_{00}(\vec{x}_{cp}, t)|_I^{d=3} &= \frac{1}{32\pi^2} \frac{1}{z_{cp}^4}, & T_{00}(\vec{x}_{cp}, t)|_{II}^{d=3} &= -\frac{3}{32\pi^2} \frac{1}{z_{cp}^4}, \\ T_{zz}(\vec{x}_{cp}, t)|_{Ia}^{d=3} &= -\frac{3}{32\pi^2} \frac{1}{z_{cp}^4}, & T_{zz}(\vec{x}_{cp}, t)|_{Ib+Ic}^{d=3} &= 0. \end{aligned}$$

The EMT components are rational functions that are proportional to $z_{cp}^{-(d+1)}$. Furthermore, we see that $T_{00}(\vec{x}_{cp}, t)|_{II} = T_{zz}(\vec{x}_{cp}, t)|_{Ia}$. We note that $T_{zz}(\vec{x}_{cp}, t)|_{Ib}$ and $T_{zz}(\vec{x}_{cp}, t)|_{Ic}$ cannot be calculated separately in a direct manner since we used the functional structure of the worldline representation of $G(\vec{x}, \vec{x}', k)$ to define these functions. Despite that, we can always compute $T_{zz}(\vec{x}_{cp}, t)|_{Ib}$ from the sum $T_{zz}(\vec{x}_{cp}, t)|_{Ib+Ic}$ using the fact that $T_{zz}(\vec{x}_{cp}, t)|_{Ic} = -T_{00}(\vec{x}_{cp}, t)|_I$. Therefore,

$$T_{zz}(\vec{x}_{cp}, t)|_{Ib}^{d=2} = \frac{1}{32\pi} \frac{1}{z_{cp}^3}, \quad T_{zz}(\vec{x}_{cp}, t)|_{Ib}^{d=3} = \frac{1}{32\pi^2} \frac{1}{z_{cp}^4}.$$

According to Eq. (2.42) the NEC along the z axis is then violated

$$T_{00}(\vec{x}_{cp}, t) + T_{zz}(\vec{x}_{cp}, t) = \begin{cases} -\frac{1}{32\pi} \frac{1}{z_{cp}^3} & \text{for } d = 2 \\ -\frac{1}{16\pi^2} \frac{1}{z_{cp}^4} & \text{for } d = 3 \end{cases}. \quad (3.7)$$

The same value for the NEC was presented in [22].

3.2 Worldline calculation for one Dirichlet plate

The first step in all our worldline calculations is the determination of the intersection condition \mathcal{F} . For the single plate setup, \mathcal{F} is easily determined from Fig. 3.1.

The loop $\vec{y}(t)$ starts at the point z_{cp} and intersects the plate at $z = 0$ for all T that fulfill $\sqrt{T}y_- + z_{cp} \leq 0$. We call the z component of the point on the loop that is closest to the plate y_- , which is negative for our choice of coordinates in the setup Fig. 3.1. We thus find for the expectation value of the Θ function

$$\begin{aligned} &\sqrt{T}y_- + z_{cp} \leq 0 \\ \implies &\Theta \left[\mathcal{F}(\vec{x}_{cp} + \sqrt{T}\vec{y}(t)) \right] = \Theta \left(\sqrt{T}\mathcal{M} - 1 \right) = \Theta \left(\sqrt{T} \frac{(-y_-)}{z_{cp}} - 1 \right). \end{aligned}$$

3 The energy-momentum tensor for a single plate

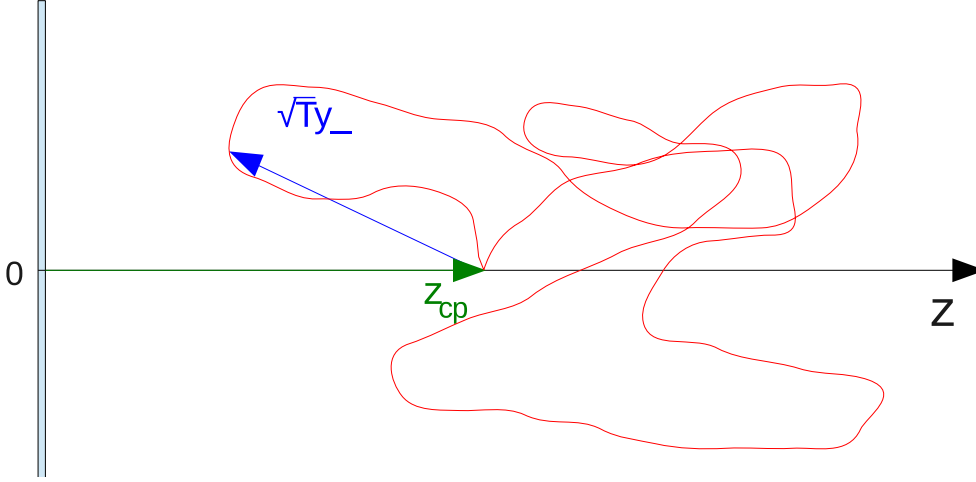


Figure 3.1 Sketch of the single plate setup with an exemplary unit loop.

The aforementioned minimal value for the proptime is obviously $T_{min} = z_{cp}^2/(-y_-)^2$, where $(-y_-)$ is now the positive distance that measures the extension of the loop towards the plate. It only depends on the z component of $\vec{y}(t)$ because the plate constrains the propagation of $\vec{y}(t)$ only in the z direction. For this reason, and because the worldline distributions factorize with respect to their position space components, we only need to calculate 1-dimensional loops. Furthermore, only one point of every loop, the point y_- , needs to be found. There is in this case no T_{max} that determines when the loop stops intersecting the boundary because if the intersection condition is fulfilled for T_{min} , it will be fulfilled for all $T > T_{min}$.

The 1-dimensional loop $y(t)$ depends on T and Δ_z through Eq. (2.26). The minimal point y_- carries the same dependence, because it is an extremal point on this loop, that is, $y_- := y(t_-)$. We have to understand this dependence in detail to be able to compute $T_{00}(\vec{x}_{cp}, t)$ and $T_{zz}(\vec{x}_{cp}, t)$. The defining equation for the extremum y_- is

$$y_- := y(t = t_-, \delta_z) \quad \Longrightarrow \quad \left. \frac{dy}{dt} \right|_{t_-} = \partial_t \mathcal{Z}(t) \Big|_{t_-} - 2\delta_z = 0. \quad (3.8)$$

This is an implicit equation for t_- which shows that t_- is a function of δ_z . Consequently, the minimal point depends on δ_z in an explicit and implicit way:

$$y_- = y(t_-(\delta_z), \delta_z). \quad (3.9)$$

3.2 Worldline calculation for one Dirichlet plate

With $\mathcal{M} = (-y_-)/z_{cp}$ we are immediately able to compute $T_{00}(\vec{x}_{cp}, t)$ and $T_{zz}(\vec{x}_{cp}, t)$ simply by inserting it into Eq. (2.39a)-(2.39d). In $T_{00}(\vec{x}_{cp}, t)|_I$, only a power of \mathcal{M} must be computed, which is very straightforward to implement numerically. There are also no difficulties in calculating $T_{00}(\vec{x}_{cp}, t)|_{II}$ and $T_{zz}(\vec{x}_{cp}, t)|_{Ia}$ as \mathcal{M} is obviously differentiable in z_{cp} . It turns out that both terms are identical since the intersection condition is only 1-dimensional. However, \mathcal{M} is not differentiable with respect to δ_z . In fact, $y(t)$ is not differentiable at all because it describes a diffusive process. As a consequence, the equation for $T_{zz}(\vec{x}_{cp}, t)|_{Ib}$ is up to now a completely formal expression. The results for all four terms are

$$T_{00}(\vec{x}_{cp}, t)|_I = \frac{1}{(4\pi)^{\frac{d+1}{2}}} \frac{1}{z_{cp}^{d+1}} \cdot \left\langle \frac{(-y_-)^{d+1}}{d+1} \right\rangle, \quad (3.10a)$$

$$T_{00}(\vec{x}_{cp}, t)|_{II} = -\frac{1}{(4\pi)^{\frac{d+1}{2}}} \frac{1}{z_{cp}^{d+1}} \cdot d \left\langle \frac{(-y_-)^{d-1}}{2} \right\rangle, \quad (3.10b)$$

$$T_{zz}(\vec{x}_{cp}, t)|_{Ia} = -\frac{1}{(4\pi)^{\frac{d+1}{2}}} \frac{1}{z_{cp}^{d+1}} \cdot d \left\langle \frac{(-y_-)^{d-1}}{2} \right\rangle, \quad (3.10c)$$

$$T_{zz}(\vec{x}_{cp}, t)|_{Ib} = \frac{1}{(4\pi)^{\frac{d+1}{2}}} \frac{1}{z_{cp}^{d+1}} \cdot \left\langle \frac{(-y_-)^d (-y_-)'' + d(-y_-)^{d-1} (-y_-)' (-y_-)'}{2} \right\rangle. \quad (3.10d)$$

Despite its formal nature, we can use Eq. (3.10d) as a description for the computation of $(-y_-)'$ and $(-y_-)''$. With the help of Eq. (3.8) and (3.9), we find

$$(-y_-)' := \frac{d}{d\delta_z} (-y_-) \Big|_{\delta_z=0} = -1 + 2t_- \Big|_{\delta_z=0}, \quad (3.11)$$

$$(-y_-)'' := \frac{d^2}{d\delta_z^2} (-y_-) \Big|_{\delta_z=0} = 2 \frac{t_-(\delta_z + h_\delta) - t_-(\delta_z - h_\delta)}{2h_\delta} \Big|_{\delta_z=0, h_\delta \rightarrow 0}. \quad (3.12)$$

The constraint Eq. (3.8) allows for an analytical form of $(-y_-)'$. For its computation only the time parameter $t_-(\delta_z = 0)$ must be determined. A similar closed form of $(-y_-)''$ does not exist because the function $t_-(\delta_z)$ is unknown. It can only be calculated numerically by using the difference quotient in Eq. (3.12) with $\delta_z = 0$ and sufficiently small h_δ . Acceptable values of h_δ will be defined within the error discussion. At this point, we only state that h_δ must be much smaller than the average extension of a loop. A very rough measure for the extension of a loop is the variance of its points $\langle e^2 \rangle = 1/6$ [38]. We thus set $h_\delta \approx 0.1 \cdot 1/6$ as a first estimate.

3 The energy-momentum tensor for a single plate

For the NEC computations of derivatives with respect to δ_z are not necessary because we know from the analytical results that $T_{zz}(\vec{x}_{cp}, t)|_{Ib+Ic} = 0$. The null energy condition along the z axis is consequently

$$T_{00}(\vec{x}_{cp}, t) + T_{zz}(\vec{x}_{cp}, t) = T_{zz}(\vec{x}_{cp}, t)|_{Ia} + T_{00}(\vec{x}_{cp}, t)|_{Ia}.$$

The calculation of the condition $T_{zz}(\vec{x}_{cp}, t)|_{Ib} = T_{00}(\vec{x}_{cp}, t)|_{Ia}$ is hence an additional check of our algorithm.

3.3 Numerical results for $T_{00}(\vec{x}_{cp}, t)$ and $T_{zz}(\vec{x}_{cp}, t)$

We now compare our numerical with the analytical results. Starting with the single plate in $d = 2$ dimensions, we recall the terms of $T_{00}(\vec{x}_{cp}, t)$ and $T_{zz}(\vec{x}_{cp}, t)$

$$\begin{aligned} T_{00}(\vec{x}_{cp}, t)|_I^{d=2} &= \frac{1}{32\pi} \frac{1}{z_{cp}^3} \cdot \frac{4}{3\sqrt{\pi}} \langle (-y_-)^3 \rangle && \stackrel{!}{=} \frac{1}{32\pi} \frac{1}{z_{cp}^3}, \\ T_{zz}(\vec{x}_{cp}, t)|_{Ia}^{d=2} &= -\frac{1}{16\pi} \frac{1}{z_{cp}^3} \cdot \frac{2}{\sqrt{\pi}} \langle (-y_-) \rangle && \stackrel{!}{=} -\frac{1}{16\pi} \frac{1}{z_{cp}^3}, \\ T_{zz}(\vec{x}_{cp}, t)|_{Ib}^{d=2} &= \frac{1}{32\pi} \frac{1}{z_{cp}^3} \cdot \frac{2}{\sqrt{\pi}} \langle (-y_-)^2 (-y_-)'' + 2(-y_-)(-y_-)'^2 \rangle && \stackrel{!}{=} \frac{1}{32\pi} \frac{1}{z_{cp}^3}. \end{aligned}$$

From these equations we immediately deduce the analytical values which our three worldline averages must approach. Tab. 3.1 shows our numerical data in $d = 2$ dimensions for an ensemble of $25 \cdot 10^3$ worldlines with 2^{14} points per loop. Ensembles with such parameters have proved to give good first estimates while still allowing for fast computations.

Our worldline algorithms already yield results that are close to their analytical values with these parameters. And the statistical errors given by the standard deviation of the ensemble are well below 3%.

The $d = 3$ case is of course handled in the same manner. When we compare with the analytical results, we find

$$\begin{aligned} T_{00}(\vec{x}_{cp}, t)|_I^{d=3} &= \frac{1}{32\pi^2} \frac{1}{z_{cp}^4} \cdot \frac{1}{2} \langle (-y_-)^4 \rangle && \stackrel{!}{=} \frac{1}{32\pi^2} \frac{1}{z_{cp}^4}, \\ T_{zz}(\vec{x}_{cp}, t)|_{Ia}^{d=3} &= -\frac{3}{32\pi^2} \frac{1}{z_{cp}^4} \cdot \langle (-y_-)^2 \rangle && \stackrel{!}{=} -\frac{3}{32\pi^2} \frac{1}{z_{cp}^4}, \\ T_{zz}(\vec{x}_{cp}, t)|_{Ib}^{d=3} &= \frac{1}{32\pi^2} \frac{1}{z_{cp}^4} \cdot \langle (-y_-)^3 (-y_-)'' + 3(-y_-)^2 (-y_-)'^2 \rangle && \stackrel{!}{=} \frac{1}{32\pi^2} \frac{1}{z_{cp}^4}, \end{aligned}$$

3.3 Numerical results for $T_{00}(\vec{x}_{cp}, t)$ and $T_{zz}(\vec{x}_{cp}, t)$

$\frac{1}{2}\sqrt{\pi}$	$\langle(-y_-)\rangle$	Δ_{stat}
0.886227	0.880224 ± 0.002944	0.33 %
$\frac{3}{4}\sqrt{\pi}$	$\langle(-y_-)^3\rangle$	Δ_{stat}
1.32934	1.32213 ± 0.01342	1.02 %
$\frac{1}{2}\sqrt{\pi}$	$\langle(-y_-)^2(-y_-)'' + 2(-y_-)(-y_-')^2\rangle$	Δ_{stat}
0.886227	0.878668 ± 0.019890	2.26 %

Table 3.1 Numerical results for the single plate in $d = 2$ with an ensemble of 25 000 loops, 2^{14} points per loop and $h_\delta = 0.0166$. The errors given are the standard deviations of the ensemble. The systematic errors have not yet been included.

from which we can read off the continuum limits of our averages. In Tab. 3.2 we show how

1	$\langle(-y_-)^2\rangle$	Δ_{stat}
1.00000	0.991527 ± 0.006396	0.65 %
2	$\langle(-y_-)^4\rangle$	Δ_{stat}
2.000000	2.00568 ± 0.03032	1.51 %
1	$\langle(-y_-)^3(-y_-)'' + 3(-y_-)^2(-y_-')^2\rangle$	Δ_{stat}
1.000000	0.990381 ± 0.024271	2.45 %

Table 3.2 Numerical results for the single plate in 3 space dimensions with an ensemble of 25 000 loops, 2^{14} points per loop and $h_\delta = 0.0166$. The errors given are the standard deviations of the ensemble. The systematic errors have not yet been included.

well our numerical calculation, using the same ensemble as in the $d = 2$ case, approaches these limits. We see again a good agreement between the numerical and analytical values for the EMT components. The statistical errors are also within a 3% margin. Although there is still room for improvement by a detailed analysis of errors, we can already conclude that our numerical algorithm works very well. It reproduces analytical results for the single plate within a few percent for modest values of ensemble parameters.

3.3.1 Error analysis for the computation of $\langle -y_- \rangle$

As with any Monte-Carlo method there are statistical and systematic errors. The statistical error is determined by the number of loops N in the ensemble. Only for large N does the arithmetic mean in Eq. (2.29) converge to the value of the expectation value of the path integral. We use the standard deviation of the ensemble, which is proportional to $\sqrt{1/N}$, as a measure for this statistical error. Since the computational costs of our worldline algorithms scale linearly with N , the standard deviation is readily controlled.

The systematic errors in our calculations arise from two different sources. The first comes from the discretization of the loops themselves. This error is controlled by the number of points per loop n_{ppl} . The discretized loops become smoother and better approximate the continuous loops the larger n_{ppl} becomes. Since the worldlines between two points are approximated by straight lines, the discretized loops are “smaller” than the continuous worldlines, and the the results of the continuum limit are approached from below by the numerical data. In Fig. 3.2 we show this by plotting our worldline results for $\langle (-y_-)^r \rangle$ with $r \in \{1, 2, 3, 4\}$ against $1/n_{ppl}$. We see that for increasing number of points per loop, the numerical data approach the analytical values. For $n_{ppl} > 2^{14}$ the numerical values are within a 5 % margin of their analytical values. One can also observe that the deviations from the analytical values are smallest for $\langle (-y_-) \rangle$ and largest for $\langle (-y_-)^4 \rangle$.

We fitted our worldline data with a function $a + b/n_{ppl}$, disregarding the error bars as they do not vary much for different n_{ppl} . From these fits we derive the systematic error as a difference between the analytical value and the fit. It can consume significant computertime to minimize this error. Even though our algorithms scale linearly with n_{ppl} , we can only change the number of points per loop in multiples of 2, since we use the d loop algorithm for the generation of the loops. As a consequence, computation time doubles for every increase in n_{ppl} . While the calculation of an ensemble of 25 000 loops with $n_{ppl} = 2^{14}$ takes only a few minutes on any ordinary PC, it takes a few hours if n_{ppl} is increased to 2^{20} . For larger n_{ppl} , it is therefore more suitable to split up the computation of the worldline average into the “embarrassingly parallel” computation of several smaller ensembles. Especially, if both N and n_{ppl} need to be increased, this parallelization is an easy way to reduce the effective time of the calculation.

The second systematic error is introduced by the difference quotient used to compute the

3.3 Numerical results for $T_{00}(\vec{x}_{cp}, t)$ and $T_{zz}(\vec{x}_{cp}, t)$

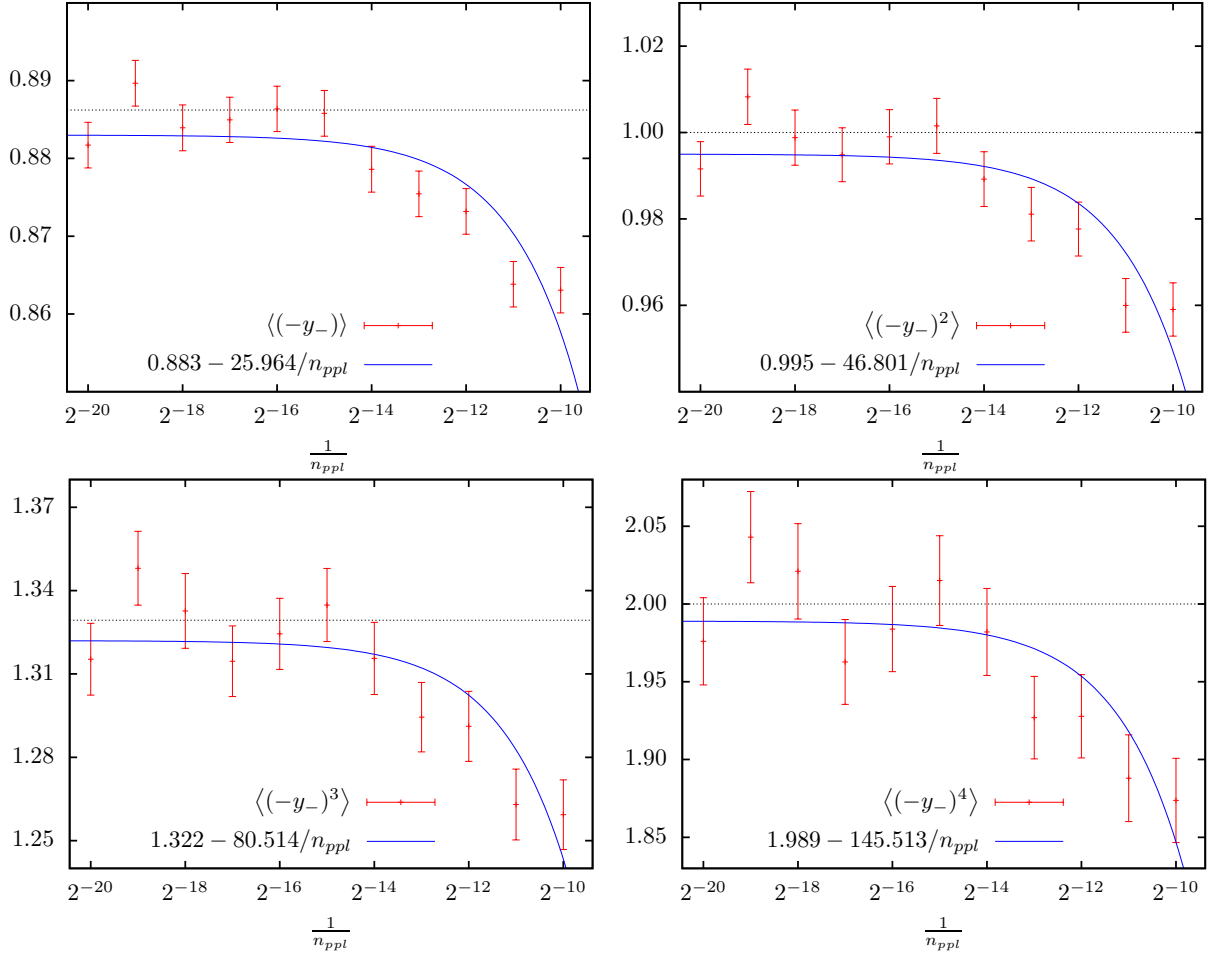


Figure 3.2 Systematic error of $\langle(-y_-)^r\rangle$ with $r \in \{1, 2, 3, 4\}$ for $n_{ppl} = 2^{10} \dots 2^{20}$. The solid curves are fits and the dotted lines are the respective analytical values.

derivatives of the minimal point $\langle(-y_-)\rangle$. From Eq. (3.12) we see that for the numerator to be non-vanishing, h_δ should be at least of the order of the average distance between points. Only then are different points along the loop the extremal point closest to the boundary. At the same time, h_δ must be small compared to the extension of the entire loop. The variance of the points of the loop $\langle e^2 \rangle = 1/6$ gives a crude estimate of the extension of the loop. For the average distance between points, we use

$$\sqrt{\left\langle \sum_{i=0}^{n_{ppl}} (y_{i+1} - y_i)^2 / n_{ppl} \right\rangle} \propto \sqrt{2/n_{ppl}}.$$

It must be noted that both parameters are only rough measures and become good ap-

3 The energy-momentum tensor for a single plate

proximations only for large N and n_{ppl} . Combining both requirements we find

$$\begin{aligned}
 h_\delta &\ll \frac{1}{6}, & h_\delta &= \sqrt{\frac{2}{n_{ppl}}} \cdot f \quad \text{with } f \gtrsim \mathcal{O}(1) \\
 \implies f &= \frac{\varepsilon}{6} \cdot \sqrt{\frac{n_{ppl}}{2}} \quad \text{with } \varepsilon \ll 1.
 \end{aligned}
 \tag{3.14}$$

Since Eq. (3.14) is just a rough estimate, we determine f empirically and compute $\langle(-y_-)''\rangle$ for three different ensembles with $25 \cdot 10^3$ loops and $n_{ppl} = 2^{10} \dots 2^{20}$ for several values $h_\delta = f \sqrt{2/n_{ppl}}$. We expect to find large errors for small values of f , especially for $f \leq 1$ because these values violate our requirement Eq. (3.14). For intermediate values of f there should be a acceptable plateau region beyond which the values of $\langle(-y_-)''\rangle$ deviate non-linearly for too large f because a linearization is not a good enough approximation for the derivative anymore.

Fig. 3.3 shows $\langle(-y_-)''\rangle$ for three ensembles with 2^{10} points per loop. The solid line in the plot is only for reference and comparison with the other plots, not an analytical value. For values $f < 1$ we observe large deviations and also large statistical errors. For f that small, the numerator in Eq. (3.12) is zero for too many loops and only very few loops contribute to the worldline average. For larger f , the statistical errors decrease and the results of all three ensembles agree very well, but they also drift from the values for $f = 1$. The second plot in Fig. 3.3 shows this behavior for a larger domain of f values. The numerical result of $\langle(-y_-)''\rangle$ decreases and drifts from initial and intermediate results with increasing f . Here we also see that $\langle(-y_-)''\rangle$ is, as expected, not a linear function of f . The values $f = 1.0 \dots 1.5$ seem to be an optimal choice for calculations with such small N and n_{ppl} , even though a plateau is only barely observable. Due to the large systematic errors for such a small number of points per loop, we consider 2^{10} too small a value of n_{ppl} to perform calculations. For a larger number of points per loop, 2^{14} and above, the systematic errors are smaller and we expect to be able to make a better estimate.

Indeed, we can see in Fig. 3.4 that $\langle(-y_-)''\rangle$ deviates less strongly for intermediate values $f = 1.0 \dots 4.0$ if $n_{ppl} = 2^{14}$. In the region $f < 1$ the statistical errors are large as before. For $f > 1$, however, the results are hardly drifting from the reference line. This region can be considered a plateau and one can use $f = 2.5 \dots 4.0$ as a good estimate. These values correspond to $\varepsilon = 0.17 \dots 0.27$ in Eq. (3.14) and hence fulfill the requirements

3.3 Numerical results for $T_{00}(\vec{x}_{cp}, t)$ and $T_{zz}(\vec{x}_{cp}, t)$

we have set for h_δ . If f is increased further, we observe the drift from the reference again, even though it is not as pronounced as for $n_{ppl} = 2^{10}$. We conclude that 2^{14} should be the smallest number of points per loop used in our calculations. For smaller n_{ppl} it will become increasingly difficult to estimate optimal values for f . Coincidentally, 2^{14} is also the minimal number of points per loop for which the systematic errors of the cumulants of the minimal point are below 5%.

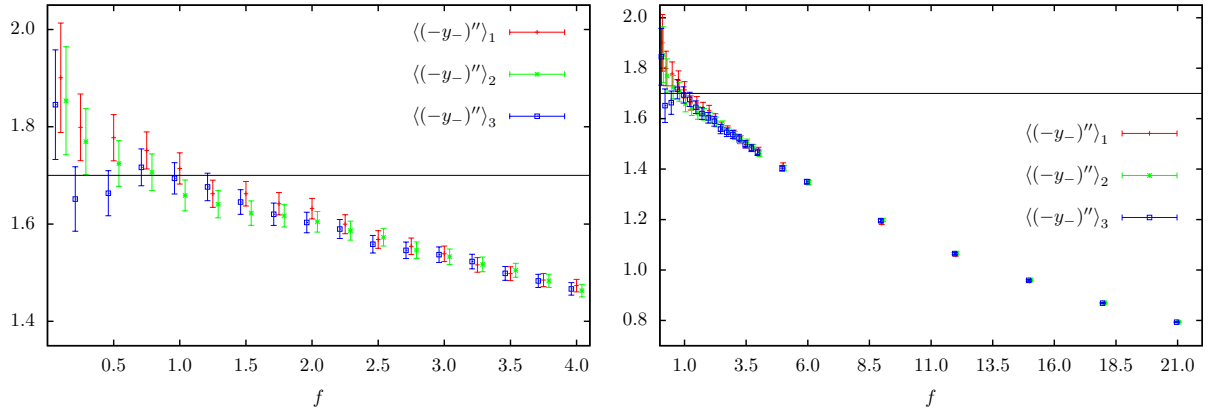


Figure 3.3 Systematic errors of $\langle(-y_-)''\rangle$ computed with three ensembles of $N = 25 \cdot 10^3$ and $n_{ppl} = 2^{10}$. The three sets of data points have been slightly shifted horizontally to be distinguishable in the plot. The solid black line is only for reference and comparison between different figures.

In order to gain a better overview of the behavior of f with increasing n_{ppl} , we study two more sets of worldline ensembles, one with 2^{17} (Fig. 3.5) and another with 2^{20} (Fig. 3.6) points per loop. For both of them we can reiterate our findings from above. If $f \leq 1$ there are large errors and deviations among the three represented ensembles. Beginning at around $f \approx 1$ the errors and deviations decrease and we see a plateau region from which an optimal value of f can be estimated for our calculations. This plateau region extends to larger f for increasing n_{ppl} . For even larger values of f the numerical data decrease and drift away from the common reference value. We estimate the optimal value of f for $n_{ppl} = 2^{17}$ to be in the region $f = 2.5 \dots 8.0$ corresponding to $\varepsilon = 0.059 \dots 0.188$. However, even for $f = 21$ we find a value of $\langle(-y_-)''\rangle$ closer to the common reference value than for $f = 21$ with $n_{ppl} = 2^{14}$. In Eq. (3.14) $f = 21$ corresponds to $\varepsilon = 1.39$ for $n_{ppl} = 2^{14}$, which violates the conditions for h_δ , but $\varepsilon = 0.49$ for $n_{ppl} = 2^{17}$. The results

3 The energy-momentum tensor for a single plate

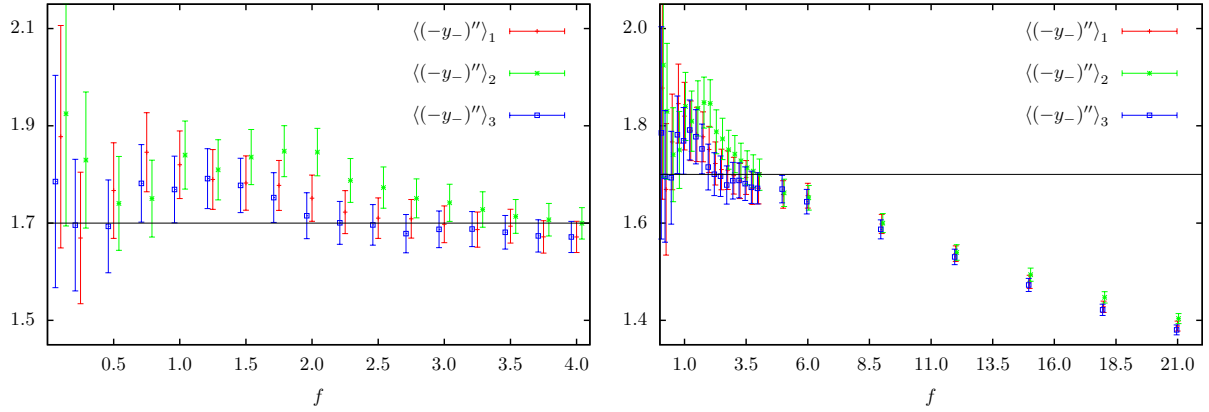


Figure 3.4 Systematic errors of $\langle(-y_-)''\rangle$ computed with three ensembles with $N = 25 \cdot 10^3$ and $n_{ppl} = 2^{14}$. The three sets of data points have been slightly shifted horizontally to be distinguishable in the plot. The solid black line is only for reference and comparison between different figures.

for $n_{ppl} = 2^{20}$ again look similar. The plateau region extends to even larger values of f . From Fig. 3.6 we estimate $f = 9.0 \dots 25.0$ to be optimal values. And indeed these values correspond to $\varepsilon = 0.07 \dots 0.21$. For even larger f the results drift from our reference value.

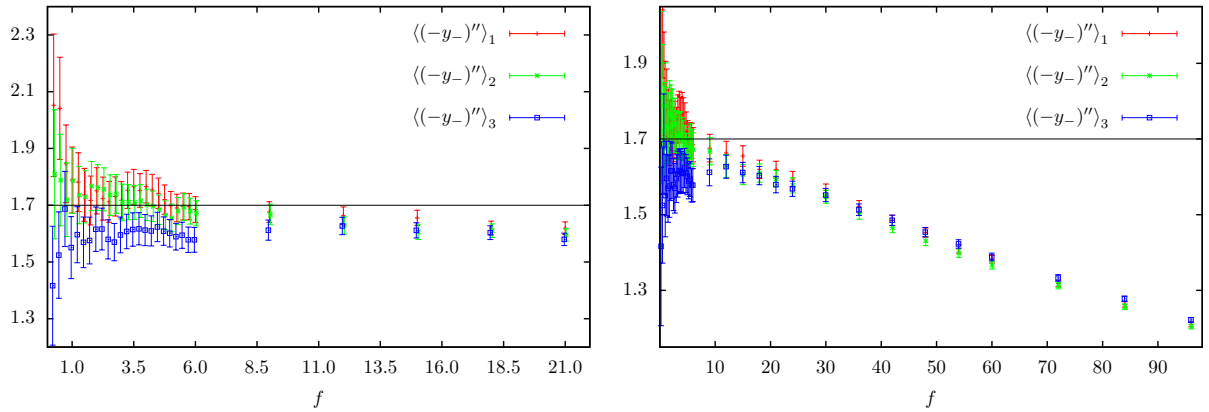


Figure 3.5 Systematic errors of $\langle(-y_-)''\rangle$ computed with three ensembles with $N = 25 \cdot 10^3$ and $n_{ppl} = 2^{17}$. The three sets of data points have been slightly shifted horizontally to be distinguishable in the plot. The solid black line is only for reference and comparison between different figures.

From the figures above, we deduce optimal values for f as a function of n_{ppl} . Those

3.3 Numerical results for $T_{00}(\vec{x}_{cp}, t)$ and $T_{zz}(\vec{x}_{cp}, t)$

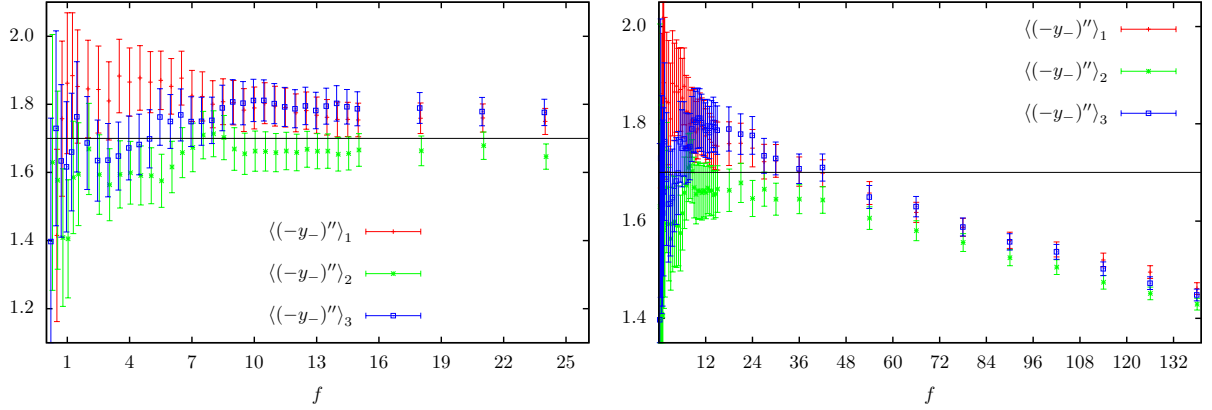


Figure 3.6 Systematic errors of $\langle(-y_-)''\rangle$ computed with three ensembles with $N = 25 \cdot 10^3$ and $n_{ppl} = 2^{20}$. The three sets of data points have been slightly shifted horizontally to be distinguishable in the plot. The solid black line is only for reference and comparison between different figures.

values are compiled in Tab. 3.3. We estimate the optimal f for those values of n_{ppl} for which we have not run the actual calculation, such that the corresponding ε are approximately 0.1. Those values are consistent with the constraint in Eq. (3.14).

We deduce the systematic errors of the cumulants of $(-y_-)$ from the fits in Fig. 3.2. Similarly we determine the systematic errors of the averages which contain derivatives of $(-y_-)$ by computing these terms for different values of n_{ppl} and the corresponding optimal value of f . Fig. 3.7 shows the results of these calculations and concludes our error discussion for the single Dirichlet plate. With the plots and optimal f values from above, we are now able to rerun our numerical calculation with minimized errors.

3 The energy-momentum tensor for a single plate

n_{ppl}	allowed f	allowed ε	optimal f	optimal ε
2^{10}	1.0...1.5	0.265...0.398	1.0	0.265
2^{11}			1.0	0.188
2^{12}			1.25	0.166
2^{13}			1.5	0.141
2^{14}	2.0...4.0	0.133...0.265	2.0	0.133
2^{15}			2.75	0.130
2^{16}			3.5	0.116
2^{17}	2.5...8.0	0.059...0.188	4.0	0.094
2^{18}			6.0	0.099
2^{19}			8.0	0.094
2^{20}	9.0...25.0	0.075...0.207	12.0	0.099

Table 3.3 The optimal values for f and ε , respectively. We determined them from Fig. 3.3-3.6 or estimated them such that $\varepsilon \approx 0.1$.

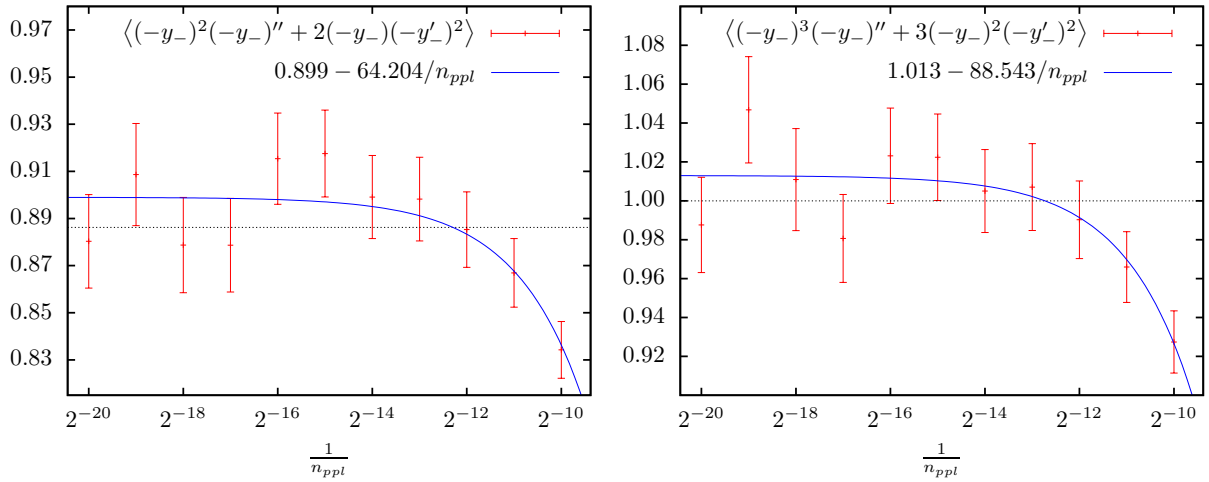


Figure 3.7 Systematic error of the derivative terms in $d = 2$ and $d = 3$ for $n_{ppl} = 2^{10} \dots 2^{20}$, $N = 25 \cdot 10^3$ and $f = 2.0$. The solid curves are fits and the dotted lines are the respective analytical values.

3.3.2 Numerical results for minimized systematic and statistical errors

In order to compute $T_{00}(\vec{x}_{cp}, t)$ and $T_{zz}(\vec{x}_{cp}, t)$ with minimal errors we use an ensemble of $N = 5 \cdot 10^5$ worldlines with $n_{ppl} = 2^{20}$ points per loop and choose $f = 12$ ($\varepsilon = 0.099$). The statistical errors are measured by the standard deviation. For the systematic error is estimated by the difference between analytical values and fits for $n_{ppl} \rightarrow \infty$. In Tab. 3.4 the worldline results are summarized for these optimized parameters.

$\frac{1}{2}\sqrt{\pi}$	$\langle(-y_-)\rangle$	Δ_{stat}	Δ_{sys}	Δ_{comp}
0.88623	0.88502 ± 0.00065	0.073 %	0.339 %	0.412 %
1	$\langle(-y_-)^2\rangle$	Δ_{stat}	Δ_{sys}	Δ_{comp}
1.00000	0.99715 ± 0.00141	0.141 %	0.500 %	0.641 %
$\frac{3}{4}\sqrt{\pi}$	$\langle(-y_-)^3\rangle$	Δ_{stat}	Δ_{sys}	Δ_{comp}
1.32934	1.32337 ± 0.00289	0.218 %	0.527 %	0.745 %
2	$\langle(-y_-)^4\rangle$	Δ_{stat}	Δ_{sys}	Δ_{comp}
2.00000	1.98702 ± 0.00626	0.315 %	0.550 %	0.865 %
$\frac{1}{2}\sqrt{\pi}$	$\langle(-y_-)^2(-y_-)'' + 2(-y_-)(-y_-)'\rangle$	Δ_{stat}	Δ_{sys}	Δ_{comp}
0.88623	0.89190 ± 0.00452	0.507 %	1.467 %	1.974 %
1	$\langle(-y_-)^3(-y_-)'' + 3(-y_-)^2(-y_-)'\rangle$	Δ_{stat}	Δ_{sys}	Δ_{comp}
1.00000	1.00103 ± 0.00561	0.560 %	1.300 %	1.860 %

Table 3.4 Numerical results for the single plate in 3 and 2 spatial dimensions with an ensemble of $5 \cdot 10^5$ loops, 2^{20} points per loop and $f = 12$, that is, $h_\delta = 12 \cdot \sqrt{2/n_{ppl}}$. The statistical and systematic errors are shown explicitly as well as the complete error Δ_{comp} .

We see that the statistical errors have decreased to well below 1 %, due to the increase in N , and the systematic errors are smaller than 1.5 %. They are larger for higher powers of $(-y_-)$. The errors of the derivative terms are generally larger. They contain not only the systematic error for the point $(-y_-)$, determined by n_{ppl} , but also the error due to

the linearization of the derivatives, determined by h_δ .

3.4 Conclusions

We have shown that worldline numerics can be used to calculate expectation values of composite operators. We presented in a detailed way how to calculate the EMT induced by a fluctuating scalar field that is constrained by Dirichlet BCs on a single plate. The single plate configuration constitutes our first proof-of-principle example. Contrary to the computation of effective actions, for local operators not only powers but also derivatives of loop variables need to be evaluated. The systematic and statistical errors arise due to the discretization of the worldlines and the path integral can be controlled by the number of loops N and the number of points per loop n_{ppl} . For large values of N and n_{ppl} , these errors amount to about 1%. The linearization of derivatives introduces an additional systematic error. We showed how one can estimate it by an extrapolation of the numerical data for large n_{ppl} . This error is then also of the order of 1%. Keeping in mind that the loop variables are, strictly speaking, non-differentiable functions, we regard such a small error for the derivatives a success of our algorithm. If we consider the single plate configuration as a first test, then our worldline algorithm has passed since it yields high precision results at low cost in terms of computation time and memory.

4 The energy-momentum tensor for Casimir's parallel plates

The second proof-of-principle example is the case of two parallel plates with Dirichlet boundary conditions. This configuration corresponds to the original setup studied by Casimir for the electromagnetic field [1]. As in the previous chapter, we compute $T_{00}(\vec{x}, t)$ and $T_{zz}(\vec{x}, t)$ in $d = 2$ and $d = 3$ space dimensions. With these terms, we can see if the null energy condition is violated or fulfilled. The plates are placed symmetrically around the origin $z = 0$. The z axis is perpendicular to the plates and their distance from one another is denoted by a . The whole configuration is invariant under arbitrary translations parallel to the plates.

4.1 Analytical calculation for two parallel plates

$\hat{T}_{\mu\nu}(\vec{x}, t)$ for two parallel Dirichlet plates can be calculated analytically in the same way as for the single plate, by applying the method of images and using the results of Sec. 3.1 for the Green's functions. The two plates at $z = a/2$ and $z = -a/2$ constitute the boundary and decompose the domain \mathcal{D} into three disjoint regions. In the outside region $z > a/2$, we find the Green's function for a single plate at $z = a/2$ and in the region and $z < -a/2$ the Green's function of a single plate at $z = -a/2$. The Green's function between the plates is given by the method of images as an infinite series of image charges induced on the plates by a point source. For arbitrary \vec{x} and \vec{x}' that lie between the plates, i.e., for which $|z| < a/2$ and $|z'| < a/2$, we introduce the vectors $\vec{x}_q := (\vec{x}_{||}, z + 2qa)$ and

4 The energy-momentum tensor for Casimir's parallel plates

$\tilde{x}_q := (\vec{x}_{||}, -z + (2q + 1)a)$. The Green's functions are then

$$G_\sigma(\vec{x}, \vec{x}', k)|^{d=2} = \frac{1}{2\pi} \sum_{q \in \mathbb{Z}} \left(\mathcal{K}_0(-ik|\vec{x}_q - \vec{x}'|) - \mathcal{K}_0(-ik|\tilde{x}_q - \vec{x}'|) \right),$$

$$G_0(\vec{x}, \vec{x}', k)|^{d=2} = \frac{1}{2\pi} \mathcal{K}_0(-ik|\vec{x}_{q=0} - \vec{x}'|),$$

$$G_\sigma(\vec{x}, \vec{x}', k)|^{d=3} = \frac{1}{4\pi} \sum_{q \in \mathbb{Z}} \left(\frac{e^{ik|\vec{x}_q - \vec{x}'|}}{|\vec{x}_q - \vec{x}'|} - \frac{e^{ik|\tilde{x}_q - \vec{x}'|}}{|\tilde{x}_q - \vec{x}'|} \right),$$

$$G_0(\vec{x}, \vec{x}', k)|^{d=3} = \frac{1}{4\pi} \frac{e^{ik|\vec{x}_{q=0} - \vec{x}'|}}{|\vec{x}_{q=0} - \vec{x}'|}.$$

After inserting these Green's functions into Eq. (2.12), we integrate with respect to k . The result is further simplified by assuming \vec{x} and \vec{x}' to lie on the z axis, that is, $\vec{x}_{||} = \vec{x}'_{||}$. The various EMT components can now be written in the form of a series

$$\zeta(s, f(z_{cp}, \Delta_z)) := \sum_{q=0}^{\infty} (f(z_{cp}, \Delta_z) + q)^{-s}, \quad (4.2)$$

which is a Hurwitz ζ function for $\text{Re}(s) > 1$ and $\text{Re}(f(z_{cp}, \Delta_z)) > 0$. While we always have $f(z_{cp}, \Delta_z) > 0$, for $d = 2$ we find $s = 1$ in $T_{zz}(\vec{x}_{cp}, t)$. We solve this problem by acting with the derivatives $\partial_{z_{cp}}$ and ∂_{Δ_z} , which increases the exponent to $s = 3$.

In 2 spatial dimensions the EMT between the plates, that is, for $|z_{cp}| < a/2$, is given by the components

$$T_{00}(\vec{x}_{cp}, t)|_I^{d=2} = -\frac{1}{32\pi a^3} \left[2\zeta(3) - \zeta\left(3, \frac{1}{2} + \frac{z_{cp}}{a}\right) - \zeta\left(3, \frac{1}{2} - \frac{z_{cp}}{a}\right) \right],$$

$$T_{00}(\vec{x}_{cp}, t)|_{II}^{d=2} = -\frac{1}{16\pi a^3} \left[\zeta\left(3, \frac{1}{2} + \frac{z_{cp}}{a}\right) + \zeta\left(3, \frac{1}{2} - \frac{z_{cp}}{a}\right) \right],$$

$$T_{zz}(\vec{x}_{cp}, t)|_{Ia}^{d=2} = -\frac{1}{16\pi a^3} \left[\zeta\left(3, \frac{1}{2} + \frac{z_{cp}}{a}\right) + \zeta\left(3, \frac{1}{2} - \frac{z_{cp}}{a}\right) \right],$$

$$T_{zz}(\vec{x}_{cp}, t)|_{Ib+Ic}^{d=2} = -\frac{1}{16\pi a^3} 2\zeta(3).$$

4.1 Analytical calculation for two parallel plates

The corresponding 3-dimensional results are

$$\begin{aligned}
T_{00}(\vec{x}_{cp}, t)|_I^{d=3} &= -\frac{1}{32\pi^2 a^4} \left[2\zeta(4) - \zeta\left(4, \frac{1}{2} + \frac{z_{cp}}{a}\right) - \zeta\left(4, \frac{1}{2} - \frac{z_{cp}}{a}\right) \right], \\
T_{00}(\vec{x}_{cp}, t)|_{II}^{d=3} &= -\frac{3}{32\pi^2 a^4} \left[\zeta\left(4, \frac{1}{2} + \frac{z_{cp}}{a}\right) + \zeta\left(4, \frac{1}{2} - \frac{z_{cp}}{a}\right) \right], \\
T_{zz}(\vec{x}_{cp}, t)|_{Ia}^{d=3} &= -\frac{3}{32\pi^2 a^4} \left[\zeta\left(4, \frac{1}{2} + \frac{z_{cp}}{a}\right) + \zeta\left(4, \frac{1}{2} - \frac{z_{cp}}{a}\right) \right], \\
T_{zz}(\vec{x}_{cp}, t)|_{Ib+Ic}^{d=3} &= -\frac{3}{32\pi^2 a^4} 2\zeta(4).
\end{aligned}$$

As we mentioned before $T_{00}(\vec{x}_{cp}, t)|_{Ia} = -T_{zz}(\vec{x}_{cp}, t)|_{Ic}$ and as a result we can also write the components

$$T_{zz}(\vec{x}_{cp}, t)|_{Ib}^{d=2} = -\frac{1}{32\pi a^3} \left[6\zeta(3) - \zeta\left(3, \frac{1}{2} + \frac{z_{cp}}{a}\right) - \zeta\left(3, \frac{1}{2} - \frac{z_{cp}}{a}\right) \right], \quad (4.5)$$

$$T_{zz}(\vec{x}_{cp}, t)|_{Ib}^{d=3} = -\frac{1}{32\pi^2 a^4} \left[8\zeta(4) - \zeta\left(4, \frac{1}{2} + \frac{z_{cp}}{a}\right) - \zeta\left(4, \frac{1}{2} - \frac{z_{cp}}{a}\right) \right]. \quad (4.6)$$

We see once more that $T_{00}(\vec{x}_{cp}, t)|_{II} = T_{zz}(\vec{x}_{cp}, t)|_{Ia}$ because the Dirichlet BCs are a constraint in one space dimension only. The EMT components diverge as the distance from either plate goes to zero. The EMT for the electromagnetic field with perfect conductor boundary conditions does not show those divergences, but instead is finite [29]. However, the electromagnetic EMT has zero trace because the electromagnetic field is conformally invariant. A minimally coupled massless scalar field does not have this additional symmetry. In order to arrive at a finite EMT, we can either couple the scalar field conformally to the background potential or compute the conformal complement [48].

The analytical NEC along the z axis between the plates is also violated in the case of two parallel plates,

$$T_{00}(\vec{x}_{cp}, t) + T_{zz}(\vec{x}_{cp}, t) = \begin{cases} \frac{-1}{32\pi a^3} \left[6\zeta(3) + \zeta\left(3, \frac{1}{2} + \frac{z_{cp}}{a}\right) + \zeta\left(3, \frac{1}{2} - \frac{z_{cp}}{a}\right) \right] & \text{for } d = 2 \\ \frac{-1}{16\pi^2 a^4} \left[4\zeta(4) + \zeta\left(4, \frac{1}{2} + \frac{z_{cp}}{a}\right) + \zeta\left(4, \frac{1}{2} - \frac{z_{cp}}{a}\right) \right] & \text{for } d = 3 \end{cases}, \quad (4.7)$$

because the ζ -functions are positive and both expressions have a negative coefficient. Our are identical to the ones in [30].

4.1.1 The conformal complement of $\hat{T}_{\mu\nu}(\vec{x}, t)$

The energy-momentum tensor derived for a conformally coupled scalar field does not diverge when approaching the boundary but it still yields the same total energy and momentum. The difference between both energy-momentum tensors is the conformal complement $\Delta\hat{T}_{\mu\nu}(\vec{x}, t)$ defined by [48]

$$\Delta\hat{T}_{\mu\nu}(\vec{x}, t) := -\xi (\partial_\mu\partial_\nu - g_{\mu\nu}g^{\alpha\beta}\partial_\alpha\partial_\beta) \hat{\Phi}(\vec{x}, t)\hat{\Phi}(\vec{x}, t),$$

where $\xi = \frac{d-1}{4d}$. Adding the vacuum expectation value of the components of this conformal complement operator to our canonical EMT removes the divergent terms of the latter. Alternatively, one can write down a Lagrangian density similar to Eq. (2.1) in a general curved spacetime and compute an energy-momentum tensor by varying with respect to the metric. When the general metric in the new EMT is then replaced with the Minkowski metric, the two energy-momentum tensors will differ in the term $\Delta\hat{T}_{\mu\nu}(\vec{x}, t)$.

We want to make some further remarks about these two energy-momentum tensors. One obtains the total energy and momentum from the energy-momentum tensor by integrating it over the entire spacetime volume. The canonical and conformal EMT define the same total energy and momentum because they differ by a total derivative. Under the spacetime volume integration this total derivative can be written as a boundary term at infinity after an integration by parts. The boundary term then vanishes because the fields and potentials fall off to zero when approaching infinity.

In the presence of boundary surfaces, that is, plates, this integration cannot be performed as we would have to integrate “through” the boundary, where the integrand, that is, the (canonical) EMT, diverges. In these cases we choose which EMT we want to compute before we impose boundary conditions. However, when we compare different energy-momentum tensors and interpret the physical meaning of their components, we have to keep these subtleties in mind.

Another approach would be to replace the ideal boundaries with the interaction with an external, non-dynamical, and smooth potential, which models the ideal boundary conditions in a certain limit [49, 50]. Such a calculation was done in [5] for the Casimir energy and in [51–53] for energy densities. Modeling the boundary with the interaction with a potential leads to the renormalization of divergences that one usually encounters in quantum field theory. To that end, the authors used perturbation theory and calculated

4.1 Analytical calculation for two parallel plates

1-loop Feynman diagrams. The renormalized Casimir energy is then finite for smooth potentials. In the limit when the potential becomes sharply located, i.e., becomes a δ -function, and the coupling constant goes to infinity, the potential models perfect Dirichlet boundary conditions. It was, however, shown that this limit leads to divergences that cannot be absorbed with the help of renormalization. These divergences, which are located on the boundary, can be interpreted as the infinite energy necessary to constrain the field fluctuations on the boundary on all energy scales.

In a calculation with different energy-momentum tensors, the Casimir energy-momentum tensors should be finite everywhere for a smooth and finite potential after renormalization as well. Although, they can have different values locally, integrating the Casimir EMTs over the spacetime volume should yield the same total energy and momentum. This integration need not commute with the above mentioned Dirichlet limit: different energy-momentum tensors can have a different divergence structure in this limit. This would explain why, for perfect boundaries, the canonical EMT diverges on the boundaries while the conformal EMT does not.

We would like to have an expression of the conformal complement in the worldline formalism as well. Toward that end, we follow along the lines of the calculations performed for $T_{00}(\vec{x}, t)$ and $T_{zz}(\vec{x}, t)$ in Chapter 2. The resulting 00 and zz components of $\Delta\hat{T}_{\mu\nu}(\vec{x}, t)$ are

$$\begin{aligned}\Delta T_{00}(\vec{x}, t) &= -4\xi \int \frac{dk}{2\pi} \frac{k}{E_k} \vec{\nabla} \cdot (\vec{\nabla} + \vec{\nabla}') \operatorname{Im} G(\vec{x}, \vec{x}', k) \\ &= -4\xi \cdot T_{00}(\vec{x}, t)|_{II} \\ \Delta T_{zz}(\vec{x}, t) &= -2\xi \left((\partial_z + \partial_{z'})^2 - 2\vec{\nabla} \cdot (\vec{\nabla} + \vec{\nabla}') \right) \int \frac{dk}{2\pi} \frac{k}{E_k} \operatorname{Im} G(\vec{x}, \vec{x}', k) \\ &= -4\xi \left(T_{zz}(\vec{x}, t)|_{Ia} - T_{00}(\vec{x}, t)|_{II} \right).\end{aligned}$$

As a consequence, the conformal or improved energy-momentum tensor $\Theta_{\mu\nu}(\vec{x}, t) :=$

4 The energy-momentum tensor for Casimir's parallel plates

$T_{\mu\nu}(\vec{x}, t) + \Delta T_{\mu\nu}(\vec{x}, t)$ is then not only finite but even constant:

$$\begin{aligned}\Theta_{00}(\vec{x}, t)|^{d=2} &= -\frac{1}{32\pi a^3} 2\zeta(3), \\ \Theta_{zz}(\vec{x}, t)|^{d=2} &= -2\frac{1}{32\pi a^3} 2\zeta(3), \\ \Theta_{00}(\vec{x}, t)|^{d=3} &= -\frac{1}{32\pi^2 a^4} 2\zeta(4), \\ \Theta_{zz}(\vec{x}, t)|^{d=3} &= -3\frac{1}{32\pi^2 a^4} 2\zeta(4).\end{aligned}$$

Despite that, $\Theta_{\mu\nu}(\vec{x}, t)$ also violates the NEC

$$\Theta_{00}(\vec{x}, t) + \Theta_{zz}(\vec{x}, t) = \begin{cases} -\frac{6}{32\pi a^3} \zeta(3) & \text{for } d = 2 \\ -\frac{8}{32\pi^2 a^4} \zeta(4) & \text{for } d = 3 \end{cases}. \quad (4.8)$$

Our results for $\Theta_{\mu\nu}(\vec{x}, t)$ match those in [30] where the general case of a massive scalar field with DBCs in d spatial dimensions is presented. Since the conformal EMT $\Theta_{\mu\nu}(\vec{x}, t)$ can always be constructed from its canonical counterpart $T_{\mu\nu}(\vec{x}, t)$, we restrict our computations to the latter.

We note that for a discussion of the ANEC we choose boundary configurations that allow a complete geodesic (along the z axis) which does not intersect the boundary. Then it does not matter which EMT we choose. Since both tensors only differ in a total derivative, the respective values for the ANEC only differ in a boundary term at infinity. However, this term is zero because both tensors fall off to zero when approaching infinity along the z axis.

4.2 Worldline calculation for two parallel Dirichlet plates

The worldline calculation of the parallel plate configuration starts by finding the intersection condition from Fig. 4.1. This condition turns out to be very similar from the condition we encountered for one plate. There are nevertheless also some novel features. The worldlines have two possibilities to intersect the plates, which means we need to identify the two extremal points y_- and y_+ of each loop. More precisely, we need to determine which point intersects one of the plates first. For any given loop this will depend on the

4.2 Worldline calculation for two parallel Dirichlet plates

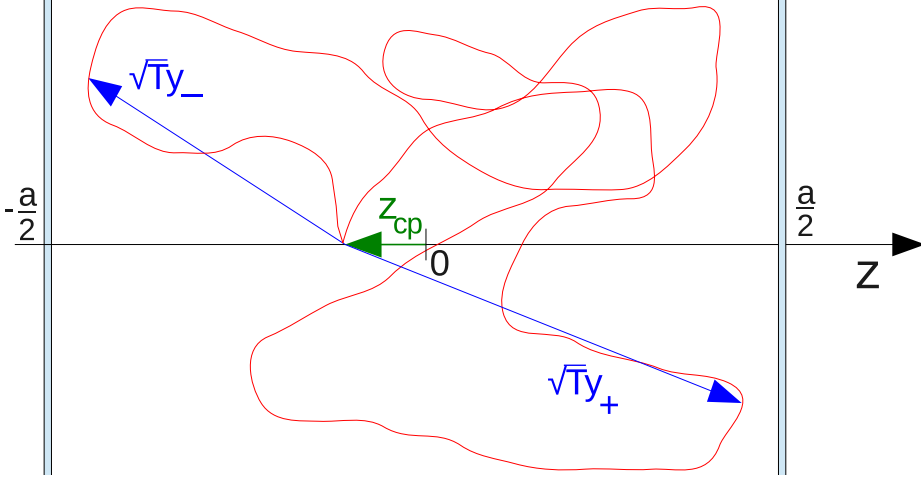


Figure 4.1 Sketch of the Casimir plates setup with an exemplary unit loop.

position z_{cp} on the z axis. The intersection conditions are explicitly

$$\left. \begin{aligned} \sqrt{T}y_- + z_{cp} &\leq -\frac{a}{2} \\ \sqrt{T}y_+ + z_{cp} &\geq \frac{a}{2} \end{aligned} \right\} \implies \Theta \left[\mathcal{F}(\vec{x}_{cp} + \sqrt{T}\vec{y}(t)) \right] = \Theta \left(\sqrt{T}\mathcal{M} - 1 \right) \quad (4.9)$$

$$\text{with } \mathcal{M} = \max[\mathcal{M}_+, \mathcal{M}_-] := \max \left[\frac{(y_+)}{\frac{a}{2} - z_{cp}}, \frac{(-y_-)}{\frac{a}{2} + z_{cp}} \right].$$

The condition in Eq. (4.9) is again 1-dimensional, so that 1-dimensional loops suffice for the computation. However, the calculation, especially of the derivatives of \mathcal{M} , is more involved because \mathcal{M} is the maximum function

$$\mathcal{M} = \frac{1}{2} (\mathcal{M}_+ + \mathcal{M}_- + |\mathcal{M}_+ - \mathcal{M}_-|). \quad (4.10)$$

Due to the modulus, \mathcal{M} is not twice differentiable at $\mathcal{M}_+ = \mathcal{M}_-$, in z_{cp} nor in δ_z . Despite that, we treat \mathcal{M} as if it were differentiable. This allows us to derive formal expressions for the various energy-momentum tensor components. In our numerical calculations these expressions will be given a concrete meaning.

We make use of Eq. (2.39a)-(2.39d) and simply substitute \mathcal{M} from Eq. (4.9). For $T_{00}(\vec{x}_{cp}, t)|_I$ the result is straightforward,

$$T_{00}(\vec{x}_{cp}, t)|_I = \frac{1}{(4\pi)^{\frac{d+1}{2}}} \frac{1}{d+1} \left\langle \max[\mathcal{M}_+, \mathcal{M}_-]^{d+1} \right\rangle.$$

4 The energy-momentum tensor for Casimir's parallel plates

Only the maximum function has to be evaluated in our algorithm for all points z_{cp} between the plates. Further manipulation of \mathcal{M} is not required.

The situation is different for the other three terms. $T_{00}(\vec{x}_{cp}, t)|_{II}$ and $T_{zz}(\vec{x}_{cp}, t)|_{Ia}$ are again identical due to the 1-dimensional condition of intersection. We will therefore not write down $T_{00}(\vec{x}_{cp}, t)|_{II}$ explicitly. It can be derived from $T_{zz}(\vec{x}_{cp}, t)|_{Ia}$ by replacing partial derivatives $\partial_{z_{cp}}$ with $\vec{\nabla}_{cp}$. The formal expression for $T_{zz}(\vec{x}_{cp}, t)|_{Ia}$ is

$$T_{zz}(\vec{x}_{cp}, t)|_{Ia} = -\frac{1}{2} \frac{1}{(4\pi)^{\frac{d+1}{2}}} \left\langle \mathcal{M}^{d-2} \left(\partial_{z_{cp}}^2 \mathcal{M} \right) + (d-2) \mathcal{M}^{d-3} \left(\partial_{z_{cp}} \mathcal{M} \right)^2 \right\rangle,$$

but we must shed light on the derivatives of \mathcal{M} . The first derivative is

$$\begin{aligned} \partial_{z_{cp}} \max[\mathcal{M}_+, \mathcal{M}_-] &= \frac{1}{2} \left[\frac{(y_+)}{\left(\frac{a}{2} - z_{cp}\right)^2} - \frac{(-y_-)}{\left(\frac{a}{2} + z_{cp}\right)^2} \right. \\ &\quad \left. + \operatorname{sgn}[\mathcal{M}_+ - \mathcal{M}_-] \left(\frac{(y_+)}{\left(\frac{a}{2} - z_{cp}\right)^2} + \frac{(-y_-)}{\left(\frac{a}{2} + z_{cp}\right)^2} \right) \right]. \end{aligned} \quad (4.11)$$

Despite the sgn function in Eq. (4.11), this term can be implemented and evaluated numerically without any problems. Possible discontinuities that occur for each single loop vanish in the continuum limit. However, the second derivative of \mathcal{M} poses a challenge because the sgn function is not differentiable. The formal result of the second derivative is

$$\begin{aligned} \partial_{z_{cp}}^2 \max[\mathcal{M}_+, \mathcal{M}_-] &= \frac{(y_+)}{\left(\frac{a}{2} - z_{cp}\right)^3} + \frac{(-y_-)}{\left(\frac{a}{2} + z_{cp}\right)^3} \\ &\quad + \operatorname{sgn}[\mathcal{M}_+ - \mathcal{M}_-] \left(\frac{(y_+)}{\left(\frac{a}{2} - z_{cp}\right)^3} - \frac{(-y_-)}{\left(\frac{a}{2} + z_{cp}\right)^3} \right) \\ &\quad + \frac{1}{2} \left(\frac{(y_+)}{\left(\frac{a}{2} - z_{cp}\right)^2} + \frac{(-y_-)}{\left(\frac{a}{2} + z_{cp}\right)^2} \right) \partial_{z_{cp}} \operatorname{sgn}[\mathcal{M}_+ - \mathcal{M}_-]. \end{aligned} \quad (4.12)$$

In Eq. (4.12) only the last term is problematic. Formally, one has $\partial_x \operatorname{sgn}(x) \propto \delta(x)$ whose numerical evaluation under the worldline average is not trivial. We in fact tried several versions of smeared-out δ -functions, but they all yielded unsatisfactory results with huge errors. That is why we instead use a brute force approach and approximate $\partial_x \operatorname{sgn}(x)$ with a difference quotient. There exist a couple of possibilities to do this. For example,

4.2 Worldline calculation for two parallel Dirichlet plates

one can consider $\text{sgn}[\mathcal{M}_+ - \mathcal{M}_-]$ as a function of the variable $\mathcal{M}_+ - \mathcal{M}_-$ or as a function of the two variables \mathcal{M}_+ and \mathcal{M}_- . The difference quotient of either option suffers from problems. In the first version $\mathcal{M}_+ - \mathcal{M}_-$ can go to zero and will generate diverging terms. The second version, while avoiding divergences and yielding better results, still carries a large systematic error. The third possibility for a difference quotient relies on the fact that both \mathcal{M}_+ and \mathcal{M}_- are positive. This allows us to write the sgn function as function of the ratio $\mathcal{M}_+/\mathcal{M}_-$. The resulting difference quotient can thus be written as

$$\begin{aligned}
 \partial_{z_{cp}} \text{sgn}[\mathcal{M}_+ - \mathcal{M}_-] &= \partial_{z_{cp}} \text{sgn}\left[\frac{\mathcal{M}_+}{\mathcal{M}_-} - 1\right] \\
 &= \partial_{\frac{\mathcal{M}_+}{\mathcal{M}_-}} \text{sgn}\left[\frac{\mathcal{M}_+}{\mathcal{M}_-} - 1\right] \partial_{z_{cp}} \frac{\mathcal{M}_+}{\mathcal{M}_-} \\
 &= \frac{\text{sgn}\left[\frac{\mathcal{M}_+}{\mathcal{M}_-}(1+l) - 1\right] - \text{sgn}\left[\frac{\mathcal{M}_+}{\mathcal{M}_-}(1-l) - 1\right]}{2l} \frac{\mathcal{M}_-}{\mathcal{M}_+} \Bigg|_{l \rightarrow 0} \partial_{z_{cp}} \frac{\mathcal{M}_+}{\mathcal{M}_-}.
 \end{aligned} \tag{4.13}$$

The parameter l in Eq. (4.13) must obey $l \ll 1$ but must not be so small as to render the numerator of the difference quotient equal to zero for too many loops in the ensemble. The systematic error that is introduced by this linearization of a derivative is controlled by l .

We note that if either \mathcal{M}_+ or \mathcal{M}_- should be zero then the ∂sgn term vanishes. However, this can only happen if either y_- or y_+ is equal to zero. Although such loops exist, their number decreases with increasing n_{ppl} . For instance, with $n_{ppl} = 2^{14}$ on average only 2 out of 10000 loops show this feature. Loops with $y_- = 0$ and $y_+ = 0$ at the same time cannot exist because the worldlines are Gaussian random numbers. (Such worldlines would have $y(t) = 0$ for all $t \in [0, 1]$.)

In the calculation of $T_{zz}(\vec{x}_{cp}, t)|_{I_b}$ the resulting expressions and difficulties are similar. We use \mathcal{M} from Eq. (4.10) in

$$T_{zz}(\vec{x}_{cp}, t)|_{I_b} = \frac{1}{2} \frac{1}{(4\pi)^{\frac{d+1}{2}}} \langle \mathcal{M}^d \mathcal{M}'' + d \mathcal{M}' \mathcal{M}' \mathcal{M}^{d-1} \rangle.$$

While different powers of \mathcal{M} are straightforward to evaluate, the derivatives with respect

4 The energy-momentum tensor for Casimir's parallel plates

to δ_z require some special consideration. The first and second derivative of \mathcal{M} are

$$\partial_{\delta_z} \max[\mathcal{M}_+, \mathcal{M}_-] = \frac{1}{2} \left[\frac{(y_+)'}{\frac{a}{2} - z_{cp}} + \frac{(-y_-)'}{\frac{a}{2} + z_{cp}} + \text{sgn}[\mathcal{M}_+ - \mathcal{M}_-] \left(\frac{(y_+)'}{\frac{a}{2} - z_{cp}} - \frac{(-y_-)'}{\frac{a}{2} + z_{cp}} \right) \right], \quad (4.14)$$

$$\begin{aligned} \partial_{\delta_z}^2 \max[\mathcal{M}_+, \mathcal{M}_-] &= \frac{1}{2} \left[\frac{(y_+)''}{\frac{a}{2} - z_{cp}} + \frac{(-y_-)''}{\frac{a}{2} + z_{cp}} + \text{sgn}[\mathcal{M}_+ - \mathcal{M}_-] \left(\frac{(y_+)''}{\frac{a}{2} - z_{cp}} - \frac{(-y_-)''}{\frac{a}{2} + z_{cp}} \right) \right] \\ &\quad + \frac{1}{2} \partial_{\delta_z} \text{sgn}[\mathcal{M}_+ - \mathcal{M}_-] \left(\frac{(y_+)'}{\frac{a}{2} - z_{cp}} - \frac{(-y_-)'}{\frac{a}{2} + z_{cp}} \right). \end{aligned} \quad (4.15)$$

All terms in Eq. (4.14) and (4.15) are familiar. The derivatives of $(\pm y_{\pm})$ are calculated as in the case of a single plate, that is,

$$\begin{aligned} (\pm y_{\pm})' &= \pm (1 - 2t_{\pm}) \Big|_{\delta_z=0}, \\ (\pm y_{\pm})'' &= \mp 2 \frac{t_{\pm}(\delta_z + h_{\delta}) - t_{\pm}(\delta_z - h_{\delta})}{2h_{\delta}} \Big|_{\delta_z=0, h_{\delta} \rightarrow 0}. \end{aligned}$$

The derivative of the sgn function is handled as in Eq. (4.13), that is, we calculate

$$\begin{aligned} \partial_{\delta_z} \text{sgn}[\mathcal{M}_+ - \mathcal{M}_-] &= \partial_{\frac{\mathcal{M}_+}{\mathcal{M}_-}} \text{sgn} \left[\frac{\mathcal{M}_+}{\mathcal{M}_-} - 1 \right] \partial_{\delta_z} \frac{\mathcal{M}_+}{\mathcal{M}_-} \\ &= \frac{\text{sgn} \left[\frac{\mathcal{M}_+}{\mathcal{M}_-} (1+l) - 1 \right] - \text{sgn} \left[\frac{\mathcal{M}_+}{\mathcal{M}_-} (1-l) - 1 \right]}{2l} \frac{\mathcal{M}_-}{\mathcal{M}_+} \Big|_{l \rightarrow 0} \partial_{\delta_z} \frac{\mathcal{M}_+}{\mathcal{M}_-}. \end{aligned} \quad (4.16)$$

The first term in Eq. (4.16) is the same as in Eq. (4.13) and we can compute it for $l \ll 1$. The second term reduces to terms containing $(\pm y_{\pm})'$ which we know how to calculate as well. Indeed, except for the calculation of the difference quotient in Eq. (4.16) and (4.13), the computation for two parallel plates resembles the one for a single plate.

4.3 Numerical results for $T_{00}(\vec{x}_{cp}, t)$ and $T_{zz}(\vec{x}_{cp}, t)$

Just like in the case of the single Dirichlet plate, we calculate preliminary results for the parallel plate configuration by running our algorithm with a worldline ensemble of 25 000

4.3 Numerical results for $T_{00}(\vec{x}_{cp}, t)$ and $T_{zz}(\vec{x}_{cp}, t)$

loops with 2^{14} points per loop. For the derivatives $l = 0.1$ and the optimal value of h_δ corresponding to Tab. 3.3 are used. Our numerical worldline data is shown next to the analytical results in Fig. 4.2. There is a very good agreement between both and the

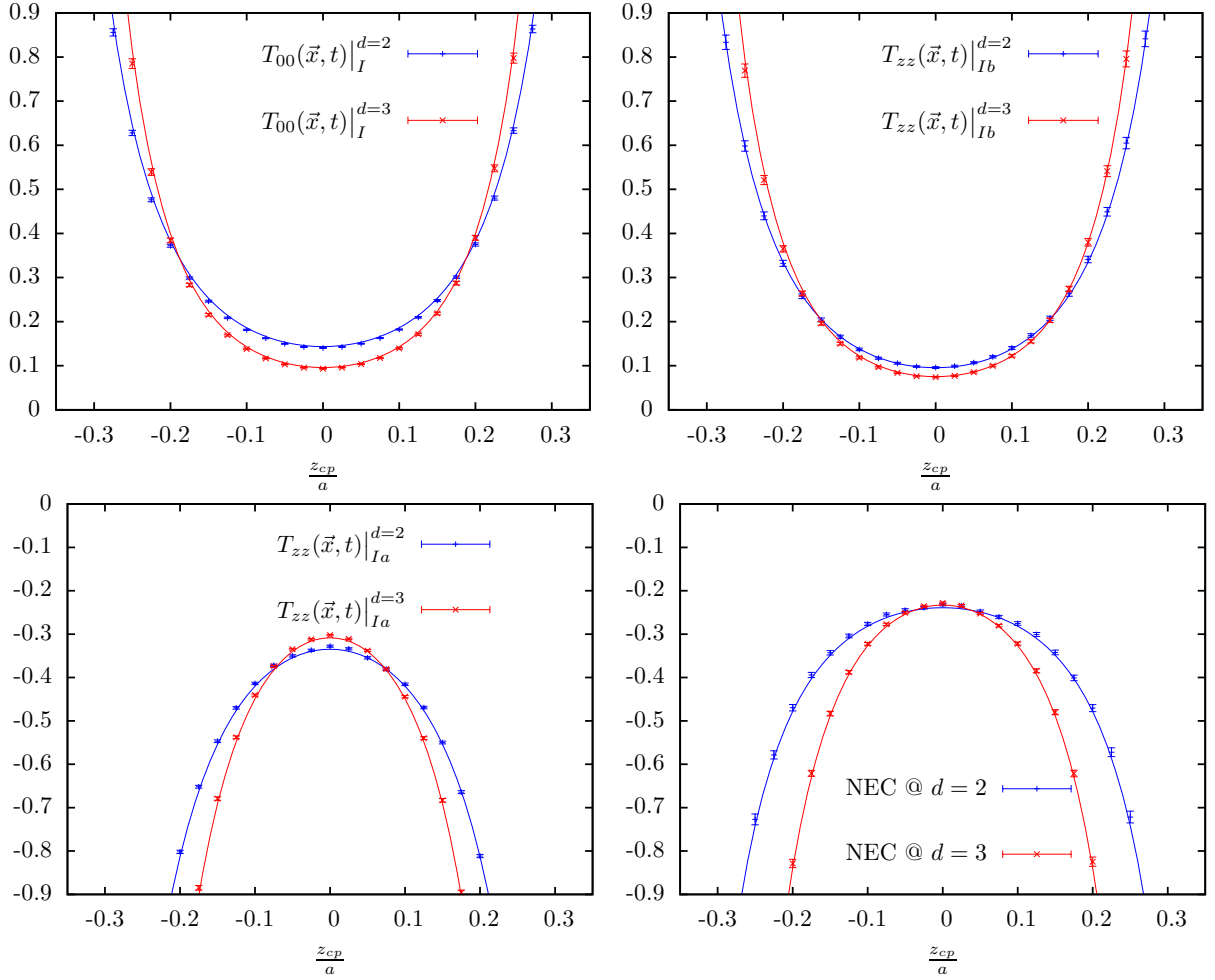


Figure 4.2 Comparison of analytical and numerical results for a worldline ensemble with $N = 25 \cdot 10^3$, $l = 0.1$, $n_{ppl} = 2^{14}$ and the corresponding optimal value of h_δ .

remaining overall error can be estimated to about 10%. While this is already convincing that our algorithm works, we analyze the errors in more detail to further improve our results.

4.3.1 Determination and reduction of errors

Most sources of errors are already known. The statistical error is related to the number N of loops in our ensemble and the number of points per loop n_{ppl} determines a systematic error of the Monte Carlo integration. Furthermore, h_δ controls the systematic error of the derivatives $(\pm y_\pm)'$ and $(\pm y_\pm)''$. Since the loop ensemble is spherically symmetric in the continuum limit, the values of $\langle(-y_-)\rangle$ and $\langle(y_+)\rangle$ are identical and so are their error estimates. Therefore, we can immediately use the optimized values of these three parameters that we found in our study of the single plate configuration.

There is only one new systematic error. It originates from the linearization of the derivative of the sgn function in $\partial^2\mathcal{M}$ and is determined by l . In order to estimate an optimal value of l , we compute the expectation value of $\partial_x \text{sgn}(x-1)$ with $x = \mathcal{M}_+/\mathcal{M}_-$. For that, we evaluate the difference quotient in Eq. (4.13) and (4.16) for different values of $l \ll 1.0$. In Fig. 4.3, we show the resulting function, which is positive with large values around $z_{cp} = 0$. The values of the function decrease to zero as we approach the plates at $z_{cp} = \pm a$. This is easily understood because $\partial_x \text{sgn}(x-1)$ with $x = \mathcal{M}_+/\mathcal{M}_-$ is only non-zero, if a worldline switches from intersecting one plate to intersecting the other plate first. This happens more often when the worldlines are in the middle than when they are close to one plate. One sees that for $l = 0.1$ and $l = 0.075$ the average of the derivative is approaching a smooth function with small statistical errors. For smaller l the errors increase and the fluctuations around the average value become large, as do the standard deviations. This is due to the fact that for too small l the numerator of the difference quotient tends to zero for too many loops in the average. $l = 0.075$ can thus be chosen as an optimal value. The remaining errors are reduced by an increase of n_{ppl} and N .

We ascertain the overall systematic errors by determining how the values of $T_{00}(\vec{x}_{cp}, t)$ and $T_{zz}(\vec{x}_{cp}, t)$ converge to their analytic values for increasing n_{ppl} . We choose three different values of z_{cp} at which we evaluate the EMT components for $N = 25 \cdot 10^3$, $n_{ppl} \in \{10, \dots, 20\}$ and the corresponding optimal value of h_δ and $l = 0.075$. The plots of these calculations can be found in the appendix in Fig. A.1 and A.2. We see that for more than 2^{14} points per loop the systematic errors and the fluctuations around the analytical value become small. An estimate for the systematic error for large n_{ppl} is calculated by fitting the worldline data to a function $a + b/n_{ppl}$. A compilation of the results is Tab. 4.1.

4.3 Numerical results for $T_{00}(\vec{x}_{cp}, t)$ and $T_{zz}(\vec{x}_{cp}, t)$

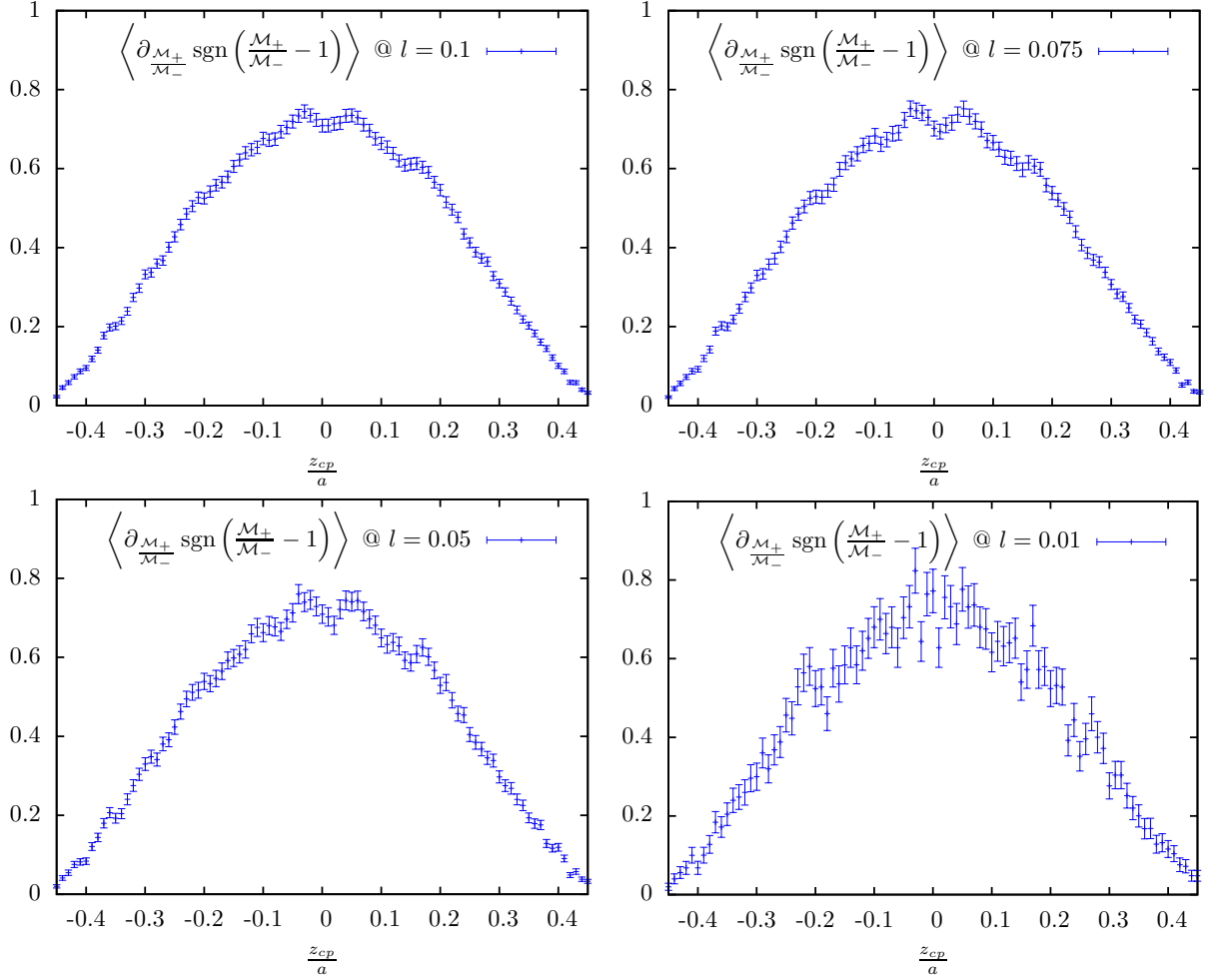


Figure 4.3 Worldline average of the derivative of the sign function for different values of the parameter l .

The systematic errors vary with z_{cp} and so we take the largest error, 2.5% as a general estimate.

4.3.2 Optimized numerical results

To arrive at results with minimal errors we increase the number of loops to $N = 5 \cdot 10^5$ and the number of points per loop to $n_{ppl} = 2^{20}$. This value corresponds $f = 12$ and $\varepsilon = 0.099$ according to Tab. 3.3. We also choose $l = 0.075$. Fig. 4.4 shows our optimized numerical data in comparison to the analytical result for both parts of $T_{zz}(\vec{x}_{cp}, t)$. The

4 The energy-momentum tensor for Casimir's parallel plates

$z_{cp} =$	0.15	0.0	-0.35	0.15	0.0	-0.35
$T_{00}(\vec{x}_{cp}, t) _I$	$d = 2$			$d = 3$		
Δ_{sys}	1.2 %	0.7 %	0.6 %	1.8 %	1.0 %	0.8 %
$T_{zz}(\vec{x}_{cp}, t) _{Ia}$	$d = 2$			$d = 3$		
Δ_{sys}	0.2 %	1.2 %	0.1 %	0.6 %	0.6 %	0.4 %
$T_{zz}(\vec{x}_{cp}, t) _{Ib}$	$d = 2$			$d = 3$		
Δ_{sys}	1.5 %	1.0 %	1.4 %	2.5 %	0.5 %	0.5 %

Table 4.1 Systematic errors Δ_{sys} for the original Casimir setup for $N = 25 \cdot 10^3$ and $n_{ppl} \rightarrow \infty$.

differences between both are only minimal with statistical errors of less than 1% and the aforementioned 2.5% systematic error. As a result the projection of the EMT on the z

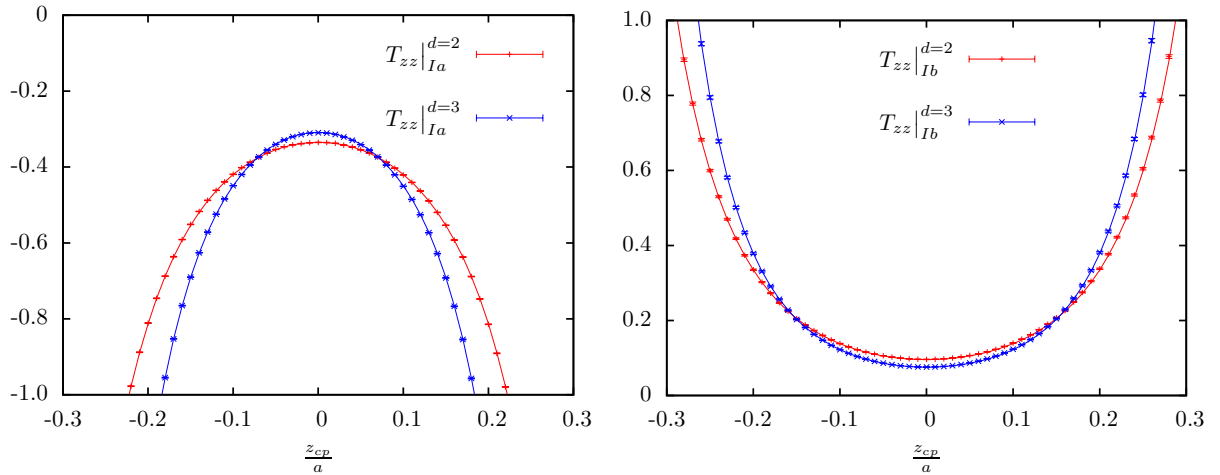


Figure 4.4 $T_{zz}(\vec{x}_{cp}, t)$ for the original Casimir configuration in $d = 2$ and $d = 3$ with minimized errors.

axis is reproduced by our data extremely well, too (cf. Fig. 4.5). It is negative between the plates and diverges near them. The statistical error of the worldline values is below 0.6% resulting in an overall error of our results of about 3%.

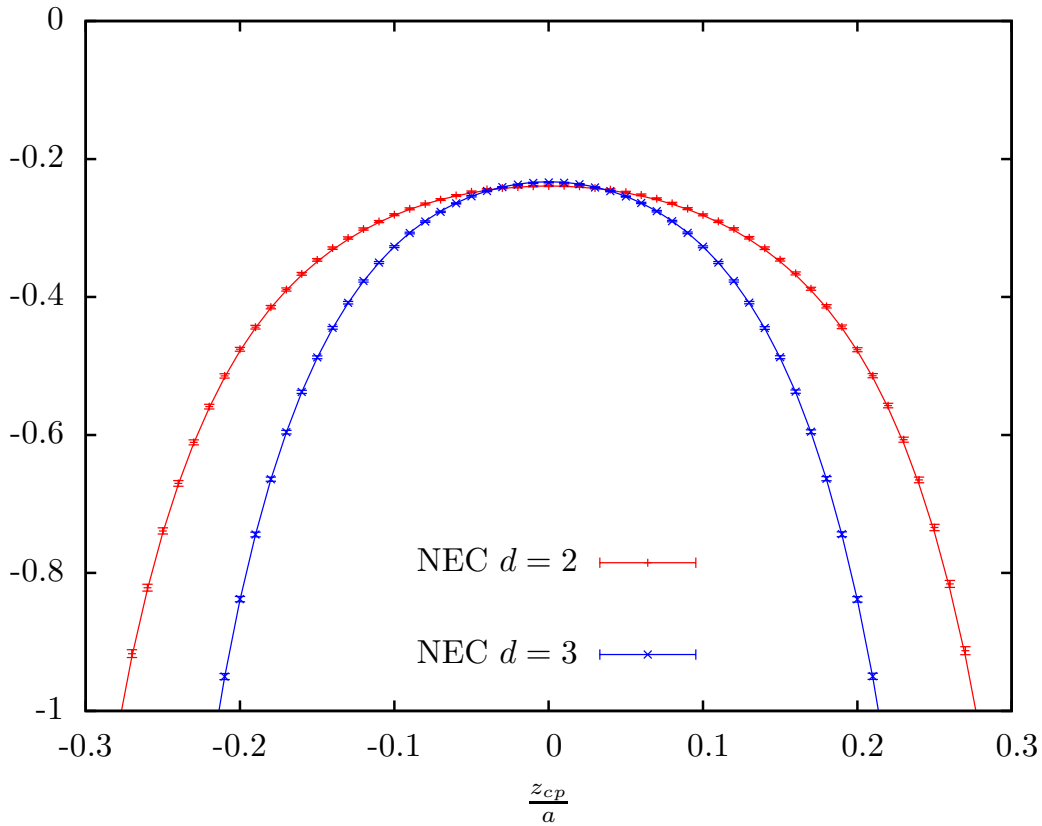


Figure 4.5 Projection of the EMT on the z axis, i.e., the null energy condition for two parallel Dirichlet plates in 2 and 3 spatial dimensions.

4.4 Conclusions

In this chapter we have seen how worldline numerics also passes the second proof-of-principle test, the two parallel Dirichlet plates configuration. The worldline calculation of the EMT for this setup of boundaries was shown to be very similar to the single plate configuration. The divergent behavior of the EMT when approaching either plate was calculated analytically and also numerically. The well-known violation of the NEC was reproduced as well. Furthermore, we showed how the conformal energy-momentum tensor can be constructed from the canonical EMT components. Our numerical algorithm proved to be highly efficient, reproducing the analytic values within about 3% at computation cost of no more than 1 CPU-day. The computation of $T_{zz}(\vec{x}_{cp}, t)$ includes the calculation of derivatives of the worldline parameters ($\pm y_{\pm}$) and a sgn function. Despite being non-

4 The energy-momentum tensor for Casimir's parallel plates

differentiable, numerical derivatives of both functions are shown to be achievable with relatively small errors.

5 Averaged Null Energy Condition for configurations with complete geodesics

In the previous chapters we demonstrated how composite operators, specifically the energy-momentum tensor of a massless scalar, can be computed using worldline numerics. We were able to reproduce analytically known results for EMT components with high precision at low cost. Our focus now shifts more towards the computation of energy conditions. The NEC is violated in both the single plate and parallel plates configuration. However, in either setup of boundaries the calculation of the averaged null energy condition for a null geodesic that is not parallel to the boundary is not possible. Such a null geodesic would intersect $\partial\mathcal{D}$ and one cannot evaluate the EMT on the boundary, i.e., the plates. In the case of DBCs the EMT diverges on the plate as the potential $\sigma(\vec{x})$ goes to infinite positive values. The ANEC is weaker than the NEC since it only requires that the integral of $\langle \hat{T}_{\mu\nu}(\vec{x}, t) V^\mu V^\nu \rangle$ along a complete null geodesic γ with tangent vectors V^μ is larger or equal to zero. The ANEC along the z axis is

$$0 \leq \int_{\gamma} d\lambda \langle \hat{T}_{\mu\nu}(\vec{x}, t) V^\mu V^\nu \rangle = \int_{-\infty}^{+\infty} dz (T_{00}(\vec{x}, t) + T_{zz}(\vec{x}, t)),$$

where γ is affinely parameterized by λ . We can therefore only integrate the NEC along the z axis if $\partial\mathcal{D}$ has holes through which the z axis passes. In this chapter we study three different, yet similar, configurations with the z axis as a complete geodesic.

5.1 Averaged Null Energy Condition for a plate with a hole in $d = 2$

The simplest boundary configuration which allows for complete geodesics that are not parallel to $\partial\mathcal{D}$ is a punctured version of the single plate. We investigate this configuration in $d = 2$ and $d = 3$. (Semi-)Analytical results for both setups were computed in [22] where a cancellation between odd and even modes for different BCs was used.

Starting with the 2-dimensional case, the first step in the worldline computation is finding the condition of intersection. To that end, we use Fig. 5.1, which shows a punctured plate in two spatial dimensions. The symmetry axis of the hole is the z axis and the loop is placed on it at a distance z_{cp} from the center of the hole. The z coordinates of the worldlines are denoted by $y_z(t)$ and the coordinates parallel to the boundary by $y_{||}(t)$. Then $y_\rho = \sqrt{y_{||}^2(t) + y_z^2(t)}$ is the distance from the starting point z_{cp} to the point of first intersection and $r = \sqrt{a^2 + z_{cp}^2}$ is the distance to the closest point of the boundary, the edge of the hole. The angles ϕ and θ between y_ρ and r and the z axis are defined by

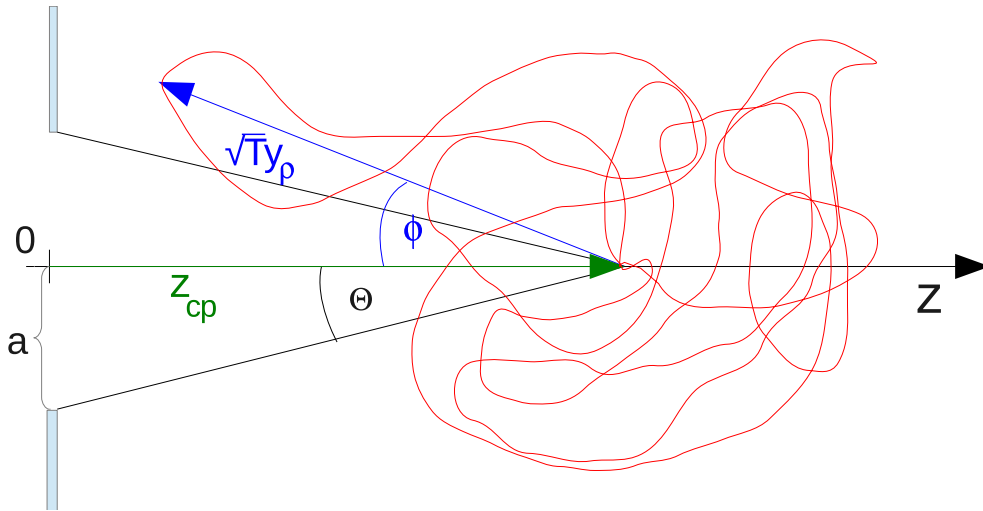


Figure 5.1 Sketch of a punctured plate in 2 spatial dimensions with an exemplary unit loop.

$\tan(\phi) = y_{||}(t)/y_z(t)$ and $\tan(\Theta) = a/z_{cp}$, respectively. The only points of the worldline that can intersect the plate are those for which $|\phi(t)| \geq |\theta|$. The intersection condition is

5.1 Averaged Null Energy Condition for a plate with a hole in $d = 2$

then

$$\left. \begin{aligned} \sqrt{T}y_z(t) + z_{cp} &\leq 0 \\ \left| \arctan\left(\frac{y_{||}(t)}{y_z(t)}\right) \right| &\geq \left| \arctan\left(\frac{a}{z_{cp}}\right) \right| \end{aligned} \right\} \implies \Theta \left[\mathcal{F}(\vec{x}_{cp} + \sqrt{T}\vec{y}(t)) \right] = \Theta \left(\sqrt{T}\mathcal{M} - 1 \right)$$

with $\mathcal{M} = \mathcal{M}_1 = \max \left(-\frac{y_z(t)}{z_{cp}} \right) \Big|_{|\phi(t)| \geq |\Theta|} = -\frac{\hat{y}_z}{z_{cp}}$

or $\mathcal{M} = \mathcal{M}_2 = \max \left(\frac{y_\varrho(t)}{r} \cdot \frac{\cos \phi(t)}{\cos \Theta} \right) \Big|_{|\phi(t)| \geq |\Theta|} = \frac{\hat{y}_\varrho}{r} G.$

(5.1)

\mathcal{M}_1 and \mathcal{M}_2 are two different parameterization of the same geometric intersection condition. Both are obviously 2-dimensional conditions because they are functions of $y_z(t)$ and $\phi(t)$. As a result, 2-dimensional worldlines must be computed.

Although \mathcal{M}_1 and \mathcal{M}_2 are identical for analytical calculations, they pose different problems for numerical evaluation. \mathcal{M}_1 is a ratio of two functions that tend to zero when $z_{cp} \rightarrow 0$. One can argue on physical grounds that the ratio must approach a finite value in this limit because the distance to $\partial\mathcal{D}$ is finite and the only divergent terms are located on $\partial\mathcal{D}$. However, we were not able to reproduce this finite value of the ratio in our numerical computations with reliable precision. In \mathcal{M}_2 this problem is not solved but shifted. $y_\varrho(t)$ and r are both positive. Their ratio can never diverge and is always positive or zero for $y_\varrho = 0$. The ratio of cosines G shows the same numerical problems as \mathcal{M}_1 . As z_{cp} goes to zero, $|\Theta|$ goes to $\pi/2$ and we know again on physical grounds that at the same time $|\phi(t)| \rightarrow \pi/2$. This happens, however, only in the continuum limit. With finite precision, the fluctuations in $\phi(t)$ are amplified by dividing with a small number $\cos \Theta$, which leads to large statistical errors.

In order to circumvent these difficulties, we explore an approximate, simplifying ansatz and set $\phi(t) = \Theta$, that is, $G = 1$. In this approximation the worldlines intersect the plate always at the edge of the hole first. The result is a simplified intersection condition

$$\mathcal{M}_3 = \max \left(\frac{y_\varrho(t)}{r} \right) \Big|_{|\phi(t)| = |\Theta|} = \frac{\hat{y}_\varrho}{r}. \quad (5.2)$$

All three intersection conditions determine a minimal value T_{min} for the proper-time integral. We neglect the case when worldlines cease to intersect $\partial\mathcal{D}$ at a finite value of

5 Averaged Null Energy Condition for configurations with complete geodesics

the proptime T_{max} . These loops do exist in the punctured plate configurations but the determination of T_{max} would increase the computation time considerably. Instead we consider neglecting these worldlines as a systematic error, which we will include in our error analysis.

In practice we generate 2-dimensional loops in Cartesian coordinates using the d loop algorithm. In a second step we introduce a binning in the angular coordinate ϕ and compute the maximal y_ρ for each bin. The angular binning translates into a binning of the z axis because $|\phi(t)| = |\Theta| = |\arccos(a/r)|$. The bins for small z_{cp} are consequently smaller than those for large z_{cp} . For the calculations presented in this thesis we used 120 angle bins, such that every bin is 3° . Similar calculations and binnings of worldlines were used in [36, 39, 40].

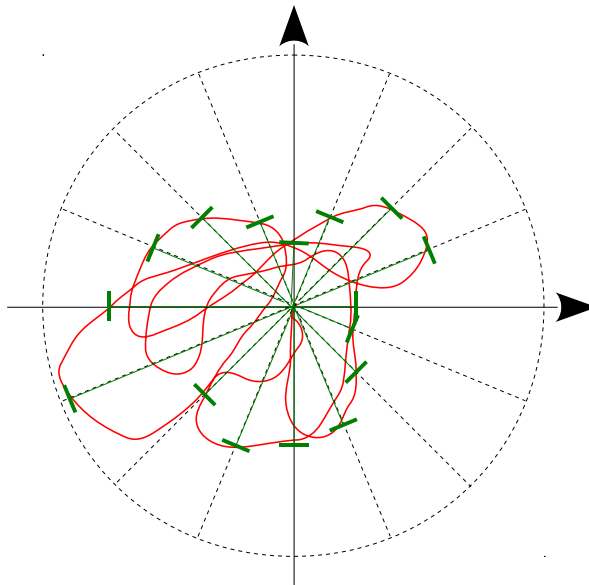


Figure 5.2 Sketch of the angular binning of a worldline (—). In each bin ϕ_q with $q \in \{1, \dots, \# \text{ of angle bins}\}$ the maximal value of y_ρ (—) is determined. The resulting map $y_\rho = y_\rho(\phi_q)$ describes an envelope of the worldline.

5.1.1 Numerical results for the simplified intersection condition

We compute the NEC and the ANEC first with the simplified condition Eq. (5.2). For the calculation of $T_{zz}(\vec{x}_{cp}, t)|_{I_a}$ and $T_{zz}(\vec{x}_{cp}, t)|_{I_b}$ the derivatives of \mathcal{M}_3 with respect to z_{cp} and δ_z are needed. The first and second z_{cp} derivatives of \mathcal{M}_3 are

$$\begin{aligned}\partial_{z_{cp}} \frac{\hat{y}_\varrho}{r} &= \frac{1}{r} (\partial_{z_{cp}} \hat{y}_\varrho) - \frac{z_{cp} \hat{y}_\varrho}{r^3} \\ \partial_{z_{cp}}^2 \frac{\hat{y}_\varrho}{r} &= \frac{1}{r} (\partial_{z_{cp}}^2 \hat{y}_\varrho) - 2 \frac{z_{cp}}{r^3} (\partial_{z_{cp}} \hat{y}_\varrho) + \frac{\hat{y}_\varrho}{r^3} \left(\frac{3 z_{cp}^2}{r^2} - 1 \right).\end{aligned}$$

The point \hat{y}_ϱ is a local maximum of $y_\varrho(t)$ with the constraint $\phi(t) = \Theta$. For the calculation of its derivatives we have to resort to difference quotients because we do not know the function $y_\varrho(t)$ explicitly. The systematic error connected with this linearization is controlled by h_z in $z_{cp} \pm h_z$. Normally, one would take h_z to be a small multiple of z_{cp} . However, this is not possible here because z_{cp} can go to zero. Instead the interval h_z is determined by considering z_{cp} as a function of Θ , that is, $z_{cp} \pm h_z$ corresponds to $\Theta \pm h_\Theta$. Θ remains finite throughout our calculations and it measures the distance z_{cp} via $\tan \Theta = a/z_{cp}$. We hence take $h_\Theta \approx 0.1\Theta$ and, using the shorthand notation $\pm l_z = \Theta \mp h_\Theta$, write the difference quotients as

$$\begin{aligned}\partial_{z_{cp}} \hat{y}_\varrho &= \frac{\hat{y}_\varrho|_{z_{cp}(l_z)} - \hat{y}_\varrho|_{z_{cp}(-l_z)}}{z_{cp}(l_z) - z_{cp}(-l_z)} \\ \partial_{z_{cp}}^2 \hat{y}_\varrho &= \frac{(\partial_{z_{cp}} \hat{y}_\varrho)|_{z_{cp}(l_z)} - (\partial_{z_{cp}} \hat{y}_\varrho)|_{z_{cp}(-l_z)}}{z_{cp}(l_z) - z_{cp}(-l_z)}.\end{aligned}$$

To be consistent for both sides of the plate, we use Θ when $\Theta > 0$ and $\Theta \leq \pi/2$ or the complementary angle when $\Theta > \pi/2$ for defining h_Θ .

$T_{zz}(\vec{x}_{cp}, t)|_{I_b}$ contains derivatives of \mathcal{M}_3 with respect to δ_z . As we mentioned above, we do not have sufficient information about the local maximum \hat{y}_ϱ to write down an analytic expression for the derivative. In its place we have to use difference quotients, for which we recast $T_{zz}(\vec{x}_{cp}, t)|_{I_b}$ as

$$T_{zz}(\vec{x}_{cp}, t)|_{I_b} = \frac{1}{2} \frac{1}{(4\pi)^{\frac{d+1}{2}}} \frac{1}{r^{d+1}} \langle \hat{y}_\varrho^d \hat{y}_\varrho'' + d \hat{y}_\varrho' \hat{y}_\varrho' \hat{y}_\varrho^{d-1} \rangle \quad (5.3)$$

$$= \frac{1}{2} \frac{1}{(4\pi)^{\frac{d+1}{2}}} \frac{1}{r^{d+1}} \frac{1}{d+1} \langle \partial_{\delta_z}^2 \hat{y}_\varrho^{d+1} \rangle. \quad (5.4)$$

5 Averaged Null Energy Condition for configurations with complete geodesics

The reason for this is that during our studies the derivatives in Eq. (5.3) turned out to fluctuate so much that the results were not usable. The difference quotient of \hat{y}_ρ^{d+1} in Eq. (5.4) is better behaved:

$$\partial_{\delta_z}^2 \hat{y}_\rho^{d+1} = \frac{\hat{y}_\rho^{d+1}|_{\delta_z+2h_\delta} + \hat{y}_\rho^{d+1}|_{\delta_z-2h_\delta} - 2\hat{y}_\rho^{d+1}|_{\delta_z}}{4h_\delta^2} \Big|_{\delta_z \rightarrow 0}.$$

Nevertheless, the fluctuations were still very large compared to those for the single plate or parallel plates configuration when using the values of h_δ from Sec. 3.3.1. As a result, we refined our estimates for h_δ , so that it is larger than the average distance between consecutive points but still small compared to the extension of the loop. $\langle e^2 \rangle = 1/6$ gives a rough measure of the extension of the loop. A more precise estimate for d -dimensional loops is $\sqrt{\langle e^2 \rangle} = \sqrt{d/6} > 1/6$ and, as a consequence, the optimal values of h_δ for the single plate configuration are to be considered lower bounds. With the new estimate of h_δ , we have for 2-dimensional loops

$$h_\delta \ll \sqrt{\langle e^2 \rangle} \implies h_\delta = \nu \sqrt{\frac{1}{3}} = \nu \cdot 0.58 \quad \text{with } \nu \ll 1.$$

We chose $\nu = 0.12$ for our calculations because we found this value to be small enough compared to 1 but not too small as to enhance the fluctuations in \hat{y}_ρ .

Despite the improved estimate for h_δ , the statistical fluctuations in $T_{zz}(\vec{x}_{cp}, t)|_{I_b}$, especially for small z_{cp} , proved to be huge in comparison to the single plate and parallel plates results. For instance, the standard deviations near $z_{cp} = 0$ were over 60% for an ensemble of $N = 10^4$ worldlines. We increased the number of loops to $N = 1.5 \cdot 10^6$ and the number of points per loop to $n_{ppl} = 2^{16}$ to get reliable data for $T_{zz}(\vec{x}_{cp}, t)|_{I_b}$ and reduce the systematic error at the same time. Fig. 5.3 shows our numerical data for $T_{zz}(\vec{x}_{cp}, t)|_{I_a}$ and $T_{zz}(\vec{x}_{cp}, t)|_{I_b}$ in $d = 2$. For both functions the errors become larger for $z_{cp} \rightarrow 0$. $T_{zz}(\vec{x}_{cp}, t)|_{I_b}$ crosses below the z axis to negative values near the center of the hole at $z_{cp} = 0$. We believe this to be part of the error of the simplifying approximation for the following reason. If the z extension were increased, that is, if the plate were made to be thicker then the region inside the hole would approach the configuration of two plates with the z axis parallel to them. $T_{zz}(\vec{x}_{cp}, t)|_{I_a}$ would go smoothly to zero if the plates were thick enough whereas $T_{zz}(\vec{x}_{cp}, t)|_{I_b}$ should have the same value inside the thick plates as it has now for the thin plates at $z_{cp} = 0$. However, we have not yet checked this conjecture.

5.1 Averaged Null Energy Condition for a plate with a hole in $d = 2$

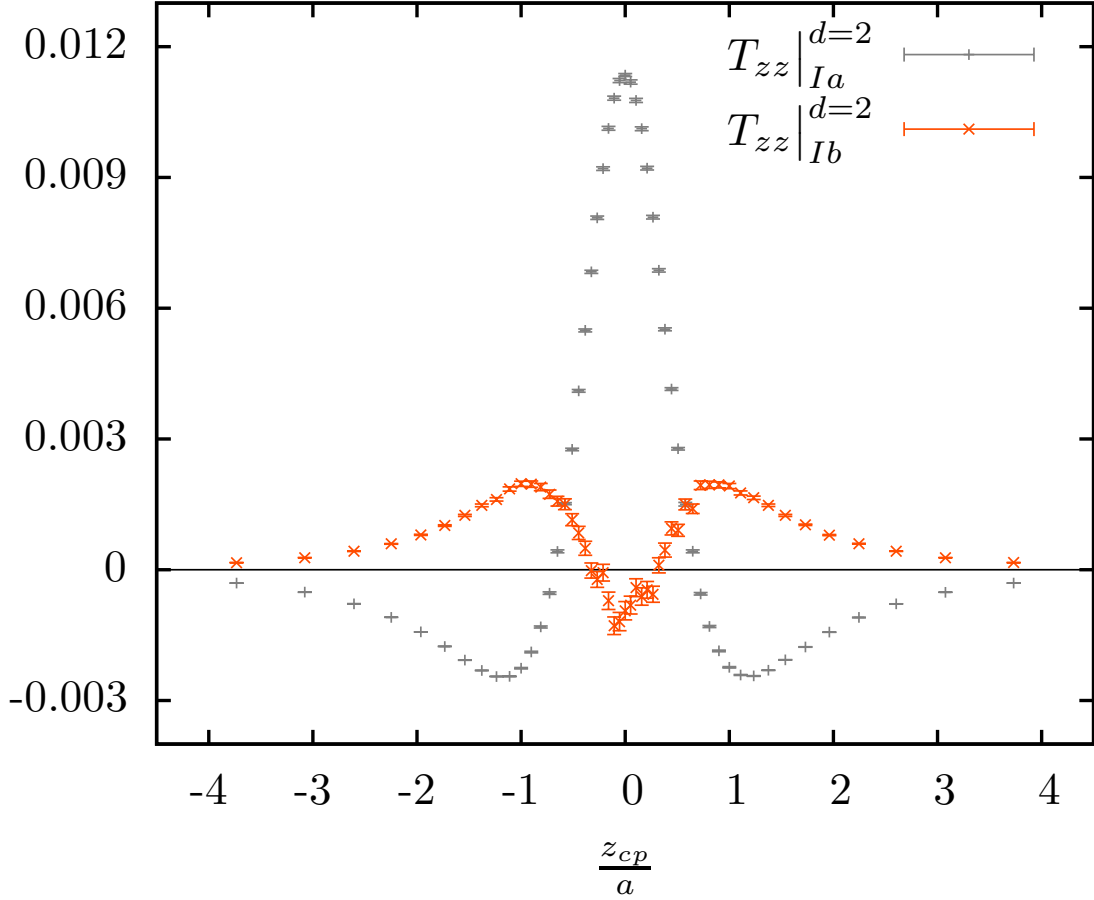


Figure 5.3 Numerical results of $T_{zz}(\vec{x}_{cp}, t)|_{I_a}$ and $T_{zz}(\vec{x}_{cp}, t)|_{I_b}$ for the 2-dimensional plate with a hole using the simplified condition of intersection

As we increased N to such a large number, the calculation takes a lot longer, which did not allow us to increase n_{ppl} above 2^{16} without increasing computation times beyond 3 CPU-days. The statistical errors are still about 2% and 20% at $z_{cp} = 0$ for $T_{zz}(\vec{x}_{cp}, t)|_{I_a}$ and $T_{zz}(\vec{x}_{cp}, t)|_{I_b}$, respectively. On top of that we have a systematic error which is very difficult to estimate since a calculation for different n_{ppl} and subsequent extrapolation is unfeasible for such large ensembles.

Besides the individual terms $T_{zz}(\vec{x}_{cp}, t)|_{I_a}$ and $T_{zz}(\vec{x}_{cp}, t)|_{I_b}$ we also computed the null energy condition, that is, the sum of both terms. Fortunately, summing both terms before the worldline average reduces the statistical error to about 2% at $z_{cp} = 0$. In Fig. 5.4 our numerical data is shown along with the analytical results obtained by Graham and Olum in [22]. The agreement between both data sets is already recognizable. However, the

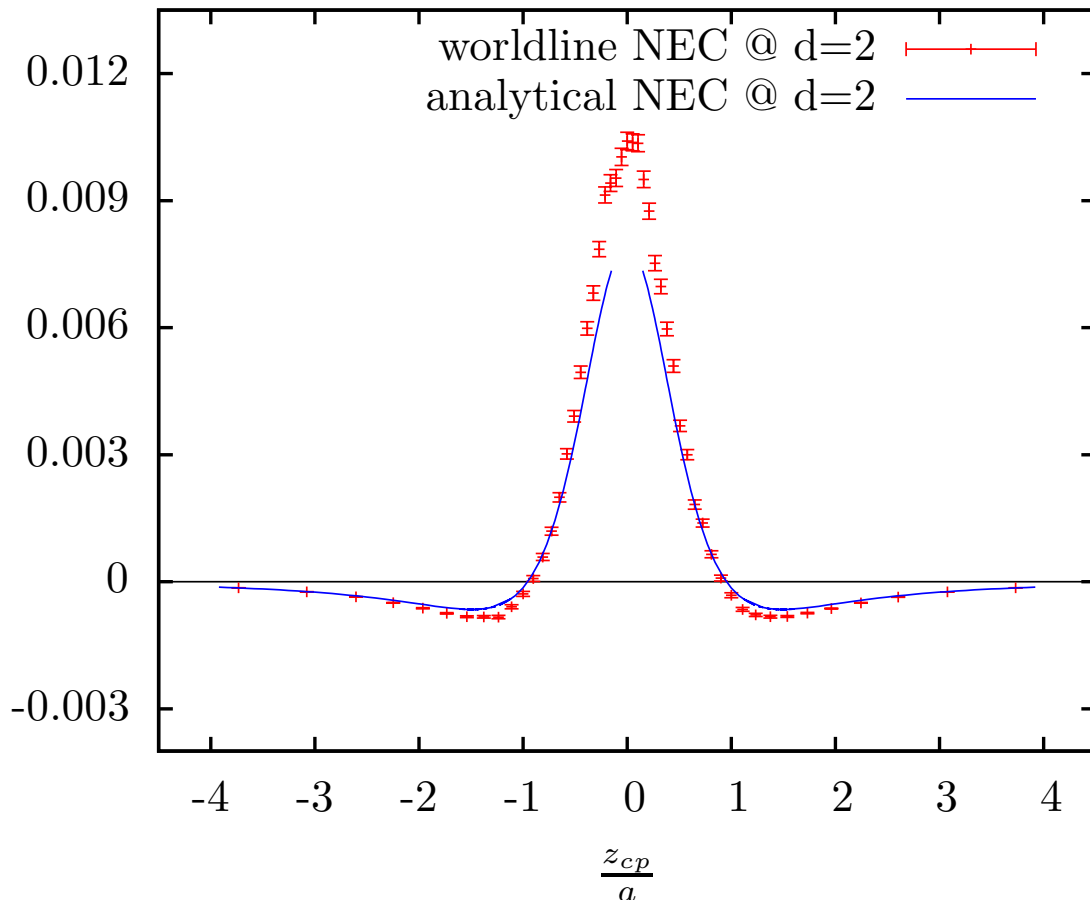


Figure 5.4 Null energy condition along the z axis for the punctured plate in $d = 2$ with the simplified condition of intersection.

numerical estimate of \hat{y}_q/r is too small compared to the analytical value. The worldline data stay below the analytical result for negative values and above for positive values because $T_{zz}(\vec{x}_{cp}, t)|_{I_a}$ is the negative second derivative of \mathcal{M}_3 . Still, it seems from Fig. 5.4 that the numerical value of the ANEC is larger than the analytical.

The ANEC is the integral of the NEC along the z axis. We approximate this integral by a sum of rectangles given by our numerical data for the NEC and our z_{cp} bins. For large distances $|z_{cp}|$ the punctured plate result approaches the NEC of the perfect mirror, i.e., the single plate

$$T_{00}(\vec{x}, t) + T_{zz}(\vec{x}, t) = -\frac{1}{32\pi} \frac{1}{z_{cp}^3}. \quad (5.5)$$

For values of z_{cp} outside the region shown in Fig. 5.4 we integrated Eq. (5.5) over the

5.1 Averaged Null Energy Condition for a plate with a hole in $d = 2$

corresponding values of z_{cp} . The ANEC is hence

$$\int_{-\infty}^{+\infty} dz_{cp} (T_{00}(\vec{x}, t) + T_{zz}(\vec{x}, t)) = (5.60 \pm 0.35) \cdot 10^{-3}/a^2, \quad (5.6)$$

which is slightly larger than the analytical value $4.53 \cdot 10^{-3}/a^2$ in [22]. However, the errors in Eq. (5.6) are only due to the statistical errors in our calculation. There are several sources of systematic errors like a finite n_{ppl} , the linearization of derivatives with difference quotients and first and foremost the approximation of the intersection condition. Despite all that, the simplified intersection condition \mathcal{M}_3 already gives a reasonable, though rough, first estimate of the true result.

Since we reduce the statistical error to acceptable values by using a very large value N , it is not easily feasible to compute the NEC for increasing n_{ppl} and determine the systematic error. We can, however, reduce the systematic error by using the exact intersection condition \mathcal{M}_2 . In order to do that, we have to find a parameterization of the factor G in Eq. (5.1) that yields small numerical errors.

5.1.2 Numerical calculation with condition \mathcal{M}_2

The intersection \mathcal{M}_2 accounts for the case that the worldlines do not intersect the plate exactly at the edge of the hole

$$\mathcal{M}_2 = \max \left(\frac{y_\rho(t)}{r} \cdot \frac{\cos \phi(t)}{\cos \Theta} \right) \Big|_{|\phi(t)| \geq |\Theta|} = \frac{\hat{y}_\rho}{r} G. \quad (5.7)$$

We can make use of trigonometric relations between r , $y_\rho(t)$, Θ and $\phi(t)$ in order to recast the geometric factor G in a form that is suitable for numerical evaluation,

$$G = \frac{\cos \phi(t)}{\cos \Theta} \quad (5.8)$$

$$= \left(\cos^2 \Theta + \left[\sin \Theta + \frac{\sin(\phi(t) - \Theta)}{\cos \phi(t)} \right]^2 \right)^{-\frac{1}{2}}. \quad (5.9)$$

In the limit $z_{cp} \rightarrow 0$ we know from physical considerations that $\phi(t) \rightarrow \Theta \rightarrow \pi/2$, but also that $G \rightarrow 1$. In this limit fluctuations in $\phi(t)$ give rise to large values of G and consequently to large statistical errors in Eq. (5.8). On the other hand, in Eq. (5.9) a

5 Averaged Null Energy Condition for configurations with complete geodesics

similar term, $\sin(\phi(t) - \Theta)/\cos \phi(t)$, is isolated in the denominator. Large fluctuations in this term do not cause large statistical errors for G .

In order to estimate the magnitude of the influence of G on the numerical results, we compare in Fig. 5.5 the values of $T_{00}(\vec{x}_{cp}, t)|_I$ for the exact G according to Eq. (5.9) and $G = 1$. $T_{00}(\vec{x}_{cp}, t)|_I$ has the advantage that it contains no derivatives and so systematic errors are only due to a finite n_{ppl} . These errors are, however, identical for both versions of intersection conditions, since we use the exact same worldline ensemble for both calculations. Fig. 5.5 shows that using the exact G results in larger values of $T_{00}(\vec{x}_{cp}, t)|_I$. This

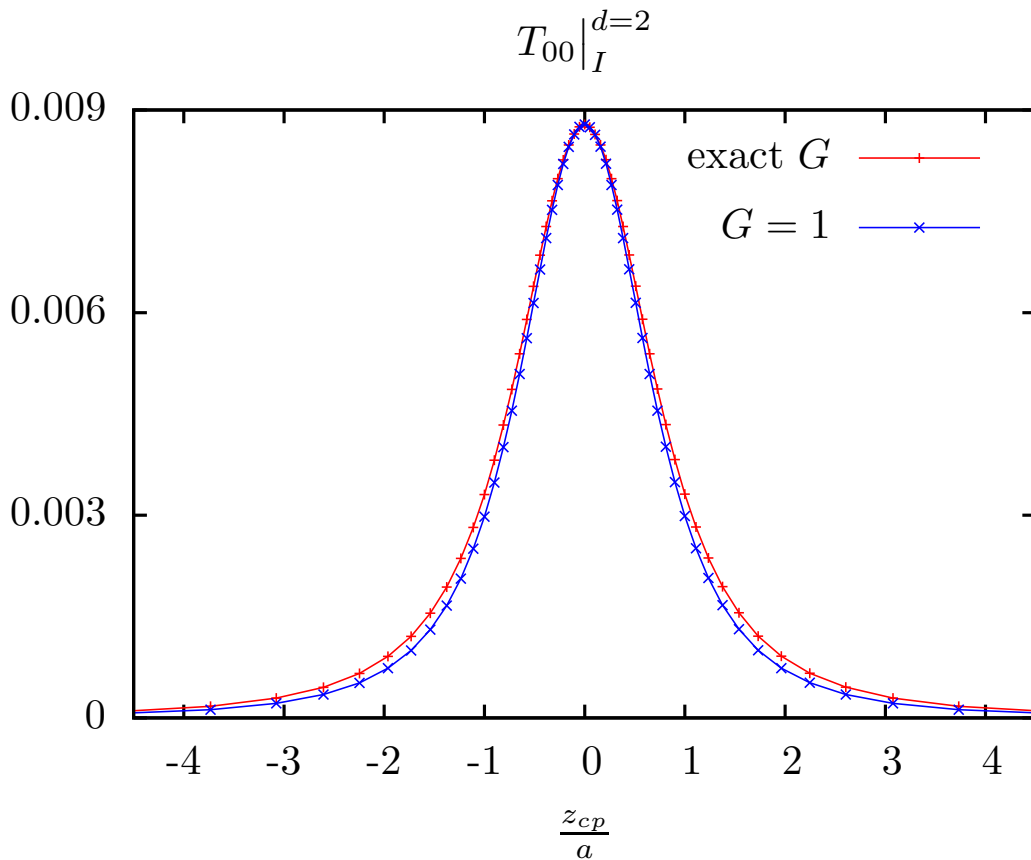


Figure 5.5 Comparison of $T_{00}(\vec{x}_{cp}, t)|_I$ for the 2-dimensional plate with a hole using the intersection conditions \mathcal{M}_2 and \mathcal{M}_3 . Both data sets were computed from the same worldline ensemble of $N = 1.5 \cdot 10^6$ worldlines with 2^{16} points per loop.

difference becomes larger with increasing distance from the hole and amounts to about 10% at $z_{cp} = 1.0$ and 20% at $z_{cp} \approx 2.0$.

5.1 Averaged Null Energy Condition for a plate with a hole in $d = 2$

The computation of the components of $T_{zz}(\vec{x}_{cp}, t)$ proceeds as above and we only replace \hat{y}_ρ with $\hat{y}_\rho G$ in all terms. The considerations for h_z and δ_z , respectively, are not changed by this replacement. The plot in Fig. 5.6 shows that the worldline data match better with the analytical values. The numerical result is still somewhat larger than the analytical for small z_{cp} .

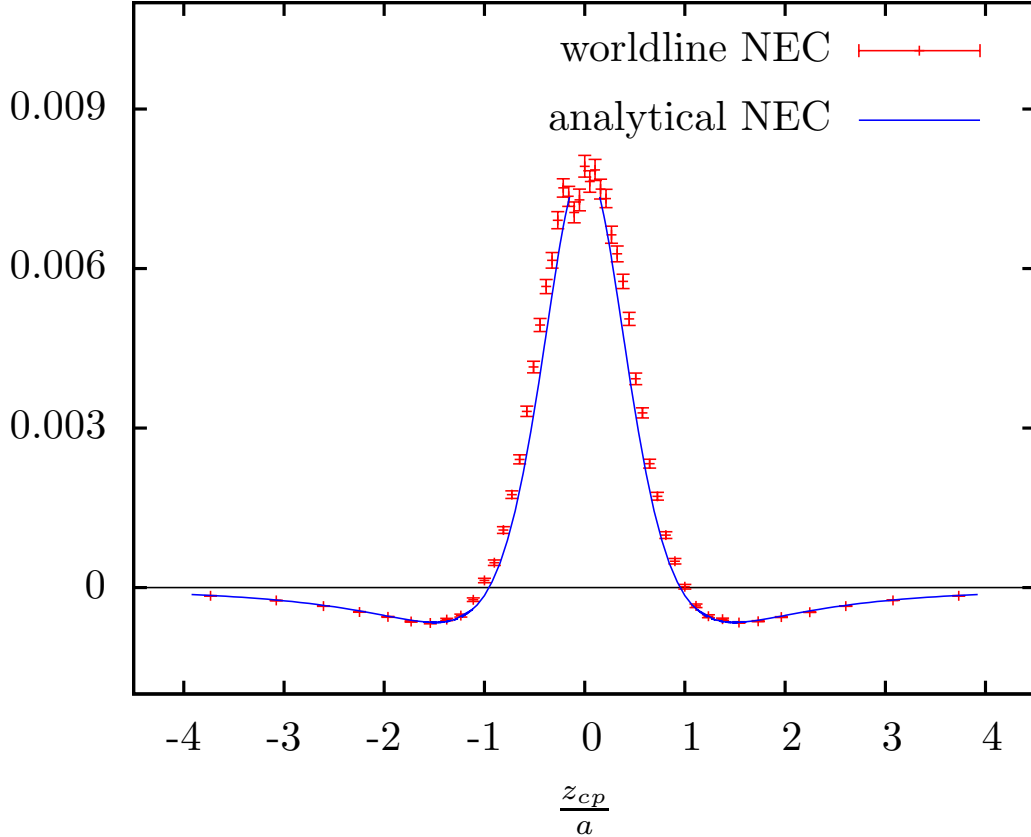


Figure 5.6 Null energy condition along the z axis for the punctured plate in $d = 2$ with the precise condition of intersection using an ensemble with $N = 1.5 \cdot 10^6$ and $n_{ppl} = 2^{16}$.

The integration of the NEC yields

$$\int_{-\infty}^{+\infty} dz_{cp} (T_{00}(\vec{x}, t) + T_{zz}(\vec{x}, t)) = (5.04 \pm 0.29) \cdot 10^{-3}/a^2, \quad (5.10)$$

a value that is still about 1.8 standard deviations larger than the analytical result. However, Eq. (5.10) only shows statistical, not systematic, errors. The overall systematic error is estimated by computing the difference between the analytical and numerical data at

5 Averaged Null Energy Condition for configurations with complete geodesics

the point closest to $z_{cp} = 0$ for which we have analytical data. Using the central values of our numerical result we find an error of 2% for the NEC. Since we integrate over both sides of the plate for the ANEC this amounts to an additional error of 4%. The statistical error in Eq. (5.10) corresponds to about 6%. The overall error Δ_{comp} of the numerical result of the ANEC is consequently of the order of 10% or

$$\int_{-\infty}^{+\infty} dz_{cp} (T_{00}(\vec{x}, t) + T_{zz}(\vec{x}, t)) = \begin{cases} (5.04 \pm 0.50) \cdot 10^{-3}/a^2 & \text{worldline} \\ 4.53 \cdot 10^{-3}/a^2 & \text{analytical [22]} \end{cases} .$$

This means that worldline numerics can replicate the analytical result of the ANEC for a plate with a hole in 2 space dimensions within the margin of error.

We note that we estimated the systematic error in a rather crude manner. An in-depth analysis will most likely increase the error bounds because our data points over-estimate the analytical values throughout the region $-1 \leq z_{cp}/a \leq 1$. We forgo such a detailed investigation here and instead take a closer look at the sources of the errors because they will appear in later calculations as well.

The errors from discretizing the path integral occur for all worldline numerics calculations. The statistical error can be reduced by increasing the number N of loops and one systematic error can be decreased by using a larger number n_{ppl} of points per loop. We showed how to control these errors in the previous chapters. The linearizations of derivatives leads to additional systematic errors. These are controlled by the parameters h_z and h_δ and we estimated reasonable values for them. Despite that, an analysis of those systematic errors for large n_{ppl} would require extensive computing time.

The binning of the angular coordinate ϕ leads to another systematic error. The angular binning leads to a binning of z_{cp} values and thus had to be incorporated in the determination of h_z . Furthermore, the ϕ bins illustrate the systematic error due to finite n_{ppl} . We used 120 bins in our calculations, which means that there are less than 1% of all points per loop in each bin. At $z_{cp} = 0$ there are exactly two bins that contribute to the expectation value, one above and one below the z axis. As a result, only about 2% of all points of every loop determine the values of the various EMT components inside the hole. The further we move away from the punctured plate, the more angular bins can contribute to the worldline average. This systematic error is not very problematic for $T_{00}(\vec{x}_{cp}, t)|_I$ or $T_{zz}(\vec{x}_{cp}, t)|_{Ia}$. For the former, we only compute $\hat{y}_\rho G$ in each bin and

5.2 Averaged Null Energy Condition for a plate with a hole in $d = 3$

for the latter we compute differences of these values between different bins. However, for $T_{zz}(\vec{x}_{cp}, t)|_{Ib}$ differences of values of $\hat{y}_\rho G$ for different values of δ_z within one or between different bins are computed.

We can now try to understand why we needed a very large N to reduce the fluctuations in $T_{zz}(\vec{x}_{cp}, t)|_{Ib}$ to an acceptable level. The derivatives with respect to δ_z correspond to variations parallel to the z axis. These variations change the z coordinate of the points along the worldlines but not $y_{||}$. Hence, for angles $|\phi|$ near zero or π , the δ_z variations shift the worldline points only in z direction within one bin and the observable $\hat{y}_\rho G$ changes along that direction. In contrast, for $|\phi| \approx \pi/2$, the variations in δ_z can shift the loop points to other bins while we measure $\hat{y}_\rho G$ along the direction of the bin which is now orthogonal to the direction of variation. This leads to large fluctuations in the worldline average, as we observed.

The assumption that all loops intersect the boundary for all $T \geq T_{min}$ results also in a systematic error.

5.2 Averaged Null Energy Condition for a plate with a hole in $d = 3$

The second boundary configuration that we investigate is a plate with a hole in 3 spatial dimensions. It is constructed by rotating the punctured plate in 2 dimensions around the z axis. We show this setup in Fig. 5.7. There are now two coordinates parallel to $\partial\mathcal{D}$ that are denoted by y_x and y_y . The whole configuration is axisymmetrical with respect to the z axis and thus $y_{||}(t) = \sqrt{y_x^2(t) + y_y^2(t)}$ measures the orthogonal distance from this symmetry axis. As a consequence, y_ρ , r , ϕ and Θ are defined the same way as in the 2-dimensional case.

The worldlines only intersect the punctured plate with points for which $|\phi(t)| \geq |\Theta|$.

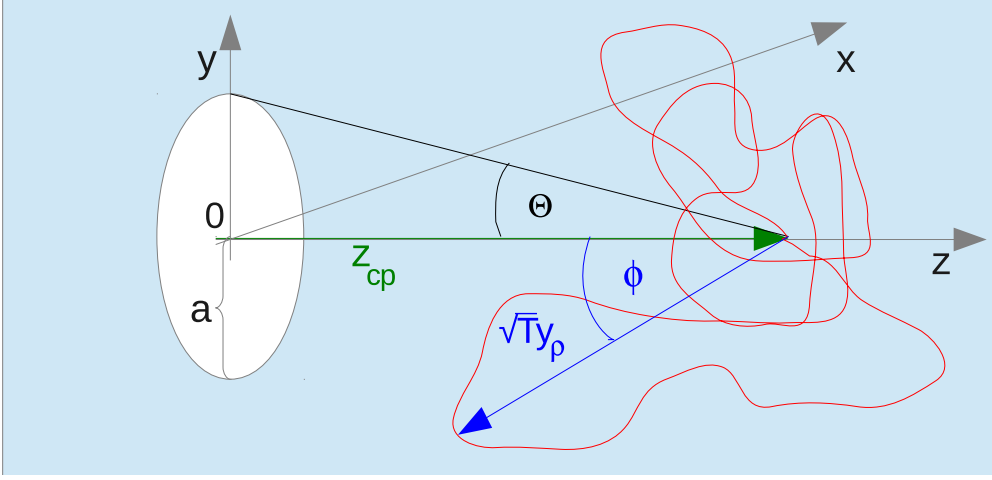


Figure 5.7 Sketch of the punctured plate in $d = 3$ with an exemplary unit loop.

The intersection conditions are hence identical to the 2-dimensional conditions

$$\begin{aligned}\mathcal{M}_1 &= \max \left(-\frac{y_z(t)}{z_{cp}} \right) \Big|_{|\phi(t)| \geq |\Theta|} = -\frac{\hat{y}_z}{z_{cp}}, \\ \mathcal{M}_2 &= \max \left(\frac{y_\varrho(t)}{r} \cdot \frac{\cos \phi(t)}{\cos \Theta} \right) \Big|_{|\phi(t)| \geq |\Theta|} = \frac{\hat{y}_\varrho}{r} G, \\ \mathcal{M}_3 &= \max \left(\frac{y_\varrho(t)}{r} \cdot \frac{\cos \phi(t)}{\cos \Theta} \right) \Big|_{|\phi(t)| = |\Theta|} = \frac{\hat{y}_\varrho}{r},\end{aligned}$$

where \mathcal{M}_1 and \mathcal{M}_2 are exact while \mathcal{M}_3 is a simplifying approximation. Even though \mathcal{M}_1 , \mathcal{M}_2 and \mathcal{M}_3 are effectively 2-dimensional conditions, $y_{||}$ already depends on y_x and y_y so that the calculations must be performed with worldlines in three dimensions. We will not consider \mathcal{M}_1 because of the same numerical challenges we faced in the case of the punctured plate in $d = 2$. We start our investigation by a calculation with the simplified condition of intersection \mathcal{M}_3 .

5.2.1 Numerical results for the simplified intersection condition

We already know how to compute the derivatives of \mathcal{M}_3 . The z_{cp} derivative must be expressed with a difference quotient with the parameters h_z and h_Θ . For the δ_z derivative a new value for h_δ is required because we have 3-dimensional loops now. From the

5.2 Averaged Null Energy Condition for a plate with a hole in $d = 3$

condition that h_δ be much smaller than the extension of a loop one finds

$$h_\delta \ll \sqrt{\langle e^2 \rangle} \implies h_\delta = \nu \sqrt{\frac{1}{2}} = \nu \cdot 0.71 \quad \text{with } \nu \ll 1.$$

We choose again $\nu = 0.12$ and run our algorithm with an ensemble of $1.5 \cdot 10^6$ worldlines and 2^{16} points per loop. Fig. 5.8 shows the resultant values of the individual parts of

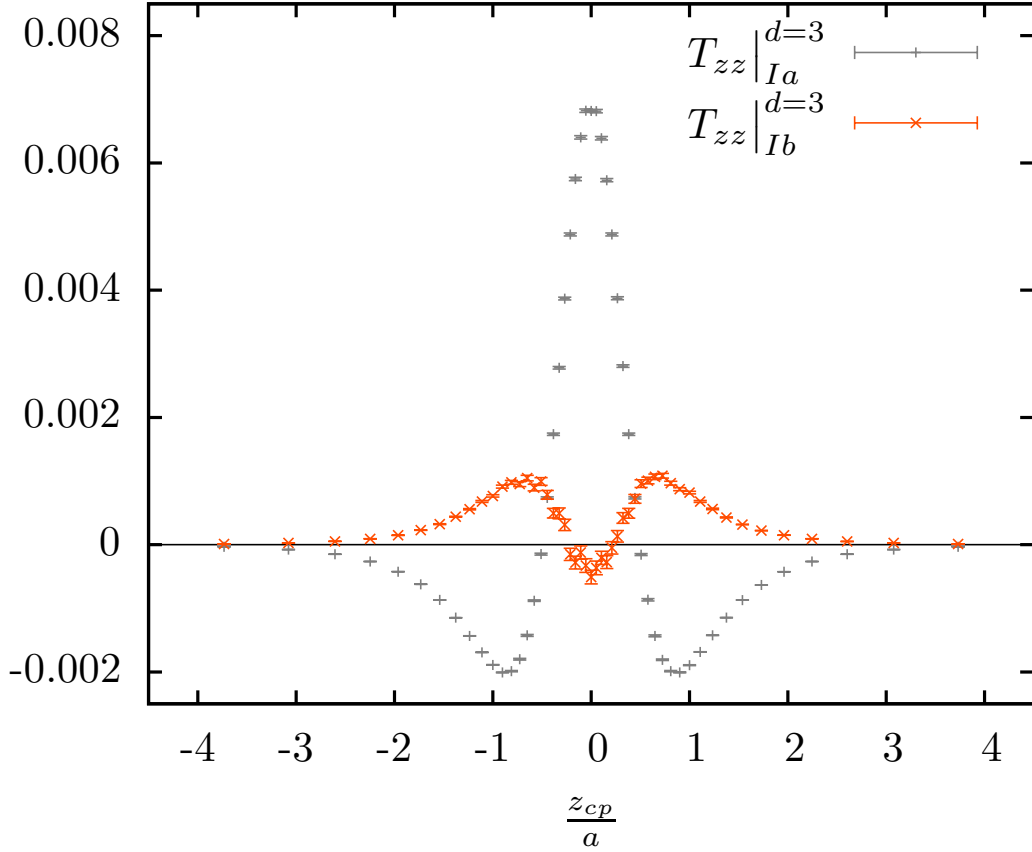


Figure 5.8 Numerical results of $T_{zz}(\vec{x}_{cp}, t)|_{Ia}$ and $T_{zz}(\vec{x}_{cp}, t)|_{Ib}$ for the plate with a hole in $d = 3$ using the simplified condition of intersection

$T_{zz}(\vec{x}_{cp}, t)$. The remaining statistical errors are still up to 20% at $z_{cp} = 0$ despite the improved estimate of h_δ and the large value of N . We also observe that $T_{zz}(\vec{x}_{cp}, t)|_{Ib}$ is negative near $z_{cp} = 0$. Whether this is a true value or results from finite numerical precision could not be decided yet and will be part of a more detailed study.

The NEC along the z axis is shown in Fig. 5.9. Our numerical value for \hat{y}_ρ is again smaller than the analytical. For negative values our data points stay below and for

5 Averaged Null Energy Condition for configurations with complete geodesics

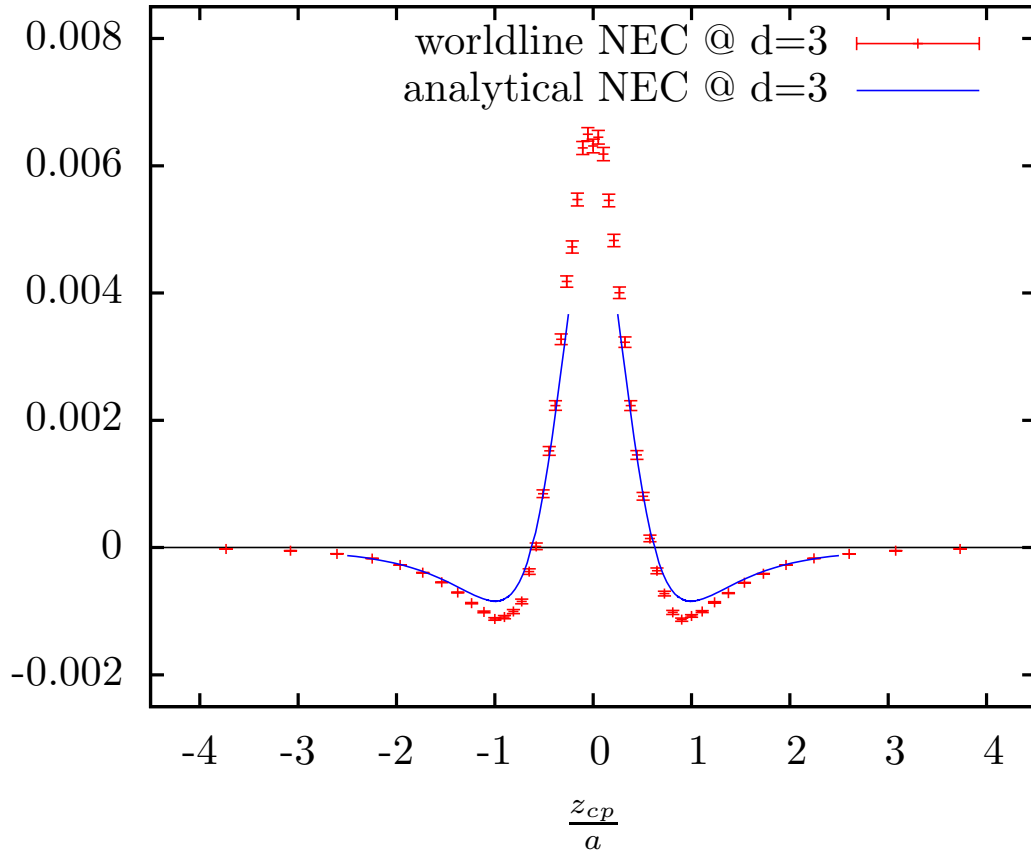


Figure 5.9 Null energy condition along the z axis for the punctured plate in $d = 3$ with the simplified condition of intersection.

positive values they stay above the analytical result. However, the standard deviation at the center of the hole is only 2%. We conjecture that the numerical ANEC is larger than the analytical. In order to check this conjecture, we integrate the NEC along the complete z axis. For values of z_{cp} outside the region of numerical data, we integrate the single plate result

$$T_{00}(\vec{x}, t) + T_{zz}(\vec{x}, t) = -\frac{1}{16\pi^2} \frac{1}{z_{cp}^4}. \quad (5.11)$$

The averaged null energy condition for the punctured plate in 3 spatial dimensions is then

$$\int_{-\infty}^{+\infty} dz_{cp} (T_{00}(\vec{x}, t) + T_{zz}(\vec{x}, t)) = (1.85 \pm 0.14) \cdot 10^{-3}/a^3, \quad (5.12)$$

5.2 Averaged Null Energy Condition for a plate with a hole in $d = 3$

which is as expected slightly larger than the analytical value of $1.63 \cdot 10^{-3}/a^3$ from [22]. Considering that we have not included systematic errors and that \mathcal{M}_3 is a simplified intersection condition, Eq. (5.12) is a very reasonable estimate of the analytical ANEC.

5.2.2 Numerical results with the condition \mathcal{M}_2

The condition \mathcal{M}_3 is based on the assumption that the worldlines only intersect the plate at the edge of the hole. The precise condition of intersection \mathcal{M}_2 in Eq. (5.1) together with the parameterization of G in Eq. (5.4) accounts for the fact that the loops can intersect at arbitrary points on the plate. We compute $T_{00}(\vec{x}_{cp}, t)|_I$ for both conditions to assess the difference between them. In Fig. 5.10 we plot both results, which look qualitatively like those obtained for the punctured plate in $d = 2$. Using the exact value of G , that is, using condition \mathcal{M}_2 , leads to larger values for $T_{00}(\vec{x}_{cp}, t)$. The difference increases with larger z_{cp} and is about 10 % at $z_{cp} \approx 1$ and 30 % at $z_{cp} \approx 2$.

The individual parts of $T_{zz}(\vec{x}_{cp}, t)$ and the NEC are computed for \mathcal{M}_2 by replacing \hat{y}_ρ with $\hat{y}_\rho G$. We find a better agreement between numerical and analytical data, even though the numerics still yields larger results (cf. Fig. 5.11). We furthermore observe relatively large statistical errors especially for small values of z_{cp} . These stem from fluctuations of the factor G because they were not present for the simplified case $G = 1$.

The result of the ANEC, the integration of the single plate result Eq. (5.11) for z_{cp} values outside the plot in Fig. 5.11 included, is

$$\int_{-\infty}^{+\infty} dz_{cp} (T_{00}(\vec{x}, t) + T_{zz}(\vec{x}, t)) = (1.76 \pm 0.12) \cdot 10^{-3}/a^3. \quad (5.13)$$

This value is about 1 standard deviation larger than the analytical value. The statistical error in Eq. (5.13) corresponds to about 7%. We would like to include the systematic errors as well. For that, we calculate the difference between numerical and analytical results for the smallest value of z_{cp} for which we have data of both. Disregarding the statistical errors and using only the central value of our worldline data, this error is about 1.2 % for the NEC, that is, at least about 2.4 % for the ANEC. Including both errors we

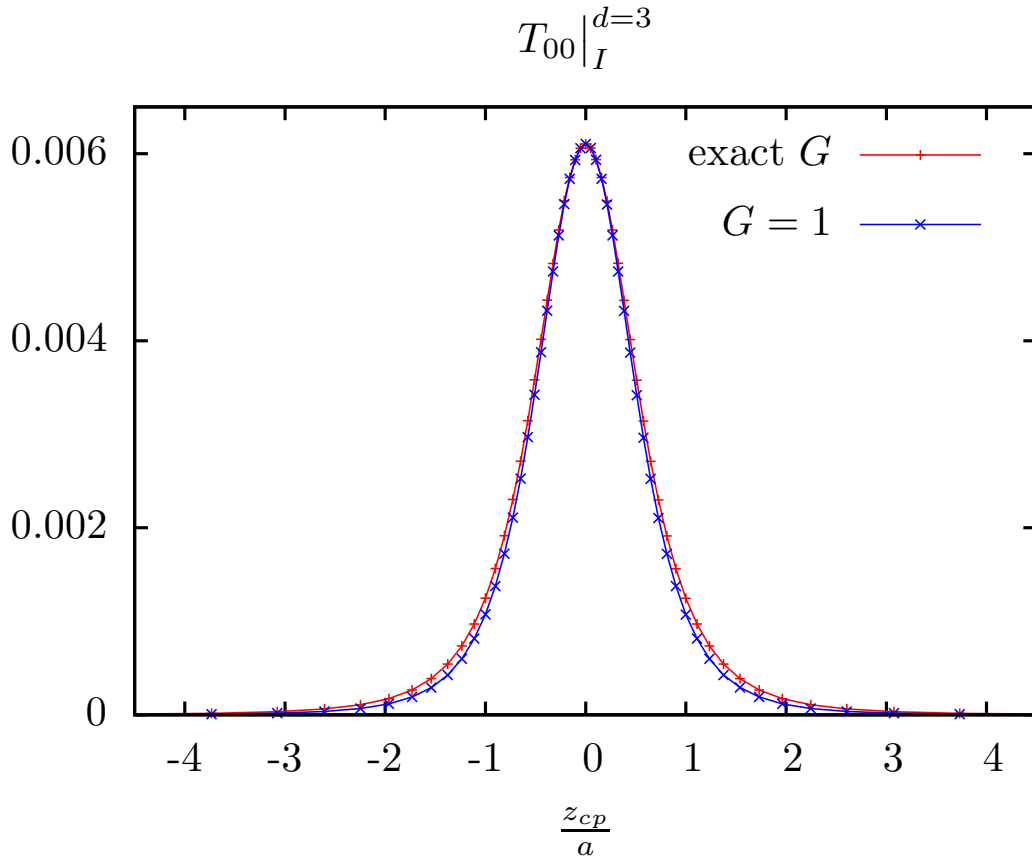


Figure 5.10 Comparison of $T_{00}(\vec{x}_{cp}, t)|_I$ for the plate with a hole in $d = 3$ using the intersection conditions \mathcal{M}_2 and \mathcal{M}_3 . Both data sets were computed from the same worldline ensemble of $N = 1.5 \cdot 10^6$ worldlines with 2^{16} points per loop.

find for the ANEC

$$\int_{-\infty}^{+\infty} dz_{cp} (T_{00}(\vec{x}, t) + T_{zz}(\vec{x}, t)) = \begin{cases} (1.76 \pm 0.17) \cdot 10^{-3}/a^3 & \text{worldline} \\ 1.63 \cdot 10^{-3}/a^3 & \text{analytical [22]} \end{cases} .$$

This means that we can reproduce the analytic ANEC for the plate with a hole in $d = 3$ with worldline numerics to within a 10% margin of error.

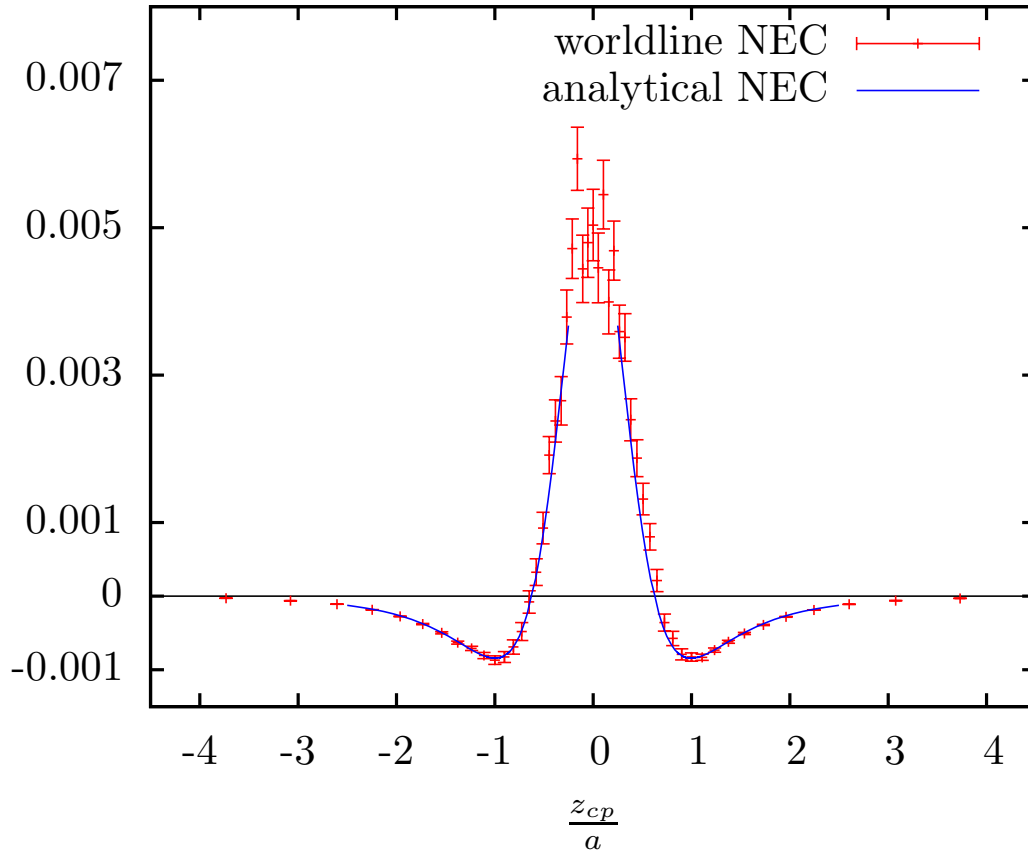


Figure 5.11 Null energy condition along the z axis for the punctured plate in $d = 3$ with the precise condition of intersection. We used an ensemble with $N = 1.5 \cdot 10^6$ and $n_{ppl} = 2^{16}$.

5.3 Averaged Null Energy Condition for a plate with a slit in $d = 3$

The case of an infinite Dirichlet plate in $d = 3$ with a slit is the third configuration for which we study the ANEC. To our knowledge there are no analytic results published for this boundary configuration. The plate with a slit is obtained from the punctured plate in 2 dimensions by a translation along a third dimension. Another way to think of it is to remove a strip from a plate in $d = 3$. A sketch of the general setup is shown in Fig. 5.12. The configuration is translationally invariant in x direction. We use the same parameters that we introduced for the the 2-dimensional plate with a hole. However, we need to specify the variable $y_{||}$. Despite having 3 spatial dimensions, we still only need

5 Averaged Null Energy Condition for configurations with complete geodesics

2-dimensional loops because the x direction is an invariant direction. We have therefore

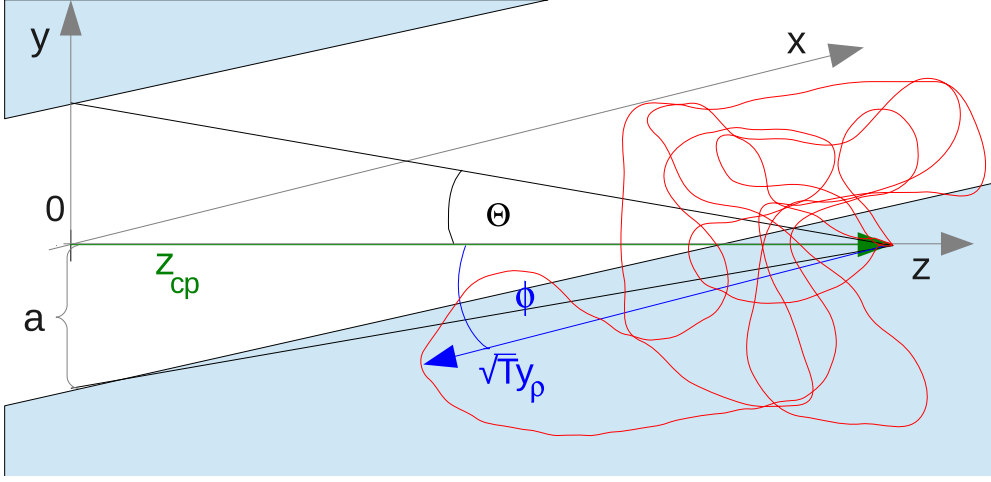


Figure 5.12 Sketch of the plate with a slit with an exemplary unit loop.

$y_{||} = y_y$ and the intersection conditions are truly 2-dimensional

$$\begin{aligned}\mathcal{M}_1 &= \max \left(-\frac{y_z(t)}{z_{cp}} \right) \Big|_{|\phi(t)| \geq |\Theta|} = -\frac{\hat{y}_z}{z_{cp}}, \\ \mathcal{M}_2 &= \max \left(\frac{y_\varrho(t)}{r} \cdot \frac{\cos \phi(t)}{\cos \Theta} \right) \Big|_{|\phi(t)| \geq |\Theta|} = \frac{\hat{y}_\varrho}{r} G, \\ \mathcal{M}_3 &= \max \left(\frac{y_\varrho(t)}{r} \cdot \frac{\cos \phi(t)}{\cos \Theta} \right) \Big|_{|\phi(t)| = |\Theta|} = \frac{\hat{y}_\varrho}{r}.\end{aligned}$$

(As before, \mathcal{M}_1 and \mathcal{M}_2 are exact and \mathcal{M}_3 is an approximation.) This makes the plate with a slit more closely related to the punctured plate in $d = 2$ from the point of view of worldline numerics. Nevertheless, the EMT depends on the physical dimension of space so that we should expect the values of the EMT and the NEC to show more similarities with the results of the plate with a hole in $d = 3$.

It is now straightforward to compute $T_{00}(\vec{x}_{cp}, t)|_I$, $T_{zz}(\vec{x}_{cp}, t)|_{I_a}$ and $T_{zz}(\vec{x}_{cp}, t)|_{I_b}$ and the NEC along the z axis using the intersection conditions \mathcal{M}_2 and \mathcal{M}_3 . The worldline ensemble is the very same that we used for the plate with a hole in 2 spatial dimensions.

5.3 Averaged Null Energy Condition for a plate with a slit in $d = 3$

For the δ_z derivatives we specify

$$h_\delta \ll \sqrt{\langle e^2 \rangle} \implies h_\delta = \nu \sqrt{\frac{1}{3}} = \nu \cdot 0.58 \quad \text{with } \nu = 0.12.$$

At first we compare the results of $T_{00}(\vec{x}_{cp}, t)|_I$ for the two different conditions of intersection \mathcal{M}_2 and \mathcal{M}_3 in Fig. 5.13. The worldline ensemble of $1.5 \cdot 10^6$ worldlines with 2^{16}

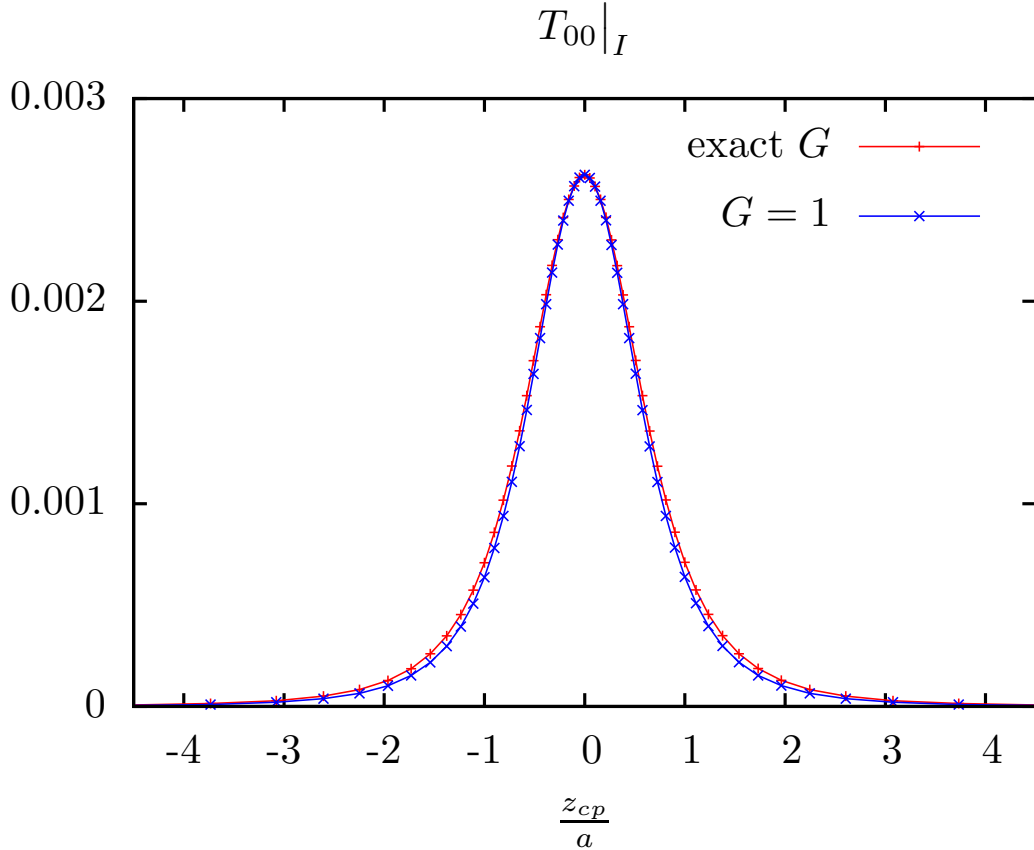


Figure 5.13 Comparison of $T_{00}(\vec{x}_{cp}, t)|_I$ for the plate with a slit using the intersection conditions \mathcal{M}_2 and \mathcal{M}_3 . Both data sets were computed from the same worldline ensemble of $N = 1.5 \cdot 10^6$ worldlines with 2^{16} points per loop.

points per loop is identical to the one used for the punctured plate in $d = 2$. The results using the exact value of G , that is, using \mathcal{M}_2 are 10 % larger at $z_{cp} = 1$ and 20 % larger at $z_{cp} \approx 2$ than the $G = 1$ result. This shows again that the approximation $G = 1$ becomes increasingly bad for increasing distance from the plate.

Fig. 5.14 shows the NEC along the z axis in this configuration using the precise intersection condition \mathcal{M}_2 . For the ANEC we integrate those results along with the NEC

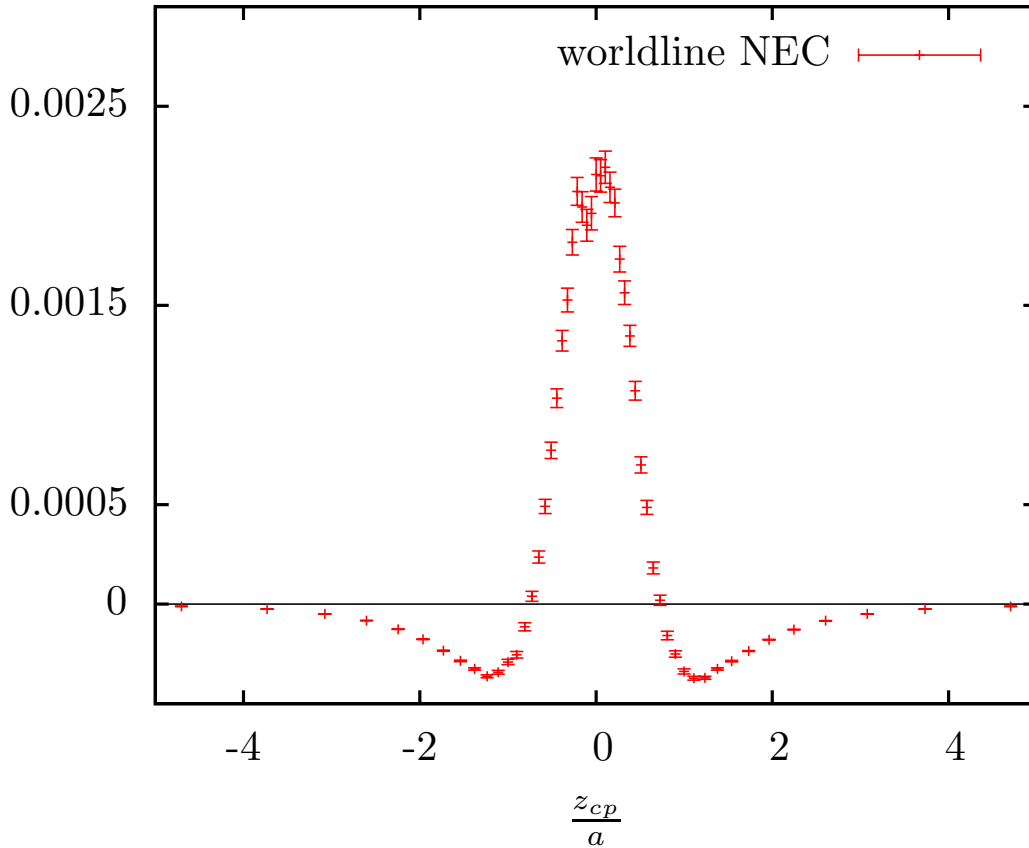


Figure 5.14 Null energy condition along the z axis for slit plate configuration with the precise condition of intersection. We used an ensemble with $N = 1.5 \cdot 10^6$ and $n_{ppl} = 2^{16}$.

Eq. (5.11) of the single plate in $d = 3$ for z_{cp} values outside the domain of our numerical data. The results of that integration are

$$\int_{-\infty}^{+\infty} dz_{cp} (T_{00}(\vec{x}, t) + T_{zz}(\vec{x}, t)) = \begin{cases} (0.813 \pm 0.119) \cdot 10^{-3}/a^3 & \text{for } G = 1 \\ (0.819 \pm 0.103) \cdot 10^{-3}/a^3 & \text{for exact } G \end{cases} . \quad (5.14)$$

Since there are no analytical values to compare with we have no benchmark point for reading off a systematic error of our results. However, it will presumably be of the same order of magnitude as the systematic errors of the two previous configurations, that is, at least of the order of 5%. The ANEC for the plate with a slit in $d = 3$ dimensions is also obeyed. Interestingly, its value is about half the value of the ANEC for the plate with a hole in 3 spatial dimensions.

5.4 Conclusions

We have computed the NEC and ANEC along the z axis for three different configurations in which the z axis is a complete geodesic, using worldline numerics. The first two setups, punctured plates in $d = 2$ and $d = 3$, served as tests for our numerical algorithm because there exist analytic results with which we can compare. During this comparison we found that the ANEC is reproduced with worldline numerics within a 10% error margin. The numerical calculation results in larger values than the analytic calculation. We were also able to extend the calculation of the NEC to region that are further away from the plates and to $z_{cp} = 0$. For the (semi-)analytical results in [22], values near $z_{cp} = 0$ had to be extrapolated. This extrapolation may lead to uncertainties in the result for the ANEC. However, our numerical algorithms, while they yield finite results near and at $z_{cp} = 0$, also show their largest systematic and statistical errors in that region. A reduction of errors, especially for z values inside and near the hole, will improve the numerical ANEC result.

For the third configuration, a plate with a slit in $d = 3$, there are no analytical results known. The numerical values of the ANEC are of the same order of magnitude as in the punctured plate case in $d = 3$, with the former about one half of the latter.

For the boundary configurations and the geodesic we chose, only two components of the energy-momentum tensor contribute to the ANEC, $T_{00}(\vec{x}, t)$ and $T_{zz}(\vec{x}, t)$. We were able to decompose these components in more compact terms, which lead to cancellation between terms of $T_{00}(\vec{x}, t)$ and $T_{zz}(\vec{x}, t)$ in the calculation of the NEC and thus in the ANEC as well. In fact, all that remains in the (A)NEC are two terms from the zz component, $T_{zz}(\vec{x}, t)|_{Ia}$ and $T_{zz}(\vec{x}, t)|_{Ib}$, that contain the derivatives with respect to z_{cp} and Δ_z . In the worldline picture these two terms the change of the intersection condition when moving the worldline along the z axis (change in z_{cp}) and changing the shape of the worldline (change in Δ_z), respectively. In other words it is not so much the intersection condition itself, which determines the value of the NEC at a certain point, but rather its rate of change when z_{cp} and Δ_z vary.

While $T_{00}(\vec{x}, t)$ and $T_{zz}(\vec{x}, t)$ correspond to the energy density and pressure, respectively, $T_{zz}(\vec{x}, t)|_{Ia}$ and $T_{zz}(\vec{x}, t)|_{Ib}$ do not have a physical interpretation. We also refrain from giving them such an interpretation since they are the result of a decomposition that is

5 Averaged Null Energy Condition for configurations with complete geodesics

based on our convenience and not on physical grounds. This decomposition may not be possible in other calculations of the EMT, with different representations and methods.

For all three boundary configurations, we find the NEC is violated for z values away from the boundary; the term $T_{00}(\vec{x}, t) + T_{zz}(\vec{x}, t)$ goes to zero from negative values for large distances from the boundaries. Near the plates the NEC shows a minimum and as the distance from the plate shrinks further (“moving into the hole”) it becomes positive. The finite maximum is reached at $z_{cp} = 0$, that is, inside the hole (or slit). We also find that the integral of the NEC along the z axis, that is, the ANEC, is positive because the positive contribution near the hole outweighs the negative contributions.

The qualitative similarity of our results for these three boundary configurations also allows for a thought experiment: we try to recover the results of the single plate configuration by letting the hole radius or slit width a go to zero. All distances in our calculations are scaled with a . For decreasing a , the minima move closer to the plate while their values become increasingly negative. On the other hand, the value of the maximum becomes more positive. Eventually, in the limit $a \rightarrow 0$, there will be an infinite, positive value of the NEC on the plate, while from the outside we have an infinite, negative value.

The numerical evaluation of these three boundary setups proved to be more involved than the single plate or two parallel plates cases. There are also several new sources for systematic errors whose reduction increased computation time to several CPU-days. A more detailed analysis and precise estimation of these errors is still missing because of that.

6 Summary and outlook

We succeeded at many steps in our worldline studies of the energy-momentum tensor for a quantum scalar field with boundary conditions. As a first goal, we extended the numerical worldline formalism to composite operators. The numerical evaluation of the worldline averages requires the use of *common point* loops that are only closed worldlines in the point-splitting limit $\vec{x} \rightarrow \vec{x}'$. Since the worldline expressions of the EMT components are finite by construction, they allow a decomposition into independent parts that, while having no explicit physical meaning, are often more compact in numerical calculations. We also have to compute derivatives of functionals of the worldlines $y(t)$. Although these worldlines are non-differentiable because they describe the Brownian motion of a diffusive process, we were able to compute derivatives of functionals of $y(t)$ with relatively small errors. The boundary configuration of the single Dirichlet plate and the two parallel plates are the prime examples of this calculation. Numerical results for both boundary configurations were computed with errors of generally less than 5%. Our algorithms still proved to be very efficient, taking only about 1 CPU-day for such computations.

The calculation of energy conditions for boundary configurations allowing complete geodesics was more involved. The conditions that determine the intersection of a worldline with a boundary are two-dimensional for these cases, and we used polar coordinates to parameterize them. The computations of derivatives proved to be more complicated than for the single plate and parallel plate configurations. The very large statistical fluctuations could only be reduced by an increase in the number of loops of our ensemble. This in turn increased computation time, making a detailed self-contained analysis of systematic errors unfeasible so far. Still, the current worldline data reproduce the analytically known results within the margin of error, which is about 10%. We also extended the calculation to values of z_{cp} for which there are no analytical data. This includes the regions far away from the plate, but especially the region inside the hole, at and near $z_{cp} = 0$. The results

6 Summary and outlook

of the plate with a slit are about one half of the punctured plate result in $d = 3$. We are not aware of any analytical data for this particular configuration.

An in-depth analysis of the errors for the punctured plate and the plate with a slit is the first goal of future numerical worldline calculations. This can be done in a brute force approach, by simply increasing the number of loops and the number of points per loop. However, it might also be possible to find another parameterization of the intersection condition that is numerically stable and allows for better control over the individual terms and their derivatives.

In a second step we would like to investigate other boundary geometries. The worldline formalism is perfectly suited to investigate different geometric setups because it is independent of the specific shape of the boundary surfaces. Especially curved surfaces or boundaries with edges and corners are therefore interesting. One can also try to find a geometry for which the ANEC has a minimal value. Intersection conditions similar to the one we used in Chapter 5 can be used as first estimate. It yielded good results for the NEC and ANEC, but the values for individual components carried large errors of over 20%. This simplified intersection condition is, in some respects, reminiscent of the proximity force approximation used in other Casimir effect calculations.

Another possibility is the inclusion of finite temperature effects, which is very easy to do in worldline numerics. The interplay between finite temperature and new geometries can lead to very interesting results for the Casimir effect [41].

Bibliography

- [1] H. Casimir, “On the attraction between two perfectly conducting plates,” *Kon. Ned. Akad. Wetensch. Proc.*, vol. 51, p. 793, 1948.
- [2] T. H. Boyer, “Quantum electromagnetic zero-point energy of a conducting spherical shell and the casimir model for a charged particle,” *Phys. Rev.*, vol. 174, pp. 1764–1776, Oct 1968.
- [3] D. Deutsch and P. Candelas, “Boundary effects in quantum field theory,” *Phys. Rev. D*, vol. 20, pp. 3063–3080, Dec 1979.
- [4] P. Candelas, “Vacuum energy in the presence of dielectric and conducting surfaces,” *Annals of Physics*, vol. 143, no. 2, pp. 241 – 295, 1982.
- [5] N. Graham, R. Jaffe, V. Khemani, M. Quandt, M. Scandurra, and H. Weigel, “Calculating vacuum energies in renormalizable quantum field theories:: A new approach to the casimir problem,” *Nuclear Physics B*, vol. 645, no. 12, pp. 49 – 84, 2002.
- [6] M. Bordag, U. Mohideen, and V. Mostepanenko, “New developments in the casimir effect,” *Physics Reports*, vol. 353, no. 13, pp. 1 – 205, 2001.
- [7] K. Milton, “The Casimir effect: Physical manifestations of zero-point energy,” *River Edge, USA: World Scientific*, 2001.
- [8] K. Milton, “Recent Developments in the Casimir Effect,” *J.Phys.Conf.Ser.*, vol. 161, p. 012001, 2009.
- [9] M. Bordag, G. Klimchitskaya, U. Mohideen, and V. Mostepanenko, “Advances in the Casimir effect,” *Int.Ser.Monogr.Phys.*, vol. 145, pp. 1–768, 2009.

Bibliography

- [10] M. Boström, S. Ellingsen, I. Brevik, M. Dou, C. Persson, and B. E. Sernelius, “Casimir attractive-repulsive transition in mems,” *The European Physical Journal B*, vol. 85, pp. 1–5, 2012.
- [11] G. Palasantzas and J. T. M. DeHosson, “Phase maps of microelectromechanical switches in the presence of electrostatic and casimir forces,” *Phys. Rev. B*, vol. 72, p. 121409, Sep 2005.
- [12] E. Buks and M. L. Roukes, “Stiction, adhesion energy, and the casimir effect in micromechanical systems,” *Phys. Rev. B*, vol. 63, p. 033402, Jan 2001.
- [13] S. A. Fulling, K. A. Milton, P. Parashar, A. Romeo, K. Shajesh, *et al.*, “How Does Casimir Energy Fall?,” *Phys.Rev.*, vol. D76, p. 025004, 2007.
- [14] K. A. Milton, P. Parashar, K. Shajesh, and J. Wagner, “How does Casimir energy fall? II. Gravitational acceleration of quantum vacuum energy,” *J.Phys.A*, vol. A40, pp. 10935–10943, 2007.
- [15] K. Shajesh, K. A. Milton, P. Parashar, and J. A. Wagner, “How does Casimir energy fall? III. Inertial forces on vacuum energy,” *J.Phys.A*, vol. A41, p. 164058, 2008.
- [16] M. S. Morris and K. S. Thorne, “Wormholes in spacetime and their use for interstellar travel: A tool for teaching general relativity,” *Am. J. of Phys.*, vol. 56, no. 5, p. pp. 395, 1988.
- [17] M. S. Morris, K. S. Thorne, and U. Yurtsever, “Wormholes, time machines, and the weak energy condition,” *Phys. Rev. Lett.*, vol. 61, pp. 1446–1449, Sep 1988.
- [18] M. Visser, “Traversable wormholes: Some simple examples,” *Phys. Rev. D*, vol. 39, pp. 3182–3184, May 1989.
- [19] S. Kar, N. Dadhich, and M. Visser, “Quantifying energy condition violations in traversable wormholes,” *Pramana*, vol. 63, no. 4, pp. 859–864, 2004.
- [20] C. J. Fewster and T. A. Roman, “On wormholes with arbitrarily small quantities of exotic matter,” *Phys. Rev. D*, vol. 72, p. 044023, Aug 2005.

- [21] K. D. Olum, “Superluminal travel requires negative energies,” *Phys. Rev. Lett.*, vol. 81, pp. 3567–3570, Oct 1998.
- [22] N. Graham and K. D. Olum, “Plate with a hole obeys the averaged null energy condition,” *Phys.Rev.*, vol. D72, p. 025013, 2005.
- [23] N. Graham and K. D. Olum, “Achronal averaged null energy condition,” *Phys.Rev.*, vol. D76, p. 064001, 2007.
- [24] M. Visser, “Gravitational vacuum polarization. 1: Energy conditions in the Hartle-Hawking vacuum,” *Phys.Rev.*, vol. D54, pp. 5103–5115, 1996.
- [25] M. Visser, “Gravitational vacuum polarization. 2: Energy conditions in the Boulware vacuum,” *Phys.Rev.*, vol. D54, pp. 5116–5122, 1996.
- [26] M. Visser, “Gravitational vacuum polarization. 3: Energy conditions in the (1+1) Schwarzschild space-time,” *Phys.Rev.*, vol. D54, pp. 5123–5128, 1996.
- [27] M. Visser, “Gravitational vacuum polarization. 4: Energy conditions in the Unruh vacuum,” *Phys.Rev.*, vol. D56, pp. 936–952, 1997.
- [28] C. J. Fewster, K. D. Olum, and M. J. Pfenning, “Averaged null energy condition in spacetimes with boundaries,” *Phys.Rev.*, vol. D75, p. 025007, 2007.
- [29] L. S. Brown and G. J. Maclay, “Vacuum stress between conducting plates: An Image solution,” *Phys.Rev.*, vol. 184, pp. 1272–1279, 1969.
- [30] K. A. Milton, “Calculating casimir energies in renormalizable quantum field theory,” *Phys.Rev.*, vol. D68, p. 065020, 2003.
- [31] K. A. Milton, “Finite casimir energies in renormalizable quantum field theory,” pp. 1021–1040, 2004.
- [32] A. Scardicchio and R. Jaffe, “Casimir effects: An Optical approach. II. Local observables and thermal corrections,” *Nucl.Phys.*, vol. B743, pp. 249–275, 2006.
- [33] R. Feynman, “Mathematical formulation of the quantum theory of electromagnetic interaction,” *Phys.Rev.*, vol. 80, pp. 440–457, 1950.

Bibliography

- [34] C. Schubert, “Perturbative quantum field theory in the string inspired formalism,” *Phys.Rept.*, vol. 355, pp. 73–234, 2001.
- [35] H. Gies, J. Sanchez-Guillen, and R. Vazquez, “Quantum effective actions from non-perturbative worldline dynamics,” *JHEP*, vol. 0508, p. 067, 2005.
- [36] H. Gies and K. Klingmuller, “Quantum energies with worldline numerics,” *J.Phys.A*, vol. A39, pp. 6415–6422, 2006.
- [37] L. Moyaerts, K. Langfeld, and H. Gies, “Worldline approach to the Casimir effect,” pp. 203–211, 2003.
- [38] H. Gies, K. Langfeld, and L. Moyaerts, “Casimir effect on the worldline,” *JHEP*, vol. 0306, p. 018, 2003.
- [39] H. Gies and K. Klingmuller, “Casimir edge effects,” *Phys.Rev.Lett.*, vol. 97, p. 220405, 2006.
- [40] H. Gies and K. Klingmuller, “Worldline algorithms for Casimir configurations,” *Phys.Rev.*, vol. D74, p. 045002, 2006.
- [41] A. Weber and H. Gies, “Interplay between geometry and temperature for inclined Casimir plates,” *Phys.Rev.*, vol. D80, p. 065033, 2009.
- [42] M. Schäfer, I. Huet, and H. Gies, “Energy-Momentum Tensors with Worldline Numerics,” *International Journal of Modern Physics: Conference Series*, vol. 14, pp. 511–520, 2012.
- [43] M. Schaden, “Dependence of the Direction of the Casimir Force on the Shape of the Boundary,” *Phys.Rev.Lett.*, vol. 102, p. 060402, 2009.
- [44] K. Aehlig, H. Dietert, T. Fischbacher, and J. Gerhard, “Casimir Forces via Worldline Numerics: Method Improvements and Potential Engineering Applications,” 2011.
- [45] A. Sommerfeld, *Vorlesungen über Theoretische Physik - Band VI - Partielle Differentialgleichungen*. Akademische Verlagsgesellschaft Geest & Portig K.-G., Leipzig, 4 ed., 1958.

- [46] J. D. Jackson, *Klassische Elektrodynamik*. Walter de Gruyter, 2 ed., 1982.
- [47] A. D. Polyanin and V. F. Zaitsev, *Handbuch der linearen Differentialgleichungen*. Spektrum Akademischer Verlag, 1996.
- [48] C. G. C. Jr., S. Coleman, and R. Jackiw, “A new improved energy-momentum tensor,” *Annals of Physics*, vol. 59, no. 1, pp. 42 – 73, 1970.
- [49] N. Graham, R. Jaffe, V. Khemani, M. Quandt, M. Scandurra, *et al.*, “Casimir energies in light of quantum field theory,” *Phys.Lett.*, vol. B572, pp. 196–201, 2003.
- [50] N. Graham, R. Jaffe, V. Khemani, M. Quandt, O. Schroeder, *et al.*, “The Dirichlet Casimir problem,” *Nucl.Phys.*, vol. B677, pp. 379–404, 2004.
- [51] N. Graham and K. D. Olum, “Negative energy densities in quantum field theory with a background potential,” *Phys.Rev.*, vol. D67, p. 085014, 2003.
- [52] K. D. Olum and N. Graham, “Static negative energies near a domain wall,” *Phys.Lett.*, vol. B554, pp. 175–179, 2003.
- [53] D. Schwartz-Perlov and K. D. Olum, “Null energy conditions outside a background potential,” *Phys.Rev.*, vol. D68, p. 065016, 2003.

Appendix A

Systematic errors for two parallel plates

In Fig. A.1 and A.2 we show the systematic errors for the various components of the energy-momentum tensor for the parallel plates configuration. We evaluate these components at three different values z_{cp} , using ensembles with 25 000 worldlines and from 2^{10} up to 2^{20} points per loop. The figures also show the corresponding analytical values and one sees how our worldline results approach them. The systematic errors decrease like $1/n_{ppl}$ with increasing number of points per loop. We therefore fit our numerical data to a function $a + b/n_{ppl}$. In the limit $n_{ppl} \rightarrow \infty$, the difference between the analytical result and the parameter a is an estimate for the remaining systematic error. We display those error estimates in Tab. 4.1.

Appendix A Systematic errors for two parallel plates

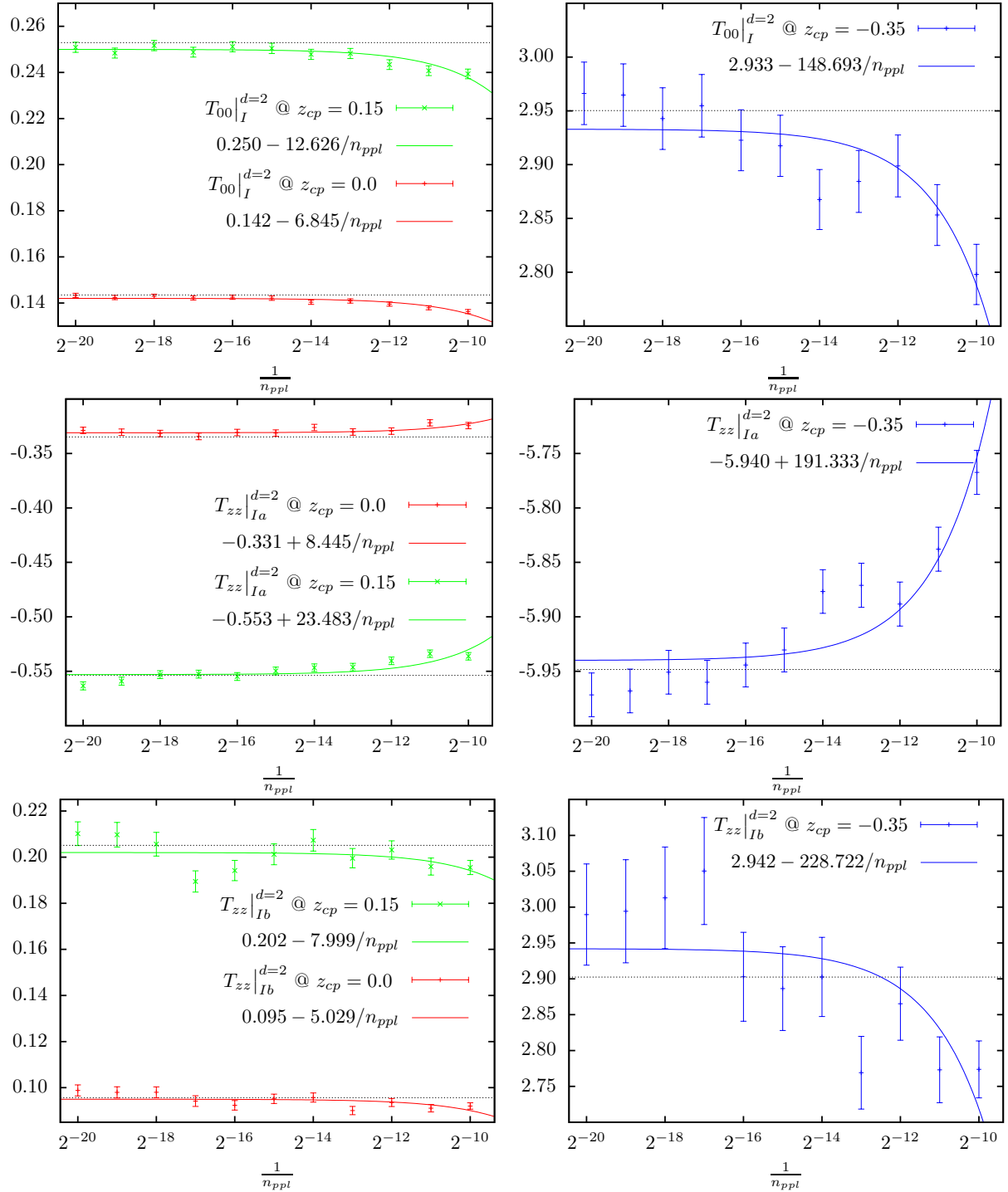


Figure A.1 Systematic errors of EMT components in $d = 2$ dimensions for $z_{cp} \in \{0.15, 0.0, -0.35\}$. The solid lines are fits of our data and the dotted lines are analytical values.

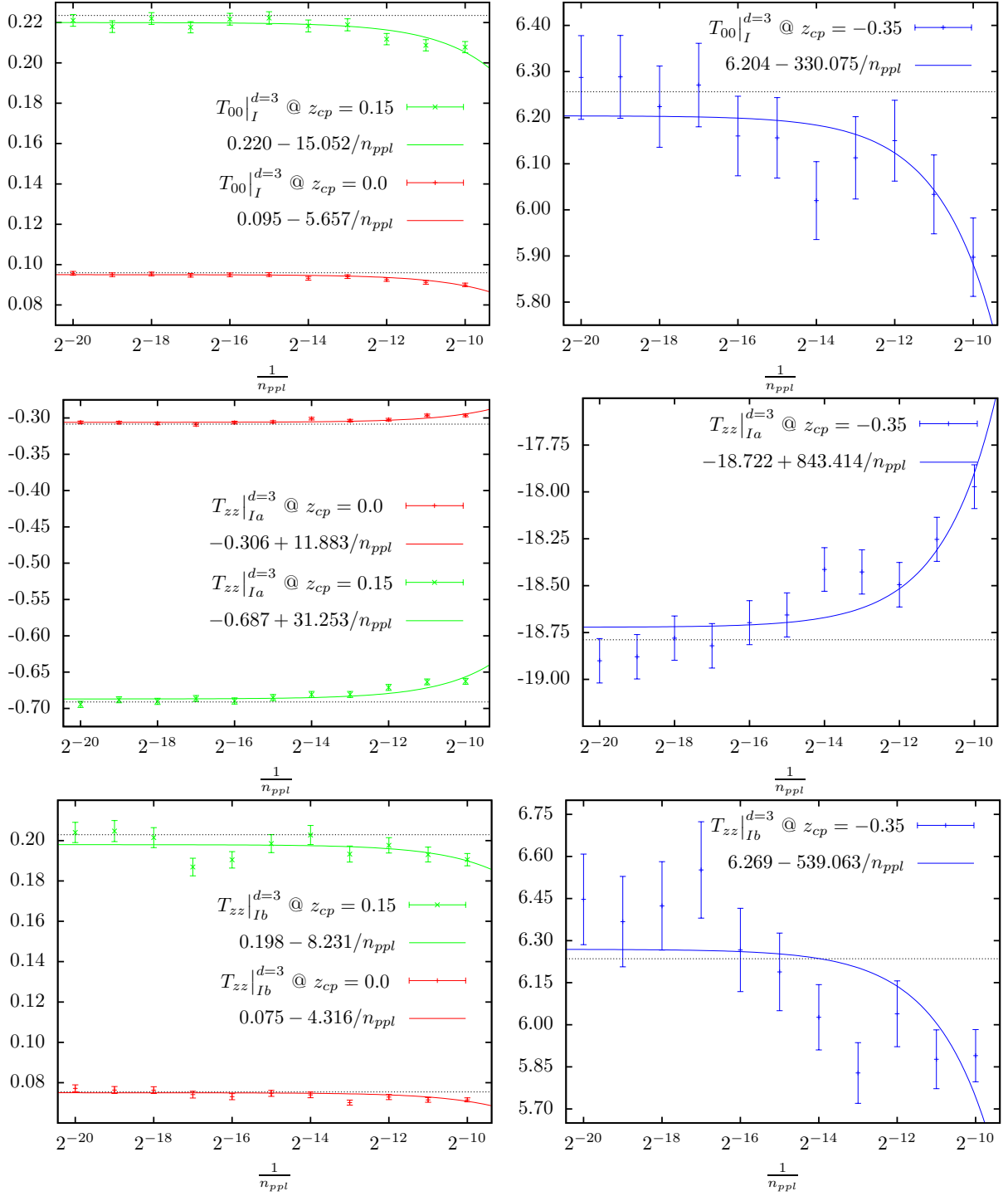


Figure A.2 Systematic errors of EMT components in $d = 3$ dimensions for $z_{cp} \in \{0.15, 0.0, -0.35\}$. The solid lines are fits of our data and the dotted lines are analytical values.

Acknowledgements

I would like to express my gratitude to all those who helped and supported me, and therefore contributed to the successful completion of this thesis.

I thank my supervisor Holger Gies for the good collaboration, the opportunity for independent research and his extensive understanding for all the difficulties and challenges that were to be met in the past three and a half years. I am indebted to Idrish Huet Hernandez for the great collaboration. Without him, many calculations in this thesis would not have been completed. My referees Noah Graham and Christian Schubert have my gratitude for the interesting discussions during their visits here in Jena. Furthermore, I would like to thank Noah Graham for providing the analytical results that were used in this thesis.

For a great working atmosphere and many interesting conversations and discussions, I thank all fellow members of the Theoretical-Physical Institute and the Research Training Group “Quantum and Gravitational Fields”, especially all my past and current office mates: Jens Braun, Franziska Synatschke-Czerwonka, Lukas Janssen, Björn Welleghausen, Daniel Körner, Marianne Heilmann and Daniel August.

Moreover I am indebted to Christine Großer and the “Linkshand-Initiative Jena” without whom I would not have been able to complete this thesis. And finally I thank my family, especially my sisters Dana and Yvonne, for their unwavering support and encouragement over the years.

Ehrenwörtliche Erklärung

Ich erkläre hiermit ehrenwörtlich, dass ich die vorliegende Arbeit selbstständig, ohne unzulässige Hilfe Dritter und ohne Benutzung anderer als der angegebenen Hilfsmittel und Literatur angefertigt habe. Die aus anderen Quellen direkt oder indirekt übernommenen Daten und Konzepte sind unter Angabe der Quelle gekennzeichnet.

Weitere Personen waren an der inhaltlich-materiellen Erstellung der vorliegenden Arbeit nicht beteiligt. Insbesondere habe ich hierfür nicht die entgeltliche Hilfe von Vermittlungs- bzw. Beratungsdiensten (Promotionsberater oder andere Personen) in Anspruch genommen. Niemand hat von mir unmittelbar oder mittelbar geldwerte Leistungen für Arbeiten erhalten, die im Zusammenhang mit dem Inhalt der vorgelegten Dissertation stehen.

Die Arbeit wurde bisher weder im In- noch im Ausland in gleicher oder ähnlicher Form einer anderen Prüfungsbehörde vorgelegt.

Die geltende Promotionsordnung der Physikalisch-Astronomischen Fakultät ist mir bekannt.

Ich versichere ehrenwörtlich, dass ich nach bestem Wissen die reine Wahrheit gesagt und nichts verschwiegen habe.

Jena, den 6. Dezember 2012